A Package-Integratable Six-Port Reflectometer for RF Power Devices

Razvan-George Venter

A Package-Integratable Six-Port Reflectometer for RF Power Devices

Razvan-George Venter

A thesis submitted to the Department of Microelectronics, Faculty of Electrical Engineering, Mathematics and Computer Science, Delft University of Technology, in partial fulfilment of the requirements for the degree of

Master of Science

in

Microelectronics

TU Delft mentors:

Dr. ing. Leo C.N. de Vreede

ir. Rui Hou

Dr. ir. Koen Buisman

NXP mentor:

Dr. ir. Klaus Werner

Thesis committee:

Dr. ing. Leo C.N. de Vreede

Dr. ir. Marco Spirito

Ir. Rui Hou

Dr. ir. Koen Buisman

Prof. dr. Andrea Neto

Dr. ir. Klaus Werner

April 2014

A Package-Integratable Six-Port Reflectometer for RF Power Devices

Razvan-George Venter

Abstract

Semiconductor power devices have a growing popularity in industrial, scientific and medical (ISM) band applications, such as microwave-heating, drying and plasma generation. A distinguishable property of these applications is the relentless pursuit of reliability, ruggedness, or the ability to withstand a mismatched loading condition without failure. Mismatch detection right at device output, preferably integrated in package, could provide critical information to avoid device breakdown and to enable performance optimization.

In this work, the in-package mismatch detection and load monitoring is enabled by a specially designed six-port reflectometer. Compared with conventional reflection measurement techniques based on heterodyne receivers, the proposed design is passive, simple, compact and inexpensive. A hardware prototype is implemented with a size of 36 mm^2. Loading conditions over the entire Smith chart are generated by a calibrated active-load-pull system and measured by the proposed system, yielding a root-mean-square error below -32 dB full-scale. This compact reflectometer enables the in-package accurate mismatch detection for the first time.

The result of this study has been accepted for publication in the 2014 International Microwave Symposium, and nominated to be a finalist for its annual best paper award.

Table of contents

List of figures

List of tables

Acknowledgement

This report represents the sum of all the work that I put into the project during the last year. It was an amazing journey, with ups and downs, like any other good thing that you remember for the whole rest of your life. Looking back now at the beginning, I find myself more mature, more critical with problems, and more experienced than in the first days dedicated to this thesis. I can honestly say that in the end, working on this project brought me more satisfaction than I could ever think of at the start. However, the road was not an easy one, and this section is dedicated to all the people that helped me a lot during the progress.

On the top of the list I would like to thank Dr. Leo de Vreede, my thesis supervisor. He was the one that proposed the idea of this project in the beginning, and helped me many times when I was stuck in the first months. The work-related discussions that you have with Leo are not easy, but this is what in the end shapes you from a complete beginner into a more experienced professional ready to face real life challenges. Besides the technical part, Leo always looked to me like a model to follow in life. He is very passionate about his work, but always relaxed, with a smile on his face, and willing to end a discussion in an optimistic mood.

I will also like to gratefully thank Rui Hou. His work-related advice helped me so many times to solve the problems and continue the process such that these problems do not appear again. He has a unique way of making you understand the concepts, even difficult ones, by giving simple real life examples, and I always admired that. Also, his power of motivating anything he says is amazing and I haven't found it so far in a lot of persons.

Another very important person for me was Dr. Koen Buisman. Koen helped me a lot understand the project goal and the possible problems in the very beginning. Also, during the whole progress the advices coming from his experience helped a lot in building a better understanding and confidence. Koen helped me also with the measurement set-ups, explaining them to me and cleverly fixing certain bugs.

Special consideration is also given to Klaus Werner from NXP Semiconductors Nijmegen, who sponsored this work in the last part, and who provided the technology access very promptly and whenever it was needed.

Last, but not the least, I would like to thank the important people in my life that gave me the balance needed during the work process. First of all my family, for providing honest support and advices whenever things were not looking so good during my stay in the Netherlands. Secondly, some incredible persons that I found here, Cristina, Lucian, Vlad, Victor, Matei, Ruxandra, and all the others, for spending amazing moments together and always being there. This thesis is dedicated to you.

Razvan-George Venter

Delft, The Netherlands

1.Introduction

1.1   Motivation

We are living in a moment when the most important devices that we use on a daily basis have already reached a certain maturity. If several decades ago we were just witnessing the first stages of certain domains such as mobile communications, computing techniques or basic electronic equipment, today all of those have become part of our normal lives, things that we take for granted, and whose existence we consider as normal as any everyday activity. This is why most of the manufacturers in any domain have migrated towards improving their already existing concepts rather than eagerly developing new ones. What today is introduced as a major new thing is actually just a better design, with new and improved features, of the basic concept that exists for already a large number of years. New mobile phones use the same basic idea like the mobile telephony was having at the beginning of the 90's: they allow people to communicate "on the go". The fact that still nowadays we are seeing one new major mobile phone release almost every month has to do with them being thinner, lighter, with a larger and more colourful screen, with more features than their old versions. And that's what keeps the audience awake, and the interest high (on average a person changes his mobile phone once every two years nowadays, compared to once every seven years in the 90's [1]). The same thing is valid for TVs, for example. The idea is the same, the size of the screen, their power consumption, their new features, all of these represent the difference. Microwave ovens were initially used only in restaurants when they were first released. Now you can find one in almost every house, and still the producers do not stop developing them, coming with improved designs in terms of cooking time, power consumption or cooking efficiency.

Obviously the list started above can continue and extend to almost any domain one can think of. The idea is that the main technology driver in the present day is the wish to make everything better, cheaper, and generally more reliable. It is not a moment when someone can have exclusivity for producing something everywhere in the world. It is probably not a mistake to affirm that for anything that is being produced or performed, there are a certain number of companies or individuals that are disputing the first position, and considering the fact that they all start from the same idea, the difference is made on the details, or in a more general view, the quality of the work or of the product.

Easily moving to the technical and hardware side of the problem, which is the domain in which this work is placed, the quality of a certain product is defined by its performances, reliability, lifetime, and of course other factors such as aspect, easiness of use, etc. It is useless to buy for example a mobile phone that looks very good but has the power consumption so

large that the battery has to be recharged once every several hours. Also, any other electronic equipment designed for domestic or professional use could not bring satisfaction if it breaks down immediately, even in the case of a small human error. After all, what brings more confidence to a user than the idea that a product will never fail or break in any condition, no matter what you do to it?

It was maybe visible from the first paragraphs of this thesis that the area that will represent the interest zone of the work is focused on electric and electronic equipment or products. In particular, the motivation from where this work was originated was to be able to make devices more "intelligent" in the sense of making them able to actively detect potentially dangerous operating situations. Most of the reasons why electronic devices fail nowadays are that they cannot handle unexpected situations such as sudden short circuits, high voltages, reflected power entering back the device, etc. If somehow they would be able to monitor in real time the conditions in which they operate, they would be able to adjust their working conditions, or in the worst case, completely shut down until safer operating conditions are detected again. For example, more and more electronic devices nowadays (such as laptops or mobile phones) have detection circuitry able to "feel" sudden short circuits that happened inside, as a result of, for example, dropping liquid on the device. Also, most of electronic equipment already integrated temperature detection, to avoid overheating that could lead to bad functionality or destruction.

This thesis will describe the design and implementation of a low level solution for a series of high level problems. The regular user having no background in electrical engineering or microwaves in particular will see the impact of the proposed design in daily major problems such as energy consumption, reliability and also quality of the product. Used into a range of regular applications, such as microwave ovens for example, this solution will be able to provide a better power consumption/cooking quality ratio, while also assuring a longer life time for the oven.

The research taken in this work will focus on a particular type of device used in a certain number of basic applications: the power amplifier. These devices are used on a wide range of products, from heating devices, and microwave ovens to base stations. To be more specific, almost anytime we are talking about devices operating at radio frequencies (RF), power amplifiers are also involved. This is why very special care is put in optimizing their design. As it was started in the beginning of this chapter, also in the case of the power amplifiers the basic concepts have already been stated, and good understanding about the subject has been made during the last decades. Extended literature exists describing all the particular notions that one needs in order to design and use a power amplifier. Because these concepts are already known and widely applied, nowadays most of the attention is set towards making the power amplifier more reliable, robust, power efficient or compact, without

degrading its set of performance characteristics. If we add to these also the ability to self-detect the conditions in which it operates, the result will be a failure safe power transistor capable of adjusting its operating regime in order to adapt to the external conditions and still deliver its best performance characteristics. That would be eventually the detail that makes all the difference between a normal and a great power transistor.

1.2   The problem and its importance

As it will be presented in Chapter 2 of this work, power transistors can be designed for operating in particular regimes, named classes of operation. All the different classes are good for particular applications and each of them is designed in a different way from the others in terms of performance. However, the basic thing that unites them is the fact that all classes of operation require certain loading conditions in order to be able to work at the highest efficiency and deliver the maximum amount of power into the output load. Delivering a high power at a good efficiency is clearly a thing that is preferable in the operation of these amplifiers. This is why it would be very beneficial if the loading condition at their output port stays as close as possible to the ideal desired condition, also called a matched condition. However, besides the situation in which the amplifier works with a reduced efficiency due to a mismatched load, there is also another problem which can be even more dangerous. This is represented by a varying loading condition. If this happens, then the efficiency at which the power transistor operates is continuously changing. Also, the same is valid for the power delivered into the load. In some applications this changing value of the delivered power might not be very disturbing. However, there are applications in which the constant level of the delivered power is actually the most important aspect of the whole device.

Let us take the example of the microwave oven. A simplified drawing of such a device is presented in Fig. 1.1.
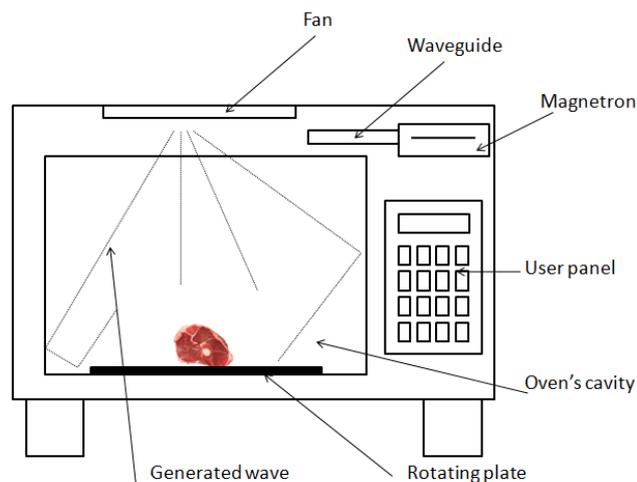
Fig. 1.1 - Simplified block diagram of a microwave oven presenting the most important internal blocks.

As it can be seen, the waves which are generated inside the oven's cavity come from a magnetron, which, on its side, is driven by a power amplifier. A fan placed on the top of the cavity scatters the microwave radiation and distributes it uniformly into the cavity. As the microwaves hit the walls of the oven, they are reflected back, losing a certain amount of power. A rotating plate placed on the bottom of the cavity rotates the food such that it is hit as uniformly as possible by the waves found inside.

The user therefore assumes that the power which he set on the oven's front panel is also the power that actually reaches the food placed in the cavity. This is important because particular types of food require a particular power level generated by the oven in order to be cooked properly and uniformly. However, different types of food placed inside the microwave oven will appear as a different load to the power amplifier driving the magnetron. That is also not all of it. It is known that water has an electrical permittivity ε_r which is temperature dependent. A change in the electrical permittivity also translates to a change in the impedance. Even if the temperature dependence of other types of food is neglected, most of them still contain water, which leads to changing impedances with respect to the temperature inside the cavity.

The food depending reflection coefficient is why in most cases the power that will be delivered by the power amplifier into the cavity will not be equal to the power set by the user on the oven's panel. Moreover, because most microwave ovens are equipped with a rotating plate inside, the reflection coefficient will be also constantly changing during the whole cooking process. This will lead to constantly changing output power, which in the end leads to possible burned, raw, or non-uniformly cooked food. If we also assume that the user is not concerned about aspects such as power consumption, size, electrical characteristics, etc., he will however most likely be concerned about the quality of the cooking process. This is why it is very important to "feel" the dynamically changing conditions inside the oven's cavity.

Of course, one must keep in mind the general trend taken by most manufacturers nowadays: making products more compact and reducing as much as possible the production cost. Regarding the above stated problem, it would make no sense to come with a solution which requires either a lot of extra space, or which would considerably increase the production cost. Therefore a low cost, ultra compact solution will be the main target during this work, as it will be further stated in the next chapters.

Continuing with the example of the microwave oven, which is actually the main industry end target of this research, being able to detect the loading conditions can be used as just the first step in a process of making the oven smarter and more robust. Afterwards, additional processing devices such as microcontrollers can be added in order to monitor the loading condition and adjust the power amplifier's operating parameters in order to still deliver

the best possible performance. This could lead in the end to a safer, more reliable, and of course healthier solution.

1.3 Area of research

As it was presented in the above section, the problem that will be investigated in this work is the impedance mismatch present at the output of a power amplifier. There are various ways of measuring the impedance mismatch in general, as this concept is used in a wide area of applications. Therefore, also the ways of measurement are varying from application to application, such as plasma detection, neuromodulation detection, or even thermal detection. The approach that will be taken in this thesis involves an **electrical** way of measuring the reflection coefficient and therefore the impedance mismatch. During the next chapters, all the concepts that will be introduced and analysed and all the conclusions that will be taken will be based entirely on an electrical perspective. Other individual ways of performing the same final goal do not represent the scope of this work and will not be investigated.

1.4 Structure of this thesis

The contents of this thesis will be divided into the most important sub categories of the main research domain. These categories are actually also the independent steps that were taken in order to design, produce, and test the proposed solution. After this brief introduction to the investigated problem, Chapter 2 will be dedicated to the basic background notions that are required and which will be used throughout the entire text. The basic functionality of a power amplifier, as well as particular ways of measuring the reflection coefficient known in literature will be also presented here. Chapter 3 will introduce the user to the first novel design proposed in this project: a package integrated bondwire based directional coupler, occupying as little area as possible and still being able to achieve competitive performance specifications. After investigating possible ways of implementing the integrated directional coupler, a new approach towards the use of the well known six port reflectometer will be presented in Chapter 4. This device will make use of the above mentioned bondwire directional coupler, plus a detection loop on which four detection ports are placed. Once again compactness is the main targeted aspect, which is why the whole six port reflectometer design will be integrated inside the power transistor's package. Chapter 5 will be dedicated to the various calibration algorithms used to handle the information provided by the integrated six port reflectometer. Several algorithms have been tested, some of them well known in literature, plus a personal algorithm based on the use of the reflectometer's S parameters. Chapter 6 is dedicated to the design of the power detectors that will also be integrated inside the package together with the six port design. Everything from the different test topologies to diode linearization algorithms and performance results will be covered here. The most important results obtained after the performed

measurements will be presented in Chapter 7. This chapter will prove the functionality of the designed reflection coefficient detection structure, showing also the obtained errors and possible explanations for their existence. Finally, the most important conclusions regarding this work will be drawn in Chapter 8. Also, some of the future work that is planned at the current moment will be illustrated here.

References

[1] R. Entner, "International comparisons: the handset replacement cycle", Recon Analytics, June 2011.

2. Reflection coefficient measurement

2.1   Definitions

The measurement of impedance mismatch is one of the most basic procedures in radio frequency applications. Under wrong output loading conditions, power amplifiers can work poorly or even get damaged. This is why careful consideration is given to the process of detecting the output impedance seen by the power amplifier, and make sure that this one does not get close to a potentially dangerous value.

For explaining the reflection coefficient at the output port of an amplifier, a start is made from the schematic presented in Fig. 2.1.
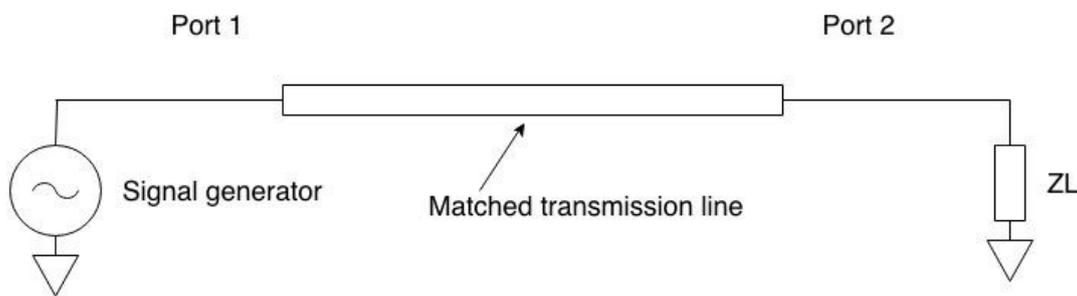
Fig. 2.1 - A power source injecting RF power into a matched transmission line terminated with an arbitrary load impedance.

Here power is injected at port 1 of the transmission line. One could imagine that this power source is actually the power amplifier generating power into a load. In the presented figure, the load is drawn at the end of the microstrip transmission line. The transmission line can be considered perfectly matched to the signal source in this example, such that no power is lost due to insertion loss. The power injected at port 1 travels along the transmission line until it reaches the load present at port 2 (Z_L). There a fraction of the injected power gets reflected, depending on the value of the load impedance. The following relation can be defined:

$$\Gamma_L = \frac{(Z_L - Z_0)}{(Z_L + Z_0)} \quad (2.1)$$

In Eq. 2.1 Z_L is the load impedance at port 2, and Z_0 is the characteristic impedance of the system. The newly introduced quantity, Γ_L, defines the amount of voltage wave reflection that is produced by a load of a certain value Z_L, when an incident voltage wave produced by a source with Z_0 internal impedance reaches it. In practice, Γ_L is called the *reflection coefficient*. By analysing the expression, one can observe that for a Z_L value equal to Z_0, the value of the reflection coefficient is 0. This is called a matched condition, or that all the power is absorbed by the load, so the load is matched to the transmission line and does not reflect anything back. Also, particular cases can be obtained for the situation when $Z_L=0$ (short), or $Z_L=\infty$ (open),

7

situations in which the reflection coefficient has a value of 1 in magnitude, or basically all the power injected into the load gets reflected back to the power source.

An important concept very related to the reflection coefficient at a specific port is represented by the *"a" and "b" waves*. This concept refers to the forward and reflected waves along a transmission line. The forward wave is known as the "a" wave and is the wave that is incident at ports 1 and 2 of Fig. 2.1. The wave that gets reflected from port 1 or 2 in Fig. 2.1 is called the reflected wave, and is also known in literature as the "b" wave. Depending on the amount of mismatch, the "b" wave can have a smaller or larger value. Fig. 2.2 presents schematically the definition of the "a" and "b" power waves at the 2 ports of a transmission line.
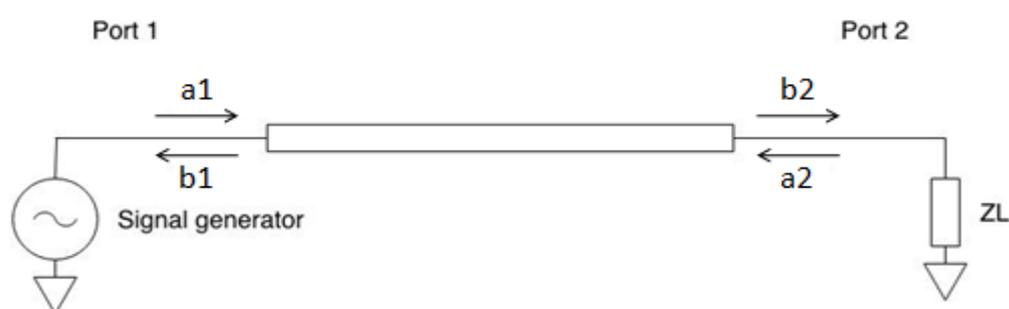
Fig. 2.2 - Forward and reflected "a" and "b" waves at the ports of a transmission line.

In literature, usually the waves entering a port are referred to as the "a" waves. In a similar way, the waves that come out of the port are labelled the "b" waves. This notation has also been followed in the above figure.

The reflection coefficient defined at the beginning of this chapter can be easily related to the newly introduced "a" and "b" waves, as it is equal to the ratio of the reflected wave and the forward (or incident) wave as presented in Eq. 2.2:

$$\Gamma_L = \frac{a_2}{b_2} \qquad (2.2)$$

Individually, the "a" and "b" waves are defined in Eq. 2.3 and 2.4:

$$a = \frac{V + Z_R * I}{2 * \sqrt{Z_R}} \qquad (2.3)$$

$$b = \frac{V - Z_R * I}{2 * \sqrt{Z_R}} \qquad (2.4)$$

In the above expressions V and I represent the total voltage and current on a transmission line in terms of incident and reflected voltage waves amplitudes, as presented in Eq. 2.5 and 2.6:

$$V = V_0^+ + V_0^- \qquad (2.5)$$

$$I = \frac{V_0^+ + V_0^-}{Z_0}, \qquad (2.6)$$

Z_0 being the characteristic impedance of the line.

Therefore, the individual unit of measurement for the "a" and "b" waves is:

$$\frac{V}{2 * \sqrt{\Omega}}$$

If one takes the absolute value and squares the previously presented expression, $V^2/2*\Omega$ is obtained, which is proportional to W, the measurement unit or power. This is why these quantities are related to the power flowing in the forward of reverse way on a transmission line.

A concept related to the "a" and "b" waves is represented by the *S parameters* of a particular microwave network. As it will be presented later on in this chapter, a series of ways in which the reflection coefficient at the output of a power device can be calculated involve the use of the S parameters. These parameters are a simple and powerful way of representing a network in terms of the forward and reflected waves present at each port, which were previously introduced. The S parameter matrix of a circuit is defined as an N x N matrix, where N is the total number of ports present in the network. Each component of the matrix, generally denoted S_{ij} represents the amount of transfer existent between ports *i* and *j*. More formally, a general S parameter can be defined in terms of the "a" and "b" waves as presented in Eq. 2.7:

$$S_{ij} = \frac{b_i}{a_j} \qquad (2.7)$$

In this expression, a_j is the incident wave present at port *j*, and b_i is the reflected wave at port *i*, as presented in Fig. 2.2. The S parameters are the best way to know the behaviour of a certain network. Most of the ways of measuring the reflection coefficient make use of them, or use other algorithms to actually determine the S parameters of the network.

Besides giving information about the reflection coefficient and the transfer between each pair of ports, the "a" and "b" waves have an important value in understanding better the reflection from an output load. Depending on the value of the reflection coefficient, or how much power gets reflected back after the contact with the load impedance, a *standing wave* will be created along the transmission line. The standing wave is formed as a result of the interference between the forward wave and the reverse wave. The normalized voltage standing wave for different values of the reflection coefficient is presented in Fig. 2.3.
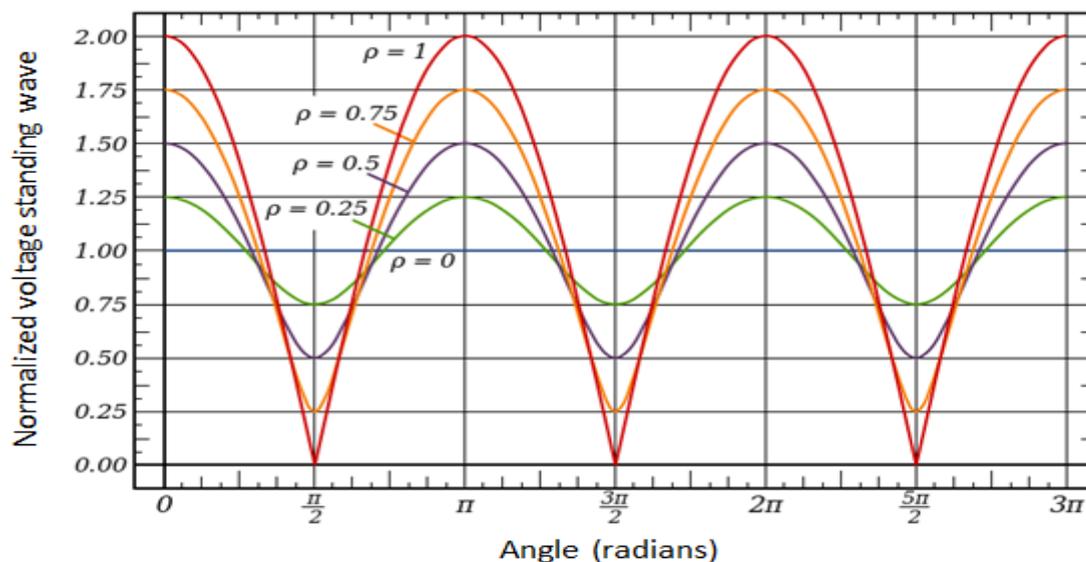
Fig. 2.3 - Normalized voltage standing wave ratio along a transmission line terminated with several types of mismatched loads. $\rho = |\Gamma_L|$.

It can be seen that the larger the reflection, the higher the amplitude of the standing wave existent along the transmission line. It can also be seen that the standing wave presents a certain periodicity, being periodic every π radians. This property will prove to have a great importance in the design that is going to be proposed in Chapter 4 of this work. By dividing the maximum and minimum voltage values from the voltage standing wave, the *standing wave ratio* (SWR) is obtained. The standing wave ratio is related to the forward and reflected waves travelling along a transmission line. As these waves can also define the reflection coefficient of an arbitrary load impedance, it means that the standing wave ratio and the reflection coefficient are also connected to each other, the relation between them being presented in Eq. 2.8.

$$SWR = \frac{1+|\Gamma_L|}{1-|\Gamma_L|} \quad (2.8)$$

It was stated earlier that the main target of this work are the power amplifiers. The design that will be presented in the future chapters represents just an extension to the concept of these amplifiers, and does not constitute a part of their individual design. However, this work will have an impact on certain aspects in the theory of power amplifiers such as the RF power delivered to a specific output load, and the efficiency of operation. Therefore it is useful to define these concepts before using them in further statements.

The *output power* delivered by a power transistor is the power that reaches the load connected at the transistor's drain terminal. As it was specified in the beginning of this chapter, depending on the amount of reflection at the output port, this delivered power can be larger or smaller. Referring to Fig. 2.2, the output power delivered by the amplifier into a load can be expressed in terms of the "a" and "b" waves as presented in Eq. 2.9:

$$P_{out} = |b_2|^2 - |a_2|^2 \quad (2.9)$$

10

Another concept related to the output delivered power is the *drain efficiency* of the device. This relates the output power with the DC power consumed by the transistor, as in Eq. 2.10:

$$\eta = \frac{P_{out}}{P_{DC}} \qquad (2.10)$$

In the above relation P_{DC} is the DC power consumed by the device.

It can be observed that this relation does not include any information about the *input power* of the power transistor. Therefore, another relation very often used in practice defines the *power added efficiency* as presented in Eq. 2.11:

$$\eta_{PAE} = \frac{P_{out} - P_{in}}{P_{DC}} \qquad (2.11)$$

A quick explanation of how these characteristics are influenced by the above defined reflection coefficient will be given in the next section of this chapter.

So far the most important definitions related to Γ_L have been presented. The "a" and "b" waves can be used to calculate the transfer between each pair of network's ports and also the reflection coefficient present at any of these ports. On the other hand, the reflection coefficient is linked with a direct relation to the impedance found at a particular port, as well as with the power amplifier performance characteristics such as the delivered power into the load (P_{out}) or the drain efficiency in case of constant supply power.

It was stated in Chapter 1 that measuring the reflection coefficient has a great importance in the functionality of a microwave system and this statement was highlighted also by the definitions given in the beginning of this chapter. A deeper explanation of its importance is presented in the next section.

2.2   The importance of measuring the reflection coefficient

The loading conditions present at the output port of a power amplifier are vital for its operation. Depending on the class of operation for which the amplifier is designed, it requires a certain loading condition in order to be able to deliver the maximum amount of power, or achieve its highest efficiency. The theory of designing and making the output matching networks of a power transistor is not the objective of this work. However, the conclusion regarding the importance of using the power transistor with the correct output loading condition is illustrated with a simple example.

Consider the schematic presented in Fig. 2.4.
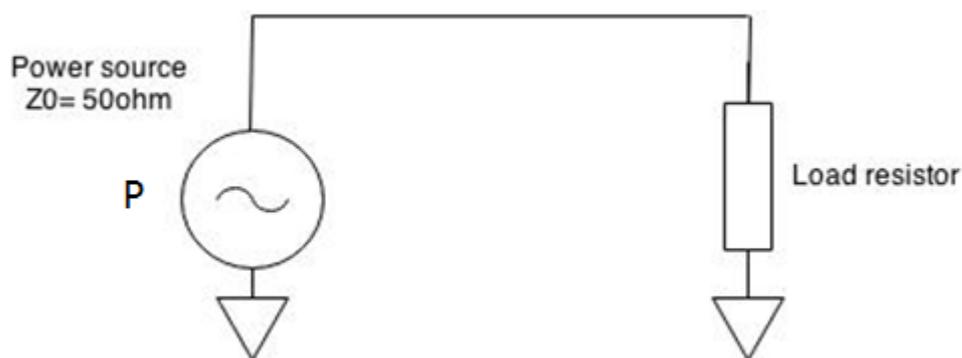
Fig. 2.4 - General schematic of a power source injecting power into an arbitrary load impedance.

In this circuit P is an ideal power source which can be set to generate any power level. For an example, P is set to a power of 40 dBm, which is equal to 10 W. Depending on the value of the load resistor (in this case purely ohmic), a plot of the power that will actually be delivered into the load is presented in Fig. 2.5.
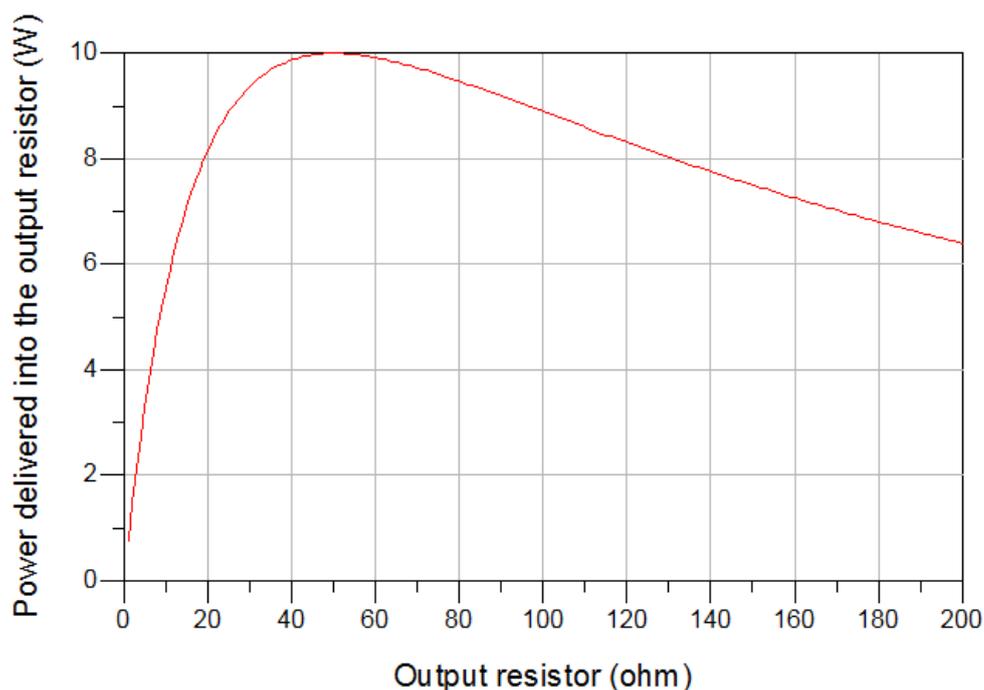
Fig. 2.5 - Output power delivered into the load by the power source represented in Fig. 2.4, depending on the value of the real load impedance.

It can be seen that for an output resistor value of 50 Ω (equal to the power source's internal impedance) all the power generated by the power source is transferred to the load resistor. When the resistor is mismatched, the power that is delivered to the load starts to drop, even if the power level generated by the source is kept constant. This happens because due to the mismatch, a fraction of the source power will be reflected at the load resistor's port. Considering the definition of the drain efficiency for a power transistor introduced in Eq. 2.10,

it can be seen that when the power delivered into the load starts to drop, also the efficiency is reduced, assuming that the DC power consumption remains constant.

As it can be seen, if the output load deviates from this perfect loading condition, the performance of the amplifier degrades, and if the load starts to deviate strongly, there is even the risk of damaging the amplifier. In practice every power amplifier has a limit on the mismatch condition that it can handle at its maximum drive conditions. At low power drive levels there is a low risk of this kind of damage. However, if one is using a power amplifier with a very reflective load presented at the output, the large power level that gets reflected back into the amplifier can cause problems. If this power level is comparable or even higher than the specification, there is a high risk of damaging the device. The physical explanation of this risk is related to the voltage or current standing waves found in particular cases of output loading conditions. For example, if the output loading condition for a power amplifier is an open ($Z_L = \infty$), the voltage wave present on the transmission line connecting the amplifier with the load will be two times larger than the incident voltage wave V^+. If the resulting voltage wave gets close to, or even higher than the power transistor's breakdown voltage, there is a clear risk of damaging the device. Similarly, if the output load is a short ($Z_L=0$), the current wave formed on the transmission line between the power amplifier and the load will have two times the amplitude of the forward current wave. If this value gets large, it can lead to an overheating of the internal transistor structure, raising again the possibility of device damage.

Usually all systems make sure that the loading conditions present at the output of the power amplifiers never exceed the specified dangerous values. This is the case of the systems that are able to monitor and control the value of the reflection coefficient, or the systems in which the reflection coefficient does not have a (fast) variation over time. However, there are also applications that are not as comfortable with respect to the reflection coefficient. In certain applications, such as microwave ovens, the load impedance is not set by the user, but is actually defined by the particular type of food or object that is placed inside the microwave oven's cavity. Considering the vast range of products that can be placed nowadays inside a microwave oven, it is clear that the value of the load impedance seen by the power amplifiers generating the microwave radiation will vary a lot from case to case. Also, all modern microwave ovens are equipped with an internal rotating plate, to assure uniformity in the cooking. However, continuously changing the physical position of the food placed inside also adds to the varying impedance seen by the amplifier. External directional couplers are normally used in practice in power amplifier circuits in order to determine the value of the reflection coefficient and possibly correct the operating regime of the amplifier. However, the use of such directional couplers in the case of microwave ovens is not suitable, as it would need extra space, as well as increasing the total production cost. Therefore, when omitting these couplers, the power amplifiers present inside microwave ovens will have very little information about the

conditions in which they are operating. Even assuming that the reflection will never get that high such that the power amplifiers will get damaged, still having a large mismatch will lead to very low efficiency and low (and not constant) power delivered into the load. Finally, for the end user this means non-uniformly cooked food, even with the help of the rotating plate. For all these reasons, being able to monitor the reflection coefficient in general is a very important practice that should be done as reliable as possible, with as little as possible added cost and complexity. In literature, most of the ways of calculating Γ_L involve coupling a small fraction of the forward and reflected waves. A better explanation about this concept is offered in the next section.

2.3   Power coupling fundamentals

Several ways to measure the reflection coefficient at the output of the device involve using a directional coupler, as it will be presented in the next section of this chapter. A directional coupler operating principle is illustrated in Fig. 2.6.
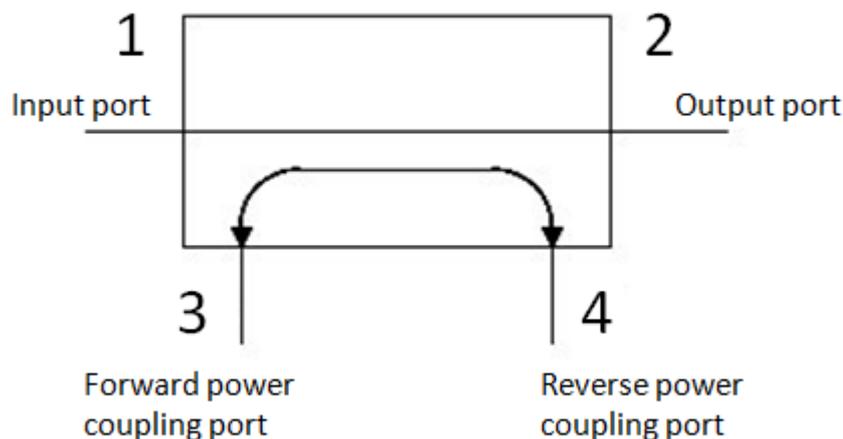
Fig. 2.6 - Diagram presenting the functionality of a basic (reverse wave) directional coupler.

The illustrated coupler is a reverse directional coupler, as the forward coupled port (port 3) is placed next to the input port (port 1). This type of directional coupler is the one that will be explained in Chapter 3 of this work. However, the same principle is valid also for the forward directional couplers. The idea is that a small fraction of the forward (incident) power is coupled at port 3 of the coupler in Fig. 2.6. Also, in a similar fashion, a small fraction of the reflected power will be coupled at port 4. From these coupled powers, the "a" and "b" waves along the main line can be calculated. The reflection coefficient at port 2 of the structure in Fig. 2.6 can be determined by taking the ratio of the "a" and "b" waves as explained in Section 2.1.

The directional coupler is mostly defined by two main characteristics: the *coupling factor* and the *directivity*. The *coupling factor* is the amount of forward and reflected power that gets coupled and later used to determine the reflection coefficient. In certain applications, including this work, it is desirable that most of the power generated by the power amplifier reaches in the end the load. This is why in these applications the coupling factor usually has a low value. Commercial directional couplers have a coupling factor in the order or -30 dB or even less, which means that 0.1% of the incident or reflected power gets coupled into the directional coupler. Therefore it adds very low losses to the power amplifier. The second very important aspect is the *directivity*, or the ability to distinguish between the forward and the reflected waves. As seen in Fig. 2.6, port 3 of the directional coupler should couple only a fraction of the forward power along the main line. However, in practice, it will also couple part of the reflected power. The ratio in dB between the forward and reflected coupled powers represents the directivity of the directional coupler. Commercial devices can have directivities larger than 30 dB. Above this level, it can be considered that almost all the power coupled at port 3 of the directional coupler represents forward (incident) power and the errors introduced in further calculations by also coupling a part of the reflected power are negligible.

Based on these two performance factors, various implementations of directional couplers are possible. Extensive literature exists on the subject of adjusting the circuit dimensions in order to obtain the best values for coupling and directivity [1]. However, the application that will be further described in the next chapters of this work imposes special conditions. Its most important limitation is the size, since the final goal is to aim for full package integration of all the designed additional circuits.

This work will make use of a less conventional way of coupling power. Since inside the package there are already bondwires connecting the power bar drain to the drain package lead, it is attractive to make use of these in order to create the power coupling structure. By inserting a coupling element (such as a microstrip line) next to the bondwire array, the power flowing through them will also couple in the secondary element. This principle is presented in the form of an Ansys HFSS layout in Fig. 2.7.
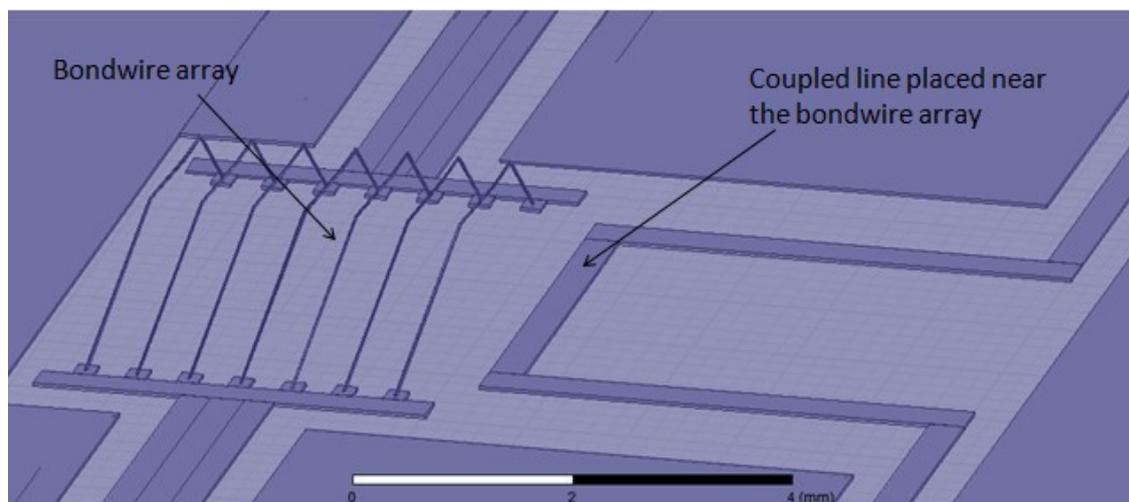
Fig. 2.7 - Concept of creating a compact directional coupler by placing a microstrip line in the proximity of a bondwire array (Ansys HFSS layout).

In this way, one can use the benefits of a directional coupler inside the package. Of course, strict restrictions will have to be followed mostly based on the total area available inside the package for the additional circuitry, but also the more or less fixed length of the bondwires in the bondwire array, which will have an impact on the achieved coupling factor and directivity. More information about the directivity and coupling factors obtained using these kinds of bondwire based directional couplers will be presented in the next chapter, where several possible ways of placing the coupled element will be investigated. Also, an analysis on the influence of bondwire length and the distance between the bondwires and the coupled circuit will be performed. However, before beginning with the description of the proposed design, it is useful to present an overview of the known ways of measuring the reflection coefficient, together with some recognized implementations already published in literature. The next two sections of this chapter will be dedicated to this review.

2.4 Ways of determining the reflection coefficient

During the previous years, a lot of ways of measuring the output loading condition and the output reflection coefficient have been analysed and published. An overview of the most important results will be presented in Section 2.5 of this chapter. In a general point of view, the methods of measuring the reflection coming from an unknown load divide in two main categories: by using both magnitude and phase of the coupled signal, and by using only the magnitude of the coupled signal. The choice between these two depends on the preference of the user and is much related to the constraints that one is facing in implementing the method.

2.4.1 Down converting mixer based measurement solutions (Vector Network Analyzer)

If one is able to measure both magnitude and phase of the coupled incident and reflected waves, then the general algorithm for the calculation of the reflection coefficient is simplified. By knowing the coupling factors (either by the coupler's indication or by measuring the device), a system of equations can be made, and the solutions to all the required travelling waves (forward and reflected) can be found in a complex form. This means that the reflection coefficient can be determined also in a complex form, with 100% accuracy if the algorithm and the terms corrections are applied right. The block diagram of the downconverting method is presented in Fig. 2.8.
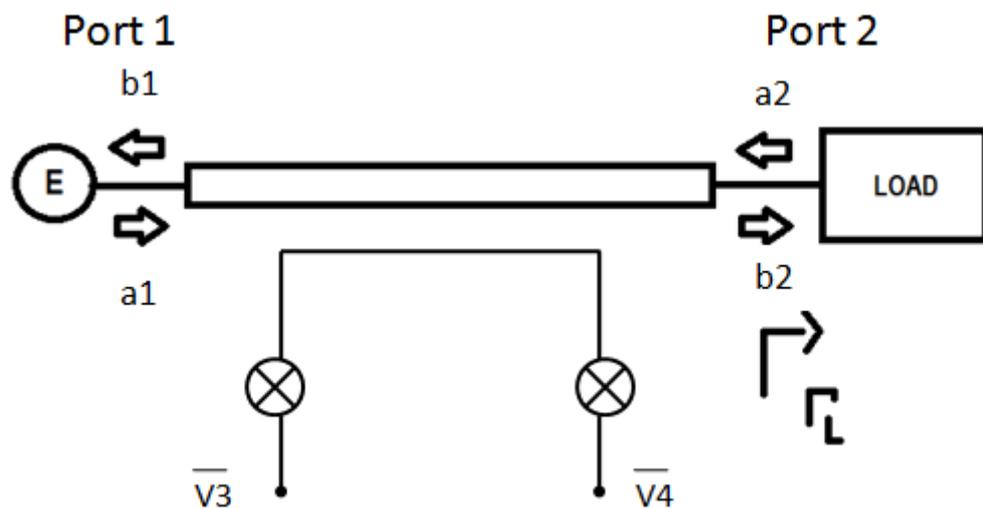
Fig. 2.8 - Schematic representing the block diagram of a voltage downconverting method.

In this figure, the "a" and "b" waves previously defined in this chapter are put into evidence at the two ports of the main line, which in the proposed implementation will represent the bondwire array inside the power transistor's package. The only condition for calculating the complex value of the reflection coefficient is to read and use the complex value of the voltage at each of the detector ports. In principle this refers to a vector network analyser approach, which is currently the most common technique for the measurement of s-parameters / reflection coefficients. A more detailed explanation of this technique is presented in [2].

2.4.2 Direct detection measurement solutions

In practice it is often difficult / costly to measure both the magnitude and the phase of the coupled signal. This is because it involves the use of an additional down converting mixer, which requires more area and mightintroduce interference due to the additional LO signal. What is commonly done is that only the magnitude of the coupled wave is measured. If the magnitudes of the forward and reflected waves are measured, then in theory the magnitude of the reflection coefficient can be found, and the complex value of the reflection coefficient is

known to lie on a circular locus on the Γ_L plane, having as the radius the magnitude that has been calculated previously. This is schematically presented in Fig. 2.9.

Locus of possible values of Γ_L determined by
two magnitude detectors (red)

Γ_L plane with unit circle(blue)
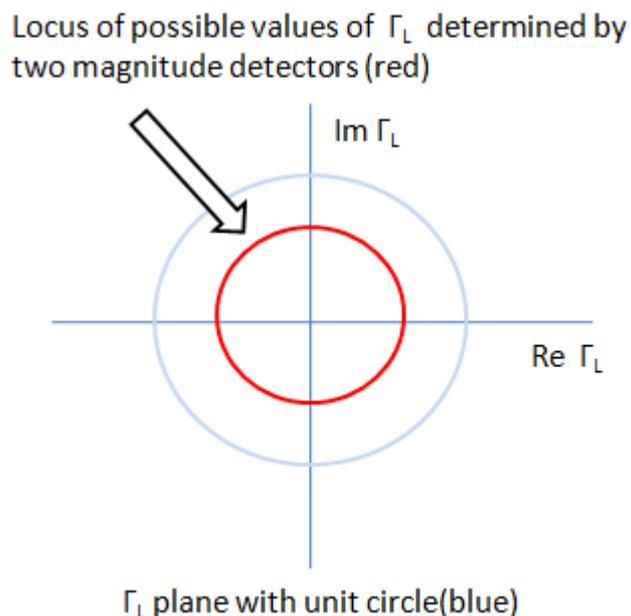
Fig. 2.9 - Locus of Γ_L values determined by using two magnitude detectors to detect the magnitude of the "a" and "b" waves.

The problem is that this method assumes perfect directivity in coupling the forward and reflected waves. With other words, it assumes from the start that all the power coupled on the forward port of the directional coupler represents forward power on the main line, and the same for the reflected power. In practical implementations this can never happen. A very good directivity is in the order of 30 dB, as achieved by commercially available devices. This means that an error will be introduced in the calculation of the Γ_L magnitude value. For a better explanation of this error, it is useful to consider a practical example. If a perfectly matched load is placed at the output port, there should be no reflection coming back from the load, as all the generated forward power should be absorbed. In this way, there should also be no reverse wave detected at the reverse coupled port of the directional coupler. However, because of the non-ideal directivity, this port will couple a little fraction of the forward wave that travels towards the load. By reading the magnitude of the coupled waves at the two detector ports, the calculation algorithm will "assume" that a certain amount of reflection exists at the load plane, since there is power coupled on the reverse coupled port. From this wrong assumption, an error in the calculation of the reflection coefficient is generated. It is clear that a higher directivity will therefore minimize this introduced error. Above some level (usually 30 dB), the amount of forward coupled power into the reverse coupled port for a perfectly matched load will be very small (even though not exactly 0). The conclusion is that depending on the directivity that one

has in the directional coupler, this Γ_L calculation error can be considered negligible or can have a significant value.

An alternative for measuring both magnitude and phase of the coupled signal is to measure only the magnitude, and still be able to determine the complex value of the reflection coefficient. The method is the base for the multi-port reflectometer methods. These particular types of circuits couple the forward and reflected waves not only in two points, like a directional coupler, but in several. For the case of a six port reflectometer, the way of functioning will be further described in Chapter 4. Also, the calculation algorithms for determining the complex value of the reflection coefficient are not so straight forward like in the case of the directional coupler. However, if one has enough computation hardware available, this would not represent a real problem, the advantage of using only magnitudes being still significantly bigger. There are a vast number of published papers describing different topologies that can be used in order to measure the reflection coefficient of a device under test. Some of the most representative will be succinctly presented in the next section.

2.5   Previous work

The measurement of the reflection coefficient of a device under test represents nowadays one of the most basic procedures in the microwave domain. This is because of two reasons: being able to calculate the reflection coefficient at the output of a device is very often vital for its correct functionality, and also vast literature exists on the presented domain, such that the problem is today fully understood. While a full journey into the evolution of the measurement techniques would require an individual text book publication, this section proposes to present and describe the most important approaches that were published during the years. All of them represent alternative ways of reaching the same final goal, but the ways in which the measurement is performed are adapted to a particular kind of application, as it will be seen.

Theoretically speaking, any network can be described by its set of S parameters, which were introduced in Section 2.1. If the S parameters can be measured, the first step towards the calculation of the complex reflection coefficient at any port has already been done. A good theoretical reference for determining Γ_L based on the S parameters for the device under test in multiport networks is given in [3] and [4].

In practice, the basic theoretical ways in which the reflection coefficient can be determined have been illustrated in Section 2.4 of this chapter. These ways have been implemented in a large range of applications, depending on the final design target. Some of the most representative of them will be described as follows.

An easy way to measure the reflection coefficient is by using a directional coupler in order to sample the forward and reflected waves that travel on a line, followed by a

downconverting mixer to read the high frequency information. The functionality of the directional coupler was presented in Fig. 2.6. The forward coupled port couples a small fraction of the forward power existing on the main line. In a similar fashion, the reverse coupled port couples a fraction of the reflected power (depending on the amount of mismatch on the output port). By knowing the coupling factor and the directivity between the two coupled ports, it is possible to calculate the reverse and forward waves, and therefore the reflection coefficient. As it was explained in the above section, depending on the existence of phase information, the complex value, or only the magnitude of Γ_L are calculated. These concepts are presented more clearly in [5] and [6].

As more knowledge was collected on the subject, deeper analysis into the reflection coefficient measurement techniques were performed and more complex circuits introduced. Considering the calculation of the magnitude of Γ_L as a known measurement, most of the work found in literature was towards the calculation of the complex Γ_L, with as little additional hardware as possible, and without the need to measure the S parameters of the structure.

An early approach towards the measurement of complex reflection coefficient was done by B. Galwas [7]. His measurement system included a slotted line together with a homodyne detector, as presented in Fig. 2.10.
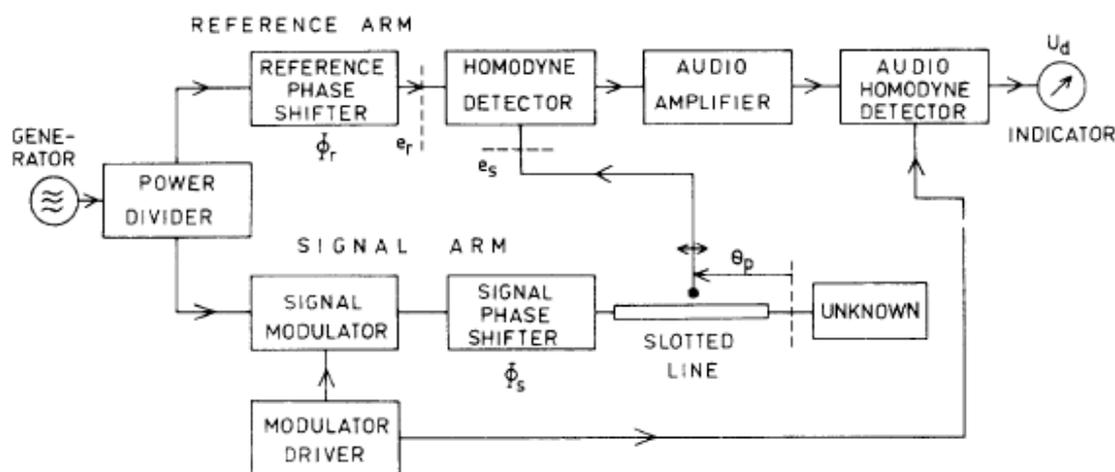
Fig. 2.10 - Block diagram representation of the Γ_L measurement method published in [7]. This method uses a slotted line to detect a phase relation correlated to the complex reflection coefficient of the unknown load.

For a test load impedance present at the output port, multiple positions on the slotted line are considered (with different phases θ_P), such that in the end a variation of $(\theta_R - \theta_P)$ in relation to the complex value of Γ_L is obtained. As it can be seen, the implementation is very complex and requires a large number of additional devices such as two phase shifters, two homodyne detectors, an amplifier and a signal modulator.

Another early implementation this time making use of a directional coupler was reported in [8] and is presented schematically in Fig. 2.11.
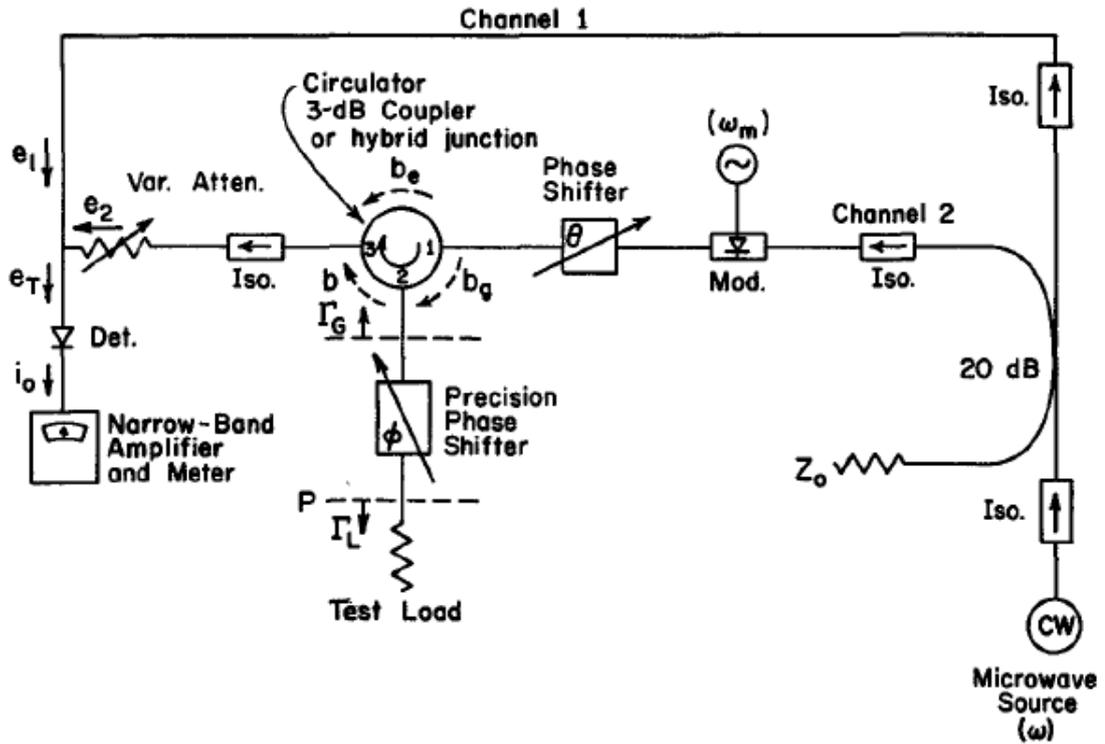
Fig. 2.11 - Block diagram representation of the Γ_L measurement method published in [8]. This approach uses a directional coupler followed by a system of phase shifters, isolators and a circulator to calculate the complex value of Γ_L.

It can be seen that a directional coupler with a medium directivity is used, but complicated additional devices are needed to determine both the phase and magnitude of the reflection coefficient. Again the use of phase shifters, together with isolators, amplifiers and a circulator makes this implementation a fairly large one.

A more compact approach towards this problem is presented in Fig. 2.12 and more in detail described in [9]. This time, two directional couplers are used, but however the additional circuitry is reduced only to an extra hybrid T, plus two diode detectors.
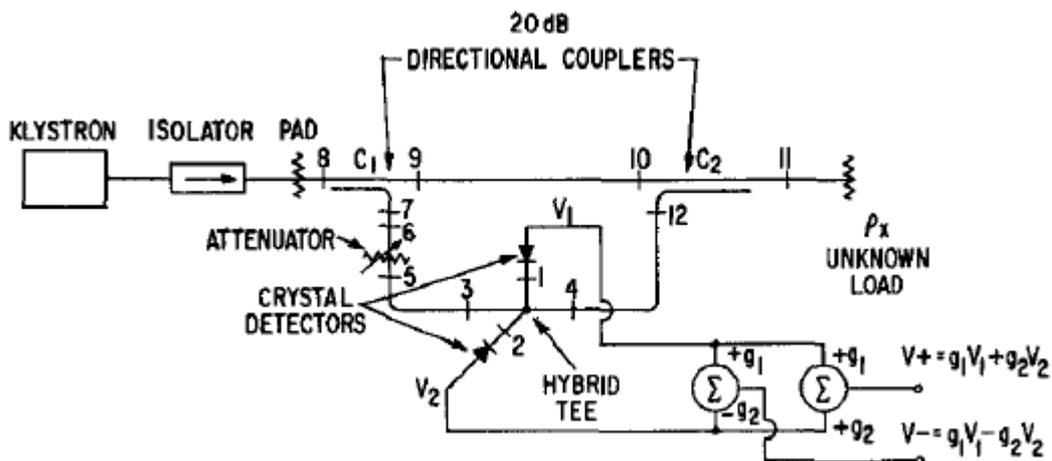
Fig. 2.12 - Schematic representation of the Γ_L measurement method published in [9]. Two directional couplers are sampling the incident and reflected waves, which are later used as the inputs of a hybrid T.

21

Considering the size limitations present in modern applications, more recent approaches focused strongly on reducing the total area of the detection circuit. An interesting example was introduced by K. Hoffmann in [10]. His design suggests placing a "Perturbation error box" in between the device under test and a scalar network analyser.

It was presented the fact that using two magnitude detectors alone can only lead to the calculation of the magnitude of Γ_L. However, using only two magnitude detectors but making several independent measurements can lead to finding the full complex result. A remarkable design was proposed by [11], which uses only two detection ports, among which one of them, for example P_4, is sampled three times by the use of a sliding reflector. The schematic for this circuit is presented in Fig. 2.13.
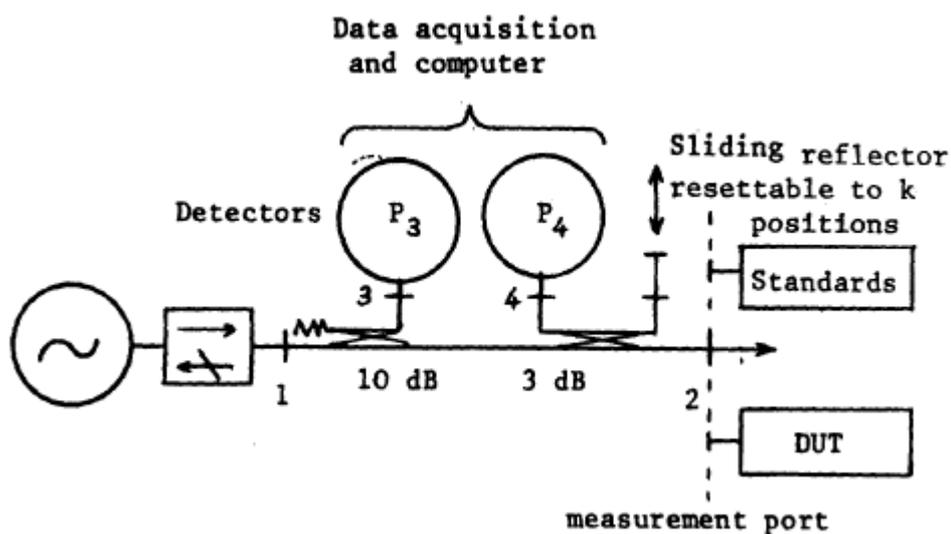
Fig. 2.13 - Block diagram representation of the Γ_L measurement method published in [11]. Multiple positions of a sliding reflector are analysed by reading the corresponding detector indications. A system of equations is then formed in order to solve for the complex reflection coefficient.

Another similar circuit is described in [12]. It uses two power detectors together with a variable attenuator to collect multiple power readings. All of them are used to calculate the complex value of Γ_L. The block diagram of this circuit is represented in Fig. 2.14.
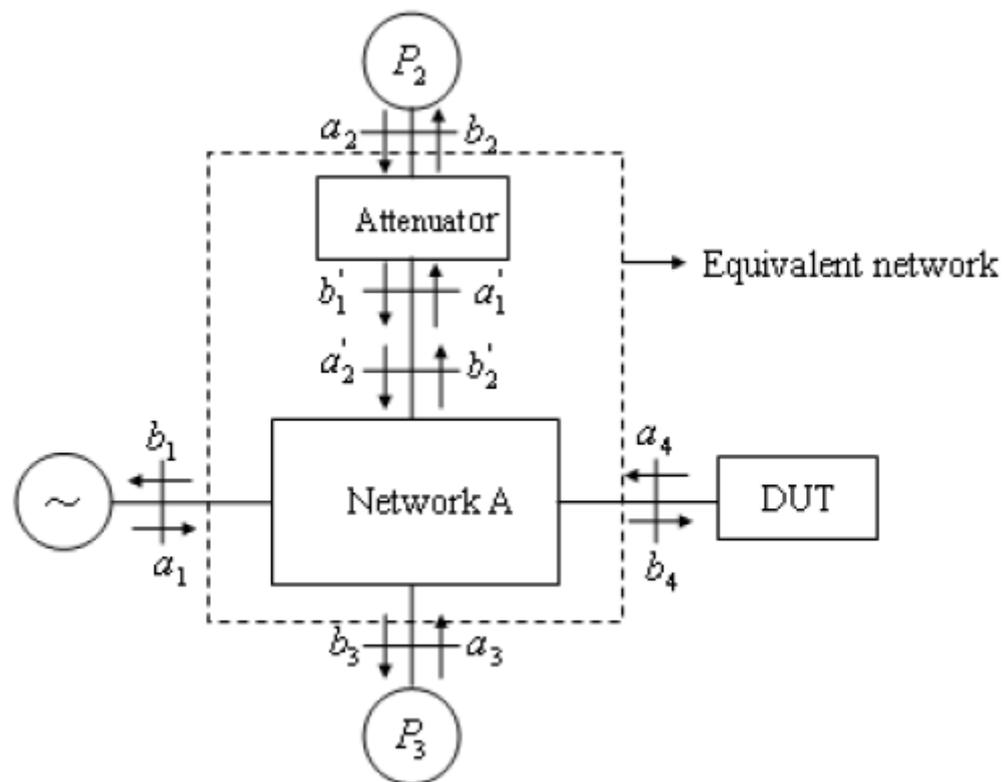
Fig. 2.14 - Block diagram representation of the Γ_L measurement method published in [12]. Having a similar architecture with the method described in [10], this circuit uses a variable attenuator in order to obtain multiple readings for the same unknown load represented by the DUT.

All the techniques of measuring the reflection coefficient presented so far assumed a physical connection between the main line and the measuring mechanism. In practice it is not always possible to interfere with the main line in order to couple power from it. Therefore in this sense, contactless ways of measuring the reflection coefficient were also developed. An easy way to couple power from a main line is to place a secondary line close to it, creating then a coupled line directional coupler. Using a downconverting method, the complex value of the reflection coefficient cand then be calculated. Extensive design recommendations for coupled line couplers exist on this matter, good ones being found on [13] and [14]. Other ways of coupling power using more advanced equipment have also been reported, as in [15], or [16]. Paper [15] describes a way to couple power into a loop coupled port. The classical way of determining the magnitude of the reflection coefficient from coupled powers is them followed. Paper [16] presents an innovative way of measuring the reflection coefficient making use of the bondwire arrays present in any power transistor package. An EM probe is placed on the top of the bondwire array in order to collect the vertical component of the electric field, as presented in Fig. 2.15.
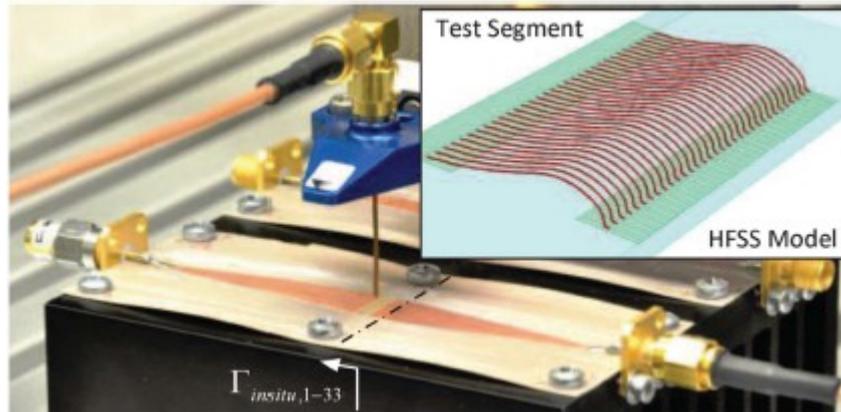
Fig. 2.15 - Experimental setup presenting the EM probe placed above the bondwire array for the reflection coefficient calculation method published in [16].

Using this component which is related to the scattered and incident voltages, a system of equations can be formed in order to calculate the complex reflection coefficient.

It is important to mention that the application analysed in this work also makes use of the bondwires as the main power medium. It is therefore not possible to physically contact them in order to couple the required fraction of power. The directional coupler implementation that will be introduced in Chapter 3 will aim at a contactless approach, while still keeping a good set of performance factors.

So far all the presented measurement techniques used two detection ports to determine the (complex) value of the reflection coefficient of an unknown load. An important milestone in this kind of measurements was achieved with the introduction of *multi detection ports networks*, which make use of more than two detection points in order to calculate the reflection coefficient. The most important advantage of this approach is that it is possible to calculate Γ_L in a complex way by only using voltage magnitudes, therefore eliminating the need of other external devices such as phase shifters or mixers, and also eliminating the need to make several independent measurements for the same output load. A *five port reflectometer* for measuring the reflection coefficient was described in [17]. Its block diagram is presented in Fig. 2.16.
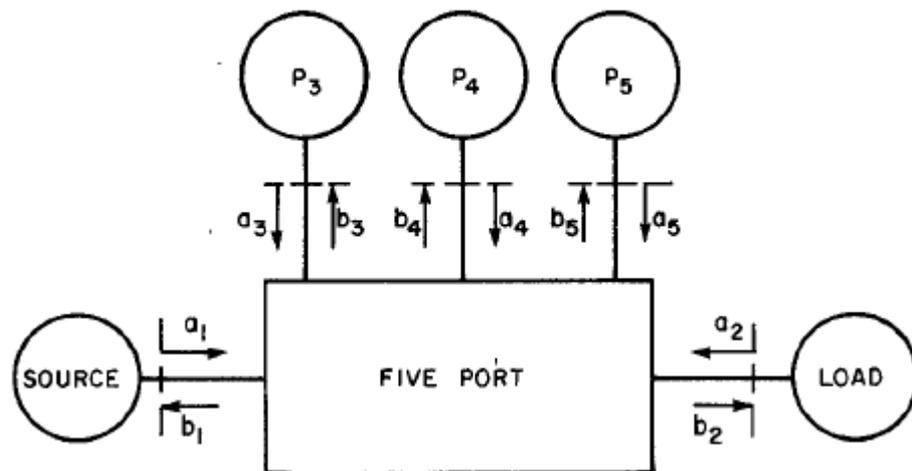
Fig. 2.16 - Block diagram representation of the Γ_L measurement method published in [17]. Three power detectors are used simultaneously to calculate the complex value of the reflection coefficient without making multiple measurements for a particular unknown load.

The three detection ports (P_3, P_4, and P_5) are used to locate the complex Γ_L value in the Γ_L plane. This is done by creating three circular loci of possible Γ_L values, as obtained using each two of them in a pair. Some ambiguity regarding the sign of both real and imaginary parts of Γ_L is present, but these can be eliminated by the use of a couple of known standards.

The same principle of the five port measuring network was implemented also in a simplified form, with only one detection port and a slotted line. This work is presented in [18] and as a block diagram in Fig. 2.17.
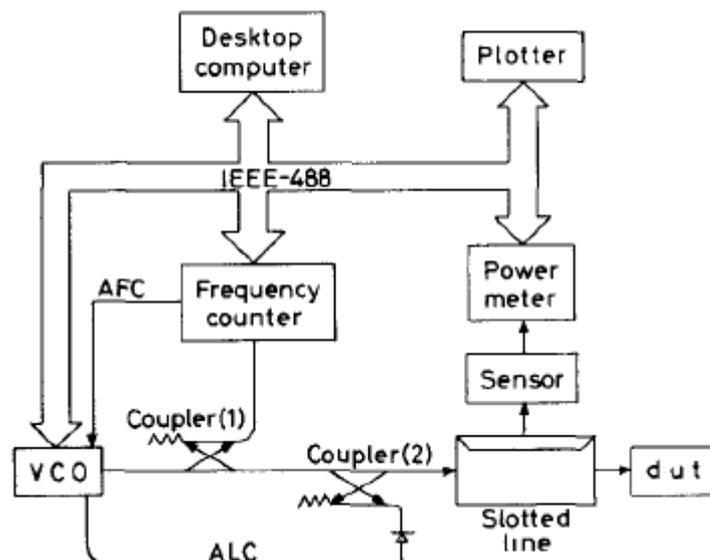
Fig. 2.17 - Block diagram representation of the Γ_L measurement method published in [18]. A slotted line is used to obtain three power readings needed for a similar approach like in the case of the five port reflectometer.

The measurement process is divided in two parts. First, using a matched load at the output port, three powers are obtained at the detection port by taking three positions of the

slotted line. Then, the matched load is disconnected and the unknown load is placed in. Taking again the three power readings at the same positions on the matched load and normalizing them to the values determined previously leads to a system of equations that can be solved for the real and imaginary parts of Γ_L.

It was stated that the five port reflectometer implementation leads in the end to some ambiguity regarding the sign of the determined reflection coefficient. By adding another detection port, the ambiguity can be completely removed. This implementation is called a *six port reflectometer*, and during the last decades has become one of the main ways of performing the reflection coefficient measurement. As the six port implementation is also mostly the subject of this work, a lot more details about its functionality and design will be individually presented in Chapter 4.

2.6   Conclusions

This chapter presented a theoretical background related to the most important goal of this work, measuring the reflection coefficient at the output of a power transistor. As it can be seen, there are various ways in which this can be done. Some of them were also investigated during the course of this thesis. The chapters describing the directional coupler (Chapter 3) and the six port reflectometer (Chapter 4) will give a lot more information about the design steps that were taken in order to implement the best version of these detection circuits. The chapter on measurement results (Chapter 7) will present all the most important results obtained and explain their significance.

References

[1] I. J. Bahl, "Lumped Elements for RF and Microwave Circuits", Artech House, January 2003, p. 365.

[2] M. Spirito, "Enhanced Techniques for the Design and Characterization of RF Power Amplifiers", 2005, p. 65.

[3] Z. Ma, E. Yamashita, "Port Reflection Coefficient Method for Solving Multi-Port Microwave Network Problems", IEEE Transactions on Microwave Theory and Techniques, vol. 43, no. 2, February 1995.

[4] P. J. Probert, J. E. Carroll, "Design features of multi-port reflectometers", Microwaves, Optics and Antennas, IEE Proceedings, 1982.

[5] G. F. Engen, "The Six Port Reflectomter: An Alternative Network Analyzer", IEEE Transactions on Microwave Theory and Techniques, vol. MTT-25, no. 12, December 1977.

[6] W. E. Caswell, "The Directional Coupler", IEEE Transactions on Microwave Theory and Techniques, February 1966.

[7] B. A. Galwas, "Measurement of Reflection Coefficient by Means of Slotted

Line and Homodyne Detection System", IEEE Transactions on Instrumentation and Measurement, vol. IM-24, no. 3, September 1975.

[8] R. J. King, R. I. Christopherson, "Homodyne System for the Measurement of Microwave Reflection Coefficients", IEEE Transactions on Instrumentation and Measurement, September 1970.

[9] G. H. Glover, "Simple Technique for Real-Time Measurement of Complex Reflection Coefficient", IEEE Transactions on Instrumentation and Measurement, July 1970.

[10] K. Hoffmann, "A Novel Vector Network Analyzer", IEEE Transactions on Microwave Theory and Techniques, vol. 46, no. 12, December 1998.

[11] L. C. Oldfield, "A Multistate Reflectometer", IEEE Transactions on Instrumentation and Measurement, vol. IM-34, no. 2, June 1985.

[12] Q. Sui, K. Wang, L. Li, "The Measurement of Complex Reflection Coefficient

by Means of an Arbitrary Four-Port Network and a Variable Attenuator", Proceedings of International Symposium on Signals, Systems and Electronics ISSSE 2010.

[13] T. G. Bryant, J. A. Weiss, "Parameters of Microstrip Transmission Lines and of Coupled Pairs of Microstrip Lines", IEEE Transactions on Microwave Theory and Techniques, vol. MTT-16, no. 12, December 1968.

[14] E. G. Cristal, L. Young, "Theory and Tables of Optimum Symmetrical TEM-Mode Coupled Transmission Line Directional Couplers", IEEE Transactions on Microwave Theory and Techniques, vol. MTT-13, no. 5, September 1965.

[15] K. Yhland, J. Stenarson, C. Wingqvist, "Noncontacting measurement of reflection coefficient and power in planar circuits up to 40 GHz", ARFTG Conference, 2007.

[16] R. Hou, M. Spirito, B. J. Kooij, F. Van Rijs, L. C. N. De Vreede, "Contactless Measurement of In-circuit Reflection Coefficients", Microwave Symposium Digest (MTT), 2012 IEEE MTT-S International.

[17] S. Li, R. G. Bosisio, "The Measurement of Complex Reflection

Coefficient by Means of a Five-Port Reflectometer", IEEE Transactions on Microwave Theory and Techniques, vol. MTT-31, no. 4, April 1983.

[18] E. Martin, J. Margineda, J. M. Zamarro, "An Automatic Network Analyzer Using a Slotted Line Reflectometer", IEEE Transactions on Microwave Theory and Techniques, vol. MTT-30, no. 5, May 1982.

3. Compact directional coupler

3.1 Introduction

The main goal of this work is to design a package integrated way of measuring the reflection coefficient at the output port of a power transistor. In Chapter 2 various ways of measuring the reflection coefficient were introduced together with their advantages and disadvantages. Also, a review of the most remarkable literature published regarding this kind of measurements was presented. By reading the previous chapter, it can be observed that a lot of well-known implementations targeting this problem make use of a directional coupler. This device, which was also briefly described before, is used as a simple and cheap solution to determine the magnitude of the reflection coefficient of any output loading condition, or its complex value, if a downconverting method is used. Therefore, the directional coupler had also its certain amount of attention in this current work.

3.2 Directional coupler theory

Before advancing to the design of the proposed directional coupler, it is very important to present the basic theory behind the functionality of this device. To do so, a start will be made from the most basic implementation, which is a set of two coupled lines placed in close proximity to each other. This implementation is presented graphically in Fig. 3.1.
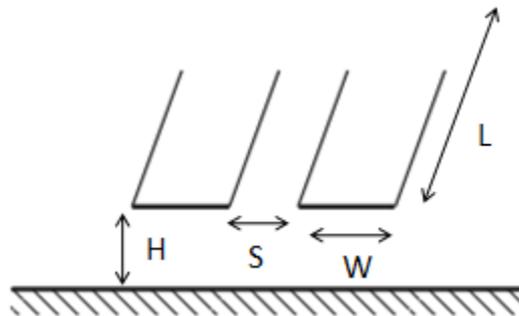
Fig. 3.1 – Drawing of a pair of identical coupled lines.

From Fig. 3.1 a first idea about the design parameters of such a directional coupler can be made. Inspecting the presented drawing, it can be seen that the physical parameters that can be varied are the length of the coupled section (L), the spacing between the two lines, (S), and the height on which the two lines are placed with respect to the ground plane, (H). The last parameters, the width of the lines (W) does also have an important role, especially in designing a coupler with specific characteristic impedance. To start the discussion about the design of such couplers, and how the design parameters influence their electric properties, two particular

cases will be discusses: the case of symmetric coupled lines, and the case of coupled lines with different geometries.

3.2.1   The case of symmetric coupled lines

If the two lines that create the coupled line directional coupler are identical with respect to their geometries (same length, same width, same height over the ground plane), then both of them will have the same characteristic impedance, and the resulted directional coupler will be a symmetric line coupler. To start the analysis of this coupler, a deeped inspection of Fig. 3.1 will be done. If TEM conditions are assumed, the coupler created by the presented two lines can be completelly modelled by the effective capacitances between the lines, and the velocity of propagation along the lines. The schematic of the capacitances describing a general directional coupler is presented in Fig. 3.2.
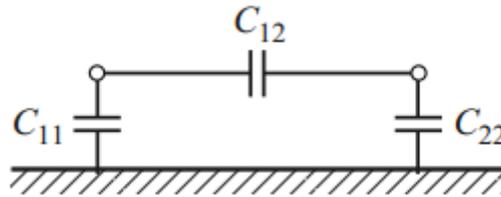
Fig. 3.2 – Schematic drawing of the thre capacitances describing the behavior of the directional coupler.

As it can be observed by analysing the capacitances schematic and the coupler design, C_{12} represents the capacitance between the two lines, while C_{11} and C_{22} represent the capacitance between each of the lines and the ground plane. As in this first analysis the lines are assumed to be equal, C_{11} will be equal to C_{22}. As it will be seen later in this section, the electrical properties of a directional coupler can be completelly determined by the capacitive approximation, and designing the coupler with particular properties (such as its coupling) can be easily done by adjusting the value of these capacitances accordingly.

The design of the coupled lines coupler can be further understood by using the even and odd mode analysis. In the even mode, currents having the same amplitude and direction are injected along the two coupled lines. In the odd mode, the currents along the conductors have again the same amplitude, but opposite directions.

Considering the even and odd mode analysis, and the previously introduced capacitive model, it is possible to calculate the even and odd mode capacitances of either line to ground. In the even case, the capacitive circuit has simmetry about the center line, as the C_{12} capacitor is shorted. The, the even mode capacitance can be defined as as in Eq. 3.1.

$$C_e = C_{11} = C_{22} \qquad (3.1)$$

By performing a similar analysis for the odd mode, the odd mode capacitance between the conductors and ground is found to be:

$$C_o = C_{11} + 2C_{12} = C_{22} + C_{12} \qquad (3.2)$$

With the newly introduced even and odd mode capacitances, the even and odd mode impedances for the two coupled lines can be defined, as presented in Eq. 3.3 and 3.4.

$$Z0e = \frac{1}{vpCe} \qquad (3.3)$$

$$Z0o = \frac{1}{vpCo} \qquad (3.4)$$

In the above relations, Co and Ce are the even and odd mode capacitances, while vp is the velocity of propagation along the lines,

$$vp = \frac{c}{\sqrt{\varepsilon_r}} \qquad (3.5)$$

If the directional coupler is located in a homogenous medium, this propagation velocity is equal in both even and odd modes. Having different velocities leads to a decrease in the couplers directivity, and ways of compensating the difference between these two velocities have been analysed in literature, as it will be presented in section 3.2.3. With the even and odd mode characteristic impedances defined above, an even and odd mode approach can be taken in order to analyze the performance of the directional coupler. An excellent explanation of this method was presented in [1], and this will represent the basis of the further derivation.

The directional coupler presented in Fig. 3.1 is drawn again in Fig. 3.3, this time having terminating impedances equal to Z_0 at ports 2, 3 and 4, and a generator of $2V_0$ with an internal impedance of Z_0 at port 1. Teta represents the electrical length of the coupler section, and the voltages and currents resulted at all the four ports are also illustrated.
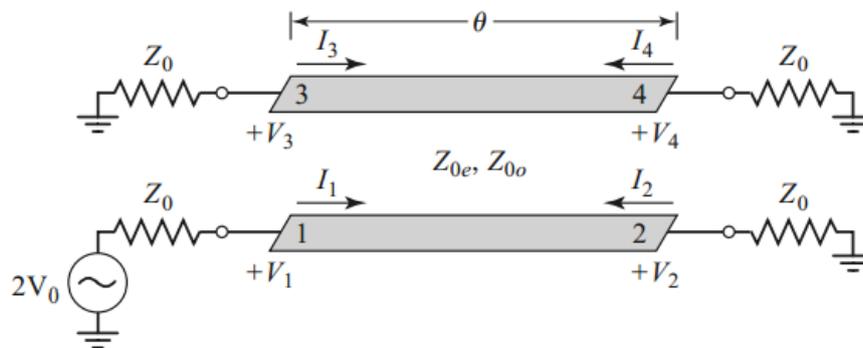
Fig. 3.3 – Representation of the coupled line directional coupler with terminating impedances and input voltage source.

The even and odd mode decomposition of the schematic in Fig 3.3 is presented Fig. 3.4 and Fig. 3.5.
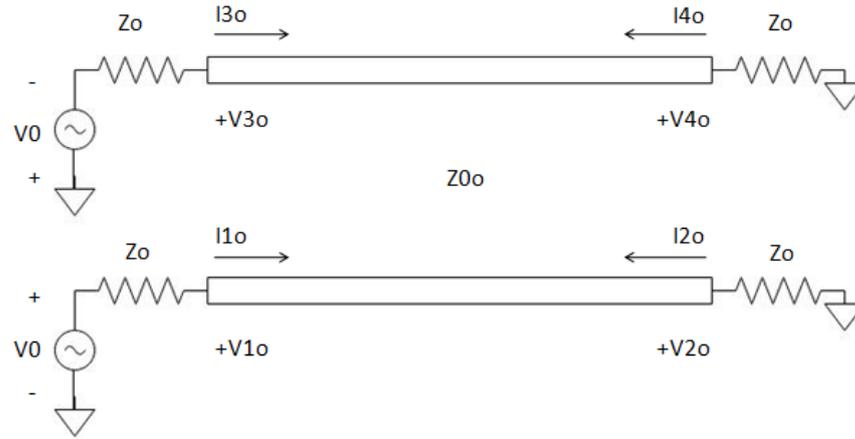
Fig. 3.4 – Odd mode analysis of the coupled line directional coupler.
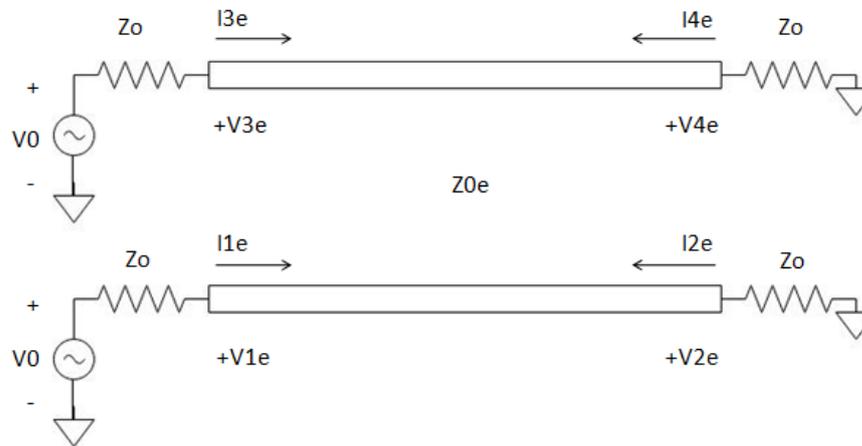
Fig. 3.5 – Even mode analysis of the coupled line directional coupler.

It can be seen that the only difference between Fig 3.4 and Fig 3.5 represents the different polarities of the applied input voltages. In terms of the even and odd impedances, Z_0 and the electrical length, the imput impedance in the odd and even cases at port 1 can be written as:

$$Zin, e = Z0e \frac{Z0 + jZ0e * tan\theta}{Z0e + jZ0 * tan\theta} \qquad (3.6)$$

$$Zin, 0 = Z0o \frac{Z0 + jZ0o * tan\theta}{Z0o + jZ0 * tan\theta} \qquad (3.7)$$

As a function of the even and odd mode voltages and current at port 1, the input impedance is:

$$Zin = \frac{V1, e + V1, o}{I1, e + I1, o} \qquad (3.8)$$

The even and odd mode voltages and currents can be specified in terms of the input voltage V_0, by means of voltage division. They can be expressed as:

$$V1, o = V0 \frac{Zin, o}{Zin, o + Z0} \qquad (3.9)$$

$$V1, e = V0 \frac{Zin, e}{Zin, e + Z0} \qquad (3.10)$$

31

$$I1, o = \frac{V0}{Zin,o+Z0} \qquad (3.11)$$

$$I1, e = \frac{V0}{Zin,e+Z0} \qquad (3.12)$$

Replacing the relations (3.9)-(3.12) into the previously defined input impedance (3.8) leads to:

$$Zin = Z0 + \frac{2(Zin,o*Zin,e-Z_0^2)}{Zin,e+Zin,o+2Z0} \qquad (3.13)$$

For a symmetrical coupled line coupler, the relation between the coupler's characteristic impedance and its even and odd mode impedances is:

$$Z0 = \sqrt{Zo,e*Zo,o} \qquad (3.14)$$

Using this relation back in (3.6)-(3.7) leads to:

$$Zin, e = Zo, e * \frac{\sqrt{Zo,o}+j*\sqrt{Zo,e}*tan\theta}{\sqrt{Zo,e}+j*\sqrt{Zo,o}*tan\theta} \qquad (3.15)$$

$$Zin, o = Zo, o * \frac{\sqrt{Zo,e}+j*\sqrt{Zo,o}*tan\theta}{\sqrt{Zo,o}+j*\sqrt{Zo,e}*tan\theta} \qquad (3.16)$$

By analysing relations (3.15) and (3.16) it can be seen that the product of the even and odd mode input impedances will be equal to the product of the even and odd mode characteristic impedances, and thus to the square root of the coupler's characteristic impedance. By using this back in (3.13), it results that as long as (3.14) is satisfied, the input impedance of the directional coupler will be equal to the coupler's characteristic impedance, and therefore the coupler will be mached at the input port. By symmetry, it means that also the other three ports will be matched.

Reffering back to Fig. 3.4 and Fig. 3.5, the voltage at port 3 of the directional coupler can be written as

$$V3 = V3, o + V3, e = V0 * \left[\frac{Zin,e}{Zin,e+Zo} - \frac{Zin,o}{Zin,o+Zo}\right] \qquad (3.17)$$

Again making use of the even and odd mode input impedance definitions (3.6)-(3.7) and the relation (3.14), the voltage at port 3 can be related to the voltage at port 1, such that:

$$V3 = V1 * \frac{j(Z0,e-Z0,o)tan\theta}{2Z0+j(Z0,e+Z0,o)tan\theta} \qquad (3.18)$$

Deviding both of the sides by V_1, we have

$$\frac{V3}{V1} = \frac{j(Z0,e-Z0,o)tan\theta}{2Z0+j(Z0,e+Z0,o)tan\theta} \qquad (3.19)$$

Considering the fact that port 3 is the coupled port of the directional coupler in the case of a backwave coupler, it means that the ratio defined in (3.19) represents the voltage coupling factor of the directional coupler.

By defining

$$C = \frac{Z0,e-Z0,o}{Zo,e+Z0,o} \qquad (3.20)$$

Relation (3.19) can be rewritten as

$$\frac{V3}{V1} = \frac{jCtan\theta}{\sqrt{1-C^2}+jtan\theta} \qquad (3.21)$$

where C is called the midband coupling factor.

By inspecting (3.21), it can be seen that the coupling factor varies with the electrical lenght of the coupled section. At low lengths, the coupling is small, and almost all the signal applied at port 1 reaches port 2, the throgh port. However, if θ is set at 90˚, relation (3.21) becomes.

$$\frac{V3}{V1} = C \qquad (3.22)$$

By observing (3.21), it can be seen that the coupling fact has a sinusoidal variation with the electrical lenght of the coupler. This variation is presented in Fig. 3.6.
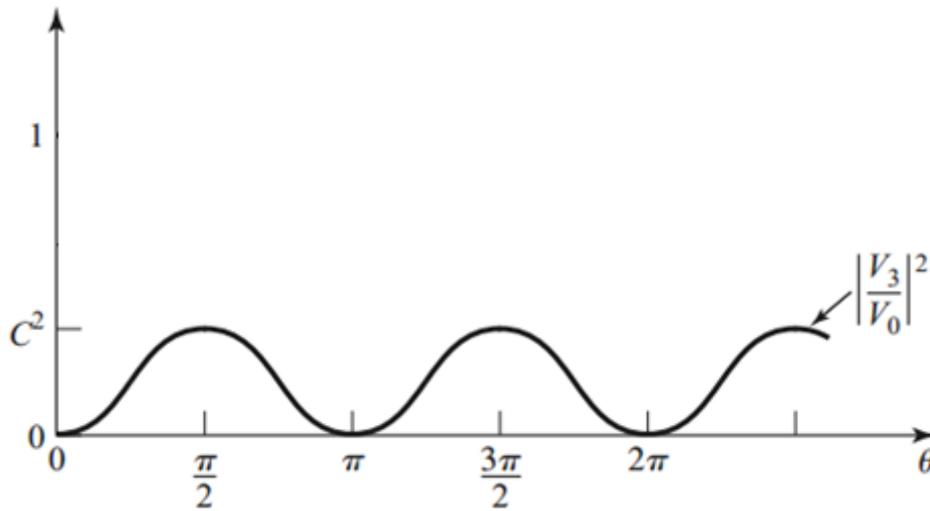
Fig. 3.6 – Variation of the coupling factor as a function of the electrical length of the conductors.

It can be seen that the peaks of the sinusoidal, which represent the maximum coupling, occur at multiples of 90˚. Because of the easy relation between the coupling factor and the even and odd mode impedances which exists at these lengths, this is how directional couplers are usually designed. Moreover, for minimum size matters, the electrical length of 90˚ is usually picked, as this is the electrical lenght at which the first coupling maximum occurs.

If the length of the directional coupler is set to 90˚, than a direct relation between the coupling factor and the even and odd mode impedances can be derived, as presented in (3.23) and (3.24).

$$Zo,e = Zo\sqrt{\frac{1+C}{1-C}} \qquad (3.23)$$

$$Zo,o = Zo\sqrt{\frac{1-C}{1+C}} \qquad (3.24)$$

By using these equations, a λ/4 directional coupler with any arbitrary coupling factor can be designed, as long as the correct even and odd impedances are achieved.

It was stated earlier that the physical parameters of the coupled line structure can be tuned in order to achieve the desired electrical properties of the coupler. In particular, the length of the coupled structure and the spacing between the two conductors are very important in designing for a particular coupling level. As it was presented in the above discussion, for coupled lines having a certain characteristic impedance, the maximum coupling that can be obtained occurs when the paralel conductors are λ/4 (90˚) long. Therefore, tuning the length of the coupled lines to this value assures that the maximum coupling between the lines is obtained. In practice this can lead to large designs, especially at low frequncies. Shorter lengths of coupled lines can also be used, but the resulted coupling between ports 1 and 3 gets lower as the length of the conductor is decreased.

To present this situation, a simple situation of two coupled lines in air is investigated. The Ansys HFSS drawing of the presented situation is shown in Fig. 3.7.
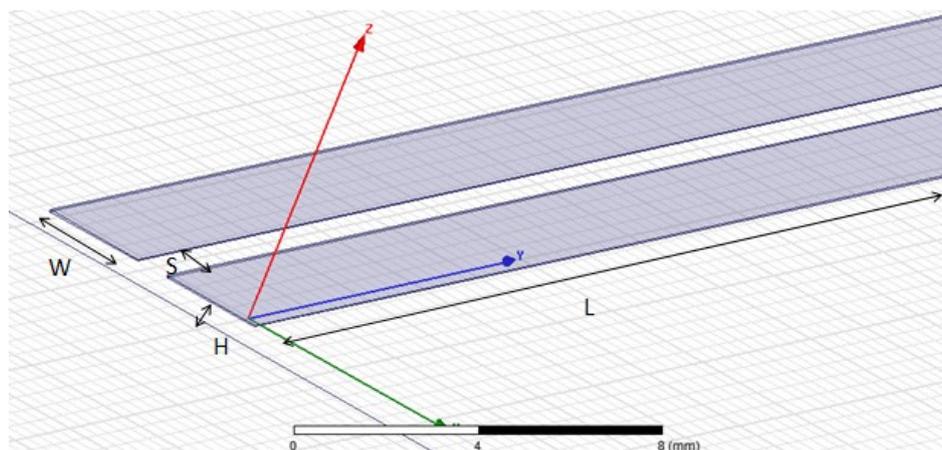
Fig. 3.7 – HFSS schematic of two coupled conductor lines in air.

In the above drawing L represents the length of the coupled lines, S is the spacing between them, H is the heingth over the ground plane and W is the width of both lines.

Initially these four geometry parameters were adjusted for a coupling factor of 20 dB, in the case of λ/4 long conductors. The resulted valued for this case are W=2.4 mm, L=30.6 mm, H=0.5 mm and S=0.8 mm. All the ports were matched to the characteristic impedance of a line, which was chosen to be 50 Ω. To inspect the impact of conductor lenght on the coupling factor, a sweep was performed on this parameter. The resulted coupling factor versus the length of the conductors is plotted in Fig. 3.8.
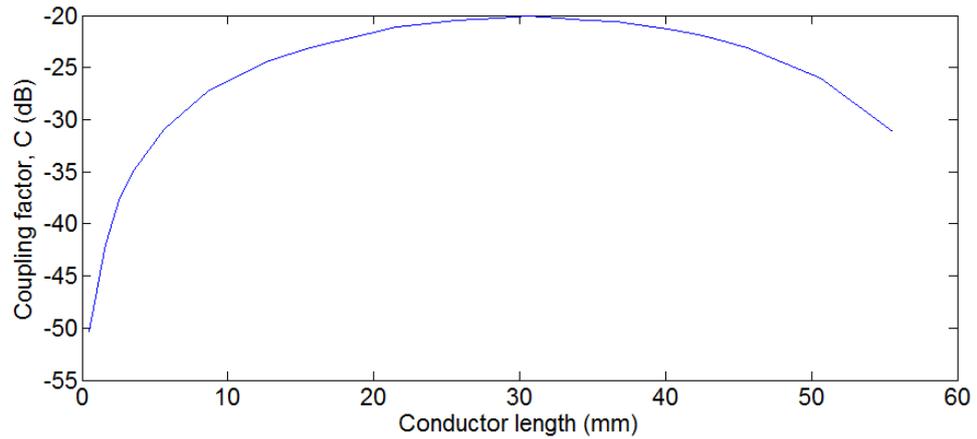
Fig. 3.8 – Simulated coupling factor versus conductor length for the coupler in Fig. 3.7.

It can be seen that indeed the coupling factor has its maximum value when the conductos have $\lambda/4$ length, or for a 2.45 GHz central frequency, 30.6 mm. For lengths lower than $\lambda/4$, the coupling is decreasing when the length is decreased. For lengths larger than $\lambda/4$ and shorter than lambda/2 the coupling factor will again decrease with the increase in length, and finally between $\lambda/2$ and $3\lambda/4$ will start to increase again with the increase in length. The next peak coupling point will happen at a conductor length of $3\lambda/4$, or 91.8 mm at the design frequency.

Another way to influence the amount of coupling between these ports is by adjusting the spacing between the coupled lines. This becomes more evident by inspecting again relation (3.20). Here it can be seen that by increasing the value of the odd mode characteristic impedance, the resulting coupling factor is decreased. By observing the way in which the odd mode impedance is defined (3.4), it can be seeen that an increase in its value means a decrease in the value of the odd mode capacitance. Finally, observing the definition of the odd mode capacitance (3.2), it can be seen that its value can be decreased by decreasing the mutual capacitance between the two connectors, C_{12}. This translates to an increase in the spacing between the two conductors placed at the same height from the ground plane. In conclusion, increasing the spacing between the two conductors leads therefore to a decrease in the coupling factor, assuming that all the other design parameters are kept constant.

To illustrate this situation, the same set of symettrical coupled lines from Fig. 3.7 will be used, this time the swept parameters being the spacing between the two of them. The coupling factor for the obtained directional coupled as a function of the spacing between the conductors is presented in Fig. 3.9.
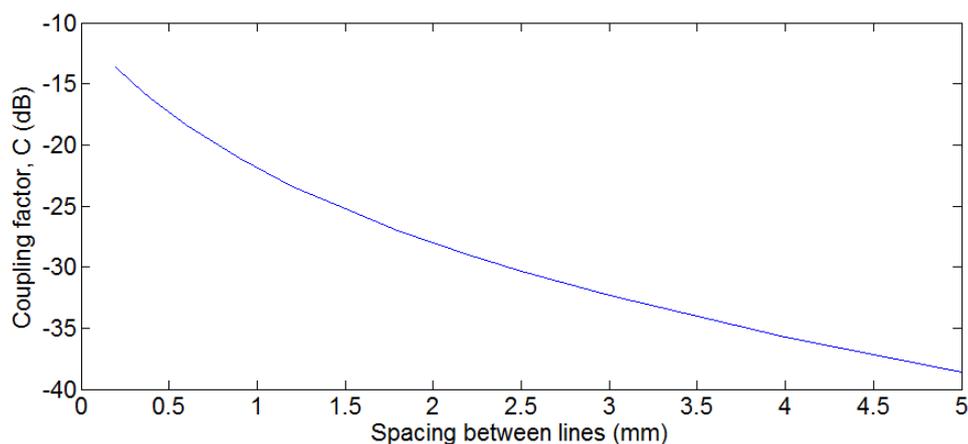
Fig. 3.9 – Coupling factor as a function of spacing between the conductors for the coupler presented in Fig. 3.7.

It can be seen that the coupling factor drops as the separation between the conductors is increased, which matches with the theoretical expectation.

3.2.2   The case of assymetric coupled lines

The previous section presented an analysis of symmetric coupled lines directional couplers. The symmetry in the considered cases comes from the fact that the two coupled structures have the same geometry in terms of width, length, spacing and height over the ground plane. However, in practice it is not always possible or desired to design a coupler in which both the conductors have the same shape and geometry. Also, the application that makes the subject of this work will represent a case in which the two structures making the directional coupler are not symmetrical. The proposed implementation will make use of the bondwire array existent inside a power transistor package as the main line of the coupler, and an additional element as the coupled line. While the coupled element can be designed to have certain electrical parameters (for example, Z_0=50 Ω), the bondwire array represents also part of the output matching network of the transistor, and therefore the impedances at its terminals will not always have 50 Ω. Also, by varying the height of the bondwires in the array, these impedances are again changed. This is why in certain applications like the presented one, it is important to design an assymetric directional coupler. The analysis of these types of couplers can be found in several examples of publications [2] [3], and a brief discussion about them will follow in this sub section.

For simplification, the easiest way to design an assymetrical coupler is by using two uniformly coupled lines of different characteristic impedance. Relating back to Fig. 3.1, this situation means that the geometry of the two coupled lines is not the same. Different characteristic impedances for the two lines can be achieved in various cases, among which varying the width of one the lines, or varying the height over the ground plane of one of the

lines. An example of an assymetrical line coupler made by having lines with different width is presented in Fig. 3.10.
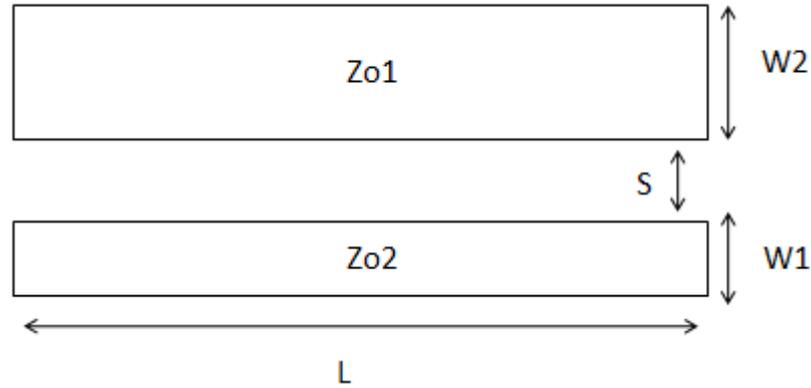
Fig. 3.10 – Assymetric coupled line directional coupler with lines of different widths.

Even if the two coupled lines are not symmetrical anymore, the capacitance model describing their coupling shown in Fig. 3.2 does still apply. The only difference is that in this situation the two capacitances to ground C11 and C22 will not be equal anymore. Based on the three capacitances present in this model, the capacitance matrix describing the two coupled lines, C, can be defined as follows:

$$C = \begin{bmatrix} C11 + C12 & -C12 \\ -C12 & C22 + C12 \end{bmatrix}$$

Paper [2] offers quick and very useful closed form solutions for the capacitances present in the C matrix, as follows:

$$\frac{C11}{\varepsilon} = \frac{376.7(Ga - k\sqrt{GaGb})}{\sqrt{\varepsilon_r}\sqrt{1-k^2}} \qquad (3.25)$$

$$\frac{C22}{\varepsilon} = \frac{376.7(Gb - k\sqrt{GaGb})}{\sqrt{\varepsilon_r}\sqrt{1-k^2}} \qquad (3.26)$$

$$\frac{C12}{\varepsilon} = \frac{376.7 * k\sqrt{GaGb}}{\sqrt{\varepsilon_r}\sqrt{1-k^2}} \qquad (3.27)$$

In the above equations G_a and G_b are the inverse of the impedances of the two coupled lines, and k is the coupling factor in a fractional form. Based on these equations, the three capacitances in Fig. 3.2 can be calculated in terms of the impedances present at the four ports of the directional coupler, and also the coupling factor k.

A deeper mathematical analysis of an (assymetric) directional coupler in terms of the voltages and currents present at its four ports will be derived next. This derivation will present in the end the Z matrix of the four port network as a function of the capacitances in the capacitance matrix, C.

In order to start, let's consider the case of n+1 conductor coupled lines. For these, the differential equations in the frequency domain written in matrix form are:

$$\frac{d}{dx}V = -ZI \qquad (3.28)$$

$$\frac{d}{dx}I = -YV \qquad (3.29)$$

In the above equations V is the n elements vector for line voltages, and I is the n element vector for line currents. We can further define Z and Y as

$$Z = R + j\omega L \qquad (3.30)$$

$$Y = G + j\omega C \qquad (3.31)$$

Where R, L, G and C are n x n symmetrical matrixes related to the properties of the network of n+1 coupled conductors.

A set of n+1 conductor coupled lines can be expressed and treated as a 2n-port etwork, with n port on the sending side and n ports on the receiving side, as presented in Fig. 3.11.
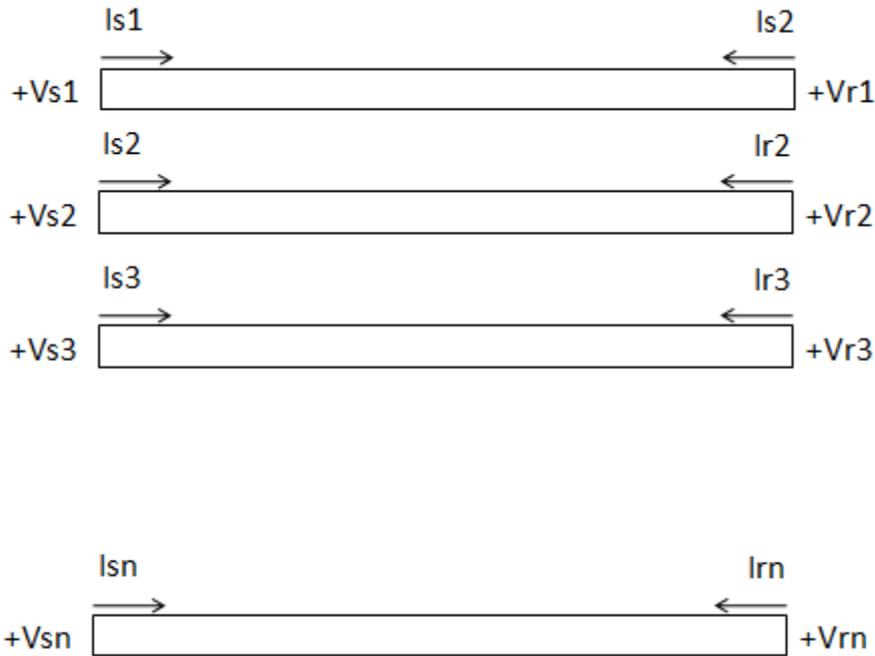
Fig. 3.11 – Currents and voltages at the ports of n coupled conductors.

Using the notations in Fig. 3.11, we can define the sending voltages vector (Vs), the receiving voltages vector (Vr), the sending currents vector (Is) and the receiving currents vector (Ir). All these vectors have n elements.

The above introduced vectors can be connected to each other in a matrix form. This matrix form relation is presented below.

$$\begin{bmatrix} Is \\ Ir \end{bmatrix} = \begin{bmatrix} Yo \coth(\Gamma d) & -Yo \operatorname{csch}(\Gamma d) \\ -Yo \operatorname{csch}(\Gamma d) & Yo \coth(\Gamma d) \end{bmatrix} \begin{bmatrix} Vs \\ Vr \end{bmatrix} \qquad (3.32)$$

$$\begin{bmatrix} Vs \\ Vr \end{bmatrix} = \begin{bmatrix} \coth(\Gamma d)Zo & \operatorname{csch}(\Gamma d)Zo \\ \operatorname{csch}(\Gamma d)Zo & \coth(\Gamma d)Zo \end{bmatrix} \begin{bmatrix} Is \\ Ir \end{bmatrix} \qquad (3.33)$$

Where $\Gamma = (ZY)^{1/2}$, $Y_0 = Z^{-1}\Gamma$, $Z_0 = Y_0^{-1}$ and d is the length of the conductor.

By using the notations

$$Za = \coth(\Gamma d)Y_0^{-1} \qquad (3.34)$$

$$Zb = \text{csch}(\Gamma d)Y_0^{-1} \qquad (3.35)$$

We can define the open circuit impedance matrix as

$$Z = \begin{bmatrix} Za & Zb \\ Zb & Za \end{bmatrix} \qquad (3.36)$$

From this point the derivation of the Z matrix in terms of the C matrix components will continue for the case of n=2 coupled conductors over a ground plane.

First, we have

$$Zo = Yo^{-1} \qquad (3.37)$$

Following the definition of Y_0 we can further write Z_0 as

$$Zo = (j\omega C)^{-1} * \sqrt{j\omega L * j\omega C} \qquad (3.38)$$

Where

$$C = \begin{bmatrix} C11 & C12 \\ C21 & C22 \end{bmatrix}$$

$$L = \begin{bmatrix} L11 & L12 \\ L21 & L22 \end{bmatrix}$$

For a lossless condition, if the conductors are placed in air ($\varepsilon_r = 1$),

$$L = \varepsilon_0 \mu_0 C^{-1} \qquad (3.39)$$

Using these notations and after some manipulation, Zo matrix can be written as

$$Zo = \sqrt{\varepsilon_0 \mu_0} * C^{-1} \qquad (3.40)$$

Now all the components required to determine the Za and Zb matrixes can be calculated, and in the end, the elements of these matrixes written in terms of the C matrix components are found as:

$$Za = \frac{\sqrt{\varepsilon_0 \mu_0}}{C11 C22 - C12^2} \begin{bmatrix} \coth(j\omega\sqrt{\varepsilon_0 \mu_0}d) C22 & -\coth(j\omega\sqrt{\varepsilon_0 \mu_0}d) C12 \\ -\coth(j\omega\sqrt{\varepsilon_0 \mu_0}d) C12 & \coth(j\omega\sqrt{\varepsilon_0 \mu_0}d) C22 \end{bmatrix} \quad (3.41)$$

$$Zb = \frac{\sqrt{\varepsilon_0 \mu_0}}{C11 C22 - C12^2} \begin{bmatrix} \text{csch}(j\omega\sqrt{\varepsilon_0 \mu_0}d) C22 & -\text{csch}(j\omega\sqrt{\varepsilon_0 \mu_0}d) C12 \\ -\text{csch}(j\omega\sqrt{\varepsilon_0 \mu_0}d) C12 & \text{csch}(j\omega\sqrt{\varepsilon_0 \mu_0}d) C22 \end{bmatrix} \quad (3.42)$$

It should be noted that in the case of symmetrical structures, $C_{11} = C_{22}$ and the diagonal terms of the above matrixes are equal. Using relations (3.41)-(3.42) and relation (3.36) it is found that all the terms of the Z impedance matrix are now written in terms of only the elements of the capacitance matrix, which in the end is related to the physical parameters of the two conductors. Using the Z matrix, and relations (3.32)-(3.33) a system of equations can be formed to relate the voltages on all the ports in terms of the capacitance matrix components, such that the amount of coupling between any pair of ports can be determined after some manipulation in terms of the C matrix components.

3.2.3   Couplers shorter than quarter λ

The discussion presented earlier in this chapter stated that in the case of two uniform coupled lines placed paralel, in close proximity to each other, the maximum signal coupling between them occurs when the electrical lenghts of the conductors are set to 90˚. In lenght units, this translates to a conductor length of $\lambda/4$, where λ is the wavelength existent on the conductor. Especially at low frequencies, the wavelength can have large lengths, depending on the value of the substrate's characteristic permitivity. For example, at 2.45 GHz, the central frequency used in most of the derivations made in this work, the wavelength on a $6.5\varepsilon_r$ substrate has a value of 48 mm. In directional couplers design that are not aimed for package integration or very compact layout, these kind of dimensions are not a concern, and the coupler can be easily designed for the desired coupled factor by choosing $\lambda/4$ long conductors and adjusting their parameters such that the even and odd mode impedances are correct. A connecion between the even and odd mode impedances and the coupling factor in the case of lambda/4 long conductor is given in relations (3.23)-(3.24). However, as it was stated from the beginning, this work targeted applications in which the compactness of the designed structure is not only desirable, but also a strict design goal. The full package integration of the mismatch detection mechanism is desired, and as this mechanism will be later developed starting from the use of a directional coupler, the coupler will therefore have to be compact and package integratable. In conclusion, in the presented application, it is not possible to design a coupler having a $\lambda/4$ length. As it was explained in section 3.2.1, by designing a coupler with conductors having length than quarter λ in length, the achieved coupling will be lower than in the case of $\lambda/4$ segments. For conductor length between 0 and $\lambda/4$, the coupling factor will increase together with the increase in conductor's lenght. The conclusions regarding the influence of lenght on the directivity of the designed coupler require more attention, as this property does not depend only on the design parameters (lenght, spacing, height over the ground plane), as also on the type of medium in which the coupler is placed. In cases in which the coupler is placed on a homogenous medium (air, or integrated inside a dielectric with a constant ε_r), the directivity of the resulted design does not vary with the electrical length of the conductors. Moreover, for the case of an ideal, lossless coupler (no dielectric loss, perfect conductive segments, all ports matched), the directivity has an ideal value of infinity. In practice it is not possible to design an ideal coupling, as losses due to the presence of dielectric and non ideal conductivity will always be present. Even so, the case of a matched, uniform directional coupler the directivity should have large values (higher than 30 dB), and should not be influenced by the electrical length. The case of couplers placed in a non-homogenous medium (among which the microstrip lines coupler is an example) requires special attention with respect to the directivity, as this property has now lower values, which are not constant with the electrical lenght. This is because the velocities of propoagation for the odd and even

mode are not equal, since the two modes have different field configurations in the vicinity of the air-dielectric interface. Improving the directivity in these conditions reffers to the task of balacing the two propagation velocities. This method can be used to increase the directivity of a coupler with conductors of any length. Literature studies exist on this matter, and good examples of inhomogenous medium designs with improved directivity can be found in [4]-[8]. The methods of balancing the velocities used in these publications involve dielectric overlay [4], grooved substrates [5], wiggly lines [6], lumped capacitances added to the ends of the conductors [7] or the use of ground plane apperture to the ground plane of the coupler [8]. The reader is adviced to inspect these papers for further design specifications.

3.3 Directional coupler literature review

Extensive literature has been published describing the design and functionality of the directional coupler. Nowadays this device is considered to be one of the most important microwave designs, and it is successfully used in applications such as attenuators, power splitters, hybrid junctions or sampling the forward and reflected waves along a transmission line. Generally the directional coupler can be built either as a waveguide directional coupler or a coupled line directional coupler. Even though not exclusively, the coupler presented in this work is related in many ways to the coupled line directional coupler. For this reason, these kinds of applications will be analysed with more attention during the rest of this section. A lot of guideline papers have been published on the subject of designing the proper directional coupler using coupled lines. Considerations can be given for either designs that have single-section coupled lines [9] [10], or multi-section coupled lines [11] [12]. Figs. 3.12 and 3.13 represent general drawings of how single-section and multi-section microstrip lines can be used in order to create a directional coupler. Also, design recommendations for the layout of interdigitated directional couplers can be found in [13].
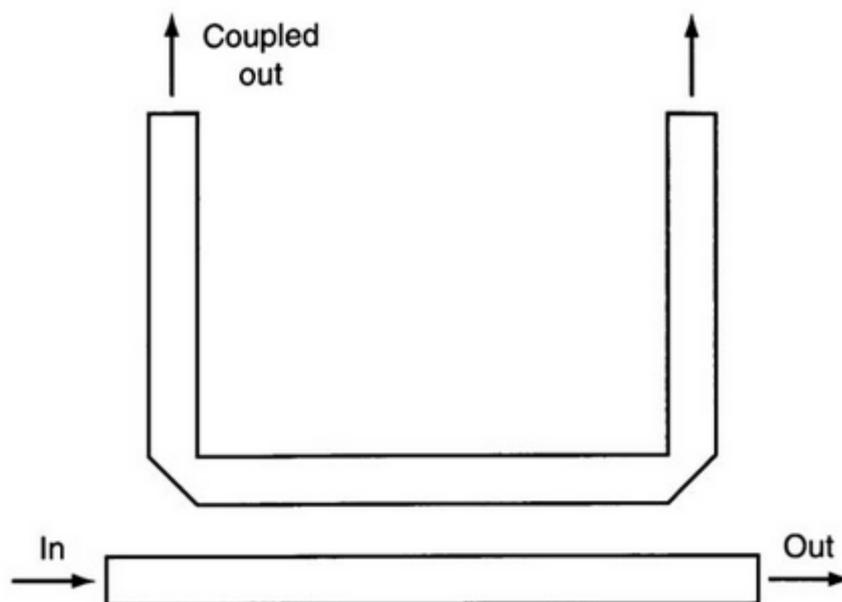
Fig. 3.12 - Basic schematic for a single-section coupled line coupler.
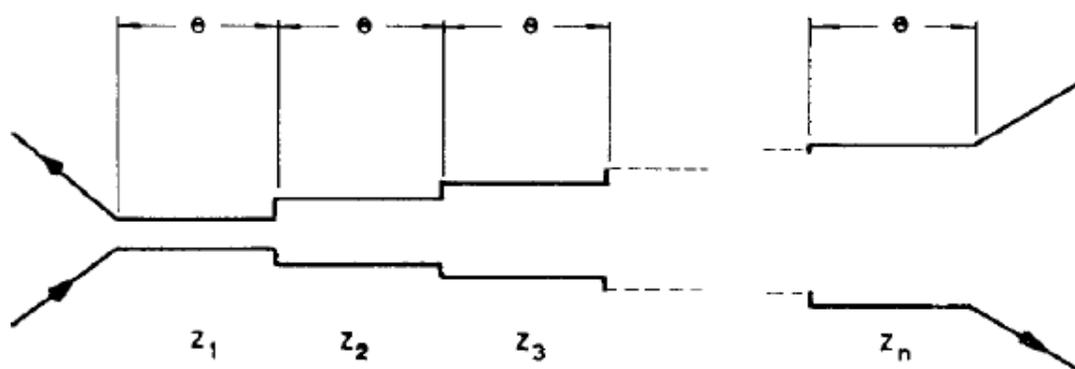
Fig. 3.13 - Basic schematic for a multi-section coupled line coupler.

The use of the directional coupler as a way to measure the reflection coefficient of a device under test has been published since several decades ago. Papers such as [14] describe this kind of usage. As earlier presented in Chapter 2, directional couplers require a relatively high directivity in order to be used as an effective way to determine the magnitude of Γ_L. This is why a lot of work has been put over time in developing better directivity for these kinds of devices. In general, a directivity of over 30 dB can be considered enough to provide accurate Γ_L determination, as it was illustrated in Chapter 2. Ways of designing directional couplers in order to improve their directivity were reported in [15] - [17]. These approaches manage to balance as much as possible the velocity of propagation between the even and odd modes of operation, thus increasing the directivity, as earlier mentioned in section 3.2.

Many different layouts of directional couplers have been published, mostly depending on the type of final application. In applications that require operation over a large range of

frequencies, a broadband coupler is desirable. Examples of such broadband designs are featured in [18] and [19].

Recently, constantly decreasing size requirements began also to affect the design of directional couplers. Very compact designs that can be even integrated inside a package have been reported in [20] and [21]. The design from [21] is presented in Fig. 3.14, while [20], presented in Fig. 3.15, uses an interesting approach of layering three layers of ceramic and one layer of quartz all suspended between the ground planes. Note that using multiple layers represents also a method of balancing the propagation velocities between the even and odd modes of operation, leading to an increased directivity.
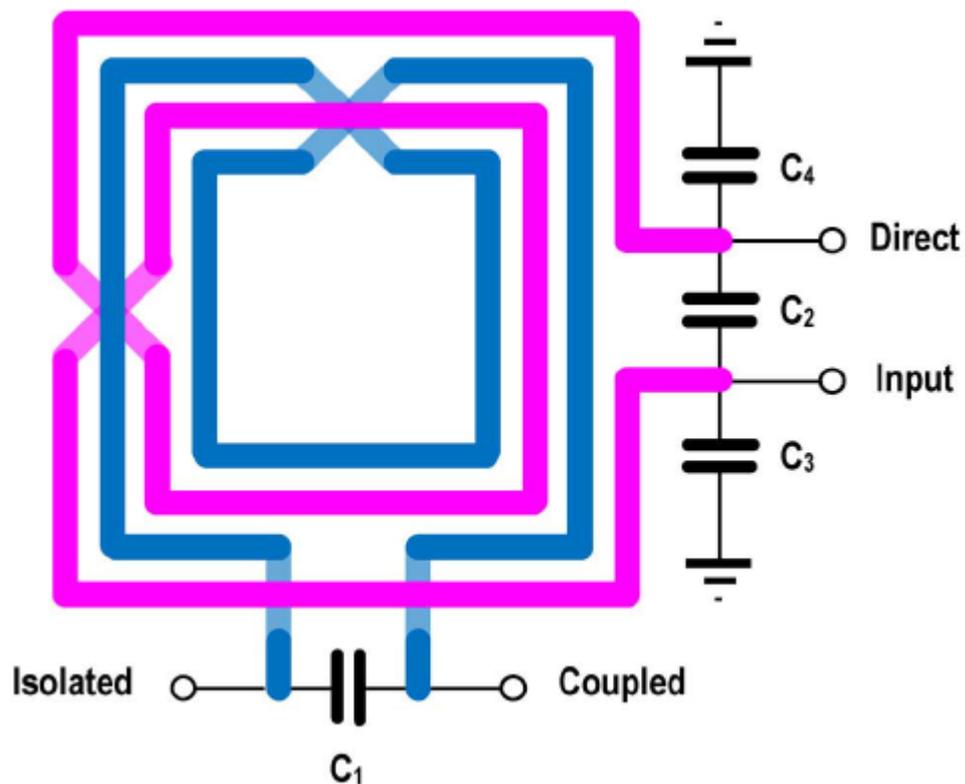
Fig. 3.14 - Compact spiral directional coupler presented in [21].
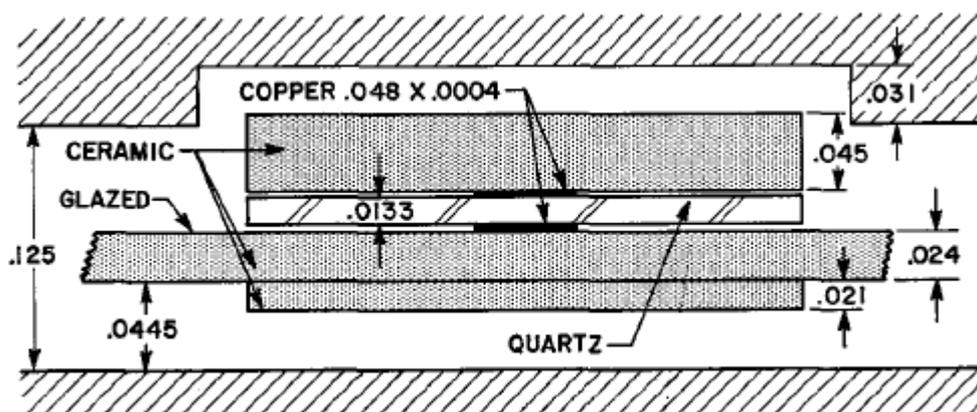
Fig. 3.15 - Three layered directional coupler presented in [20].

43

Tuneable designs of directional couplers were also published, for the applications where the coupling must change during the process. Good examples of this kind are [13] and [22]. The design from [22] is represented graphically in Fig. 3.16.
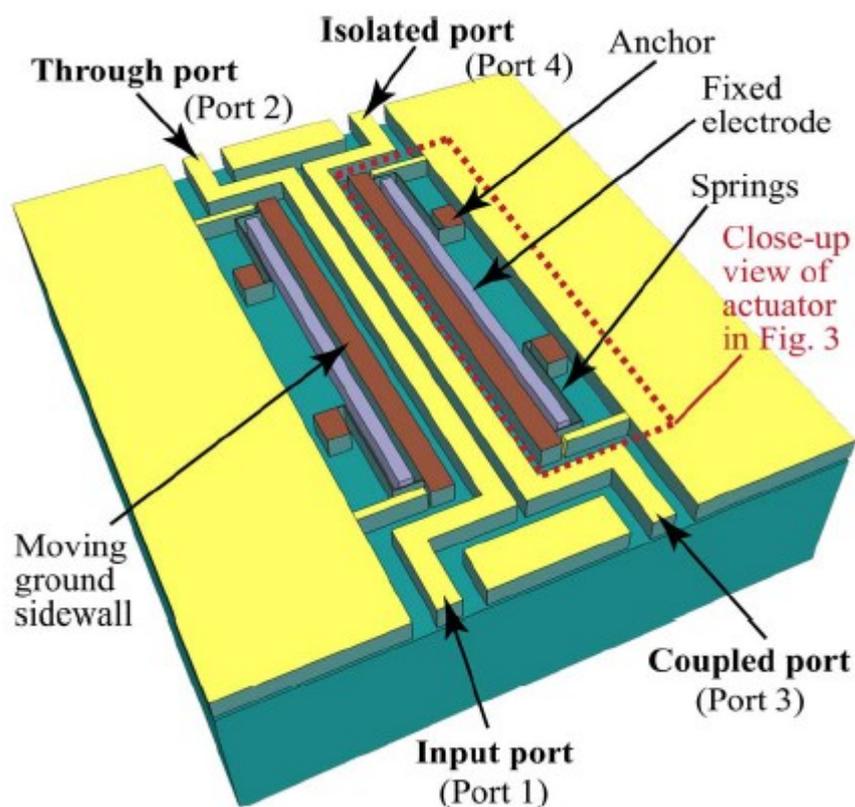
Fig. 3.16 - Tuneable directional coupler made by using a MEMS spring.

Finally, in the case when couplers made with microstrip lines are not desired, it is possible to choose a lumped element directional coupler, a good example of this being presented in [23].

An important observation is that some of the above described directional couplers have a large coupling factor ([18] [20]), their use being recommended for power splitting applications. In the application that will be illustrated in this work, a low coupling factor is desirable, as the mismatch detection circuit should impact as little as possible the functionality of the power transistor.
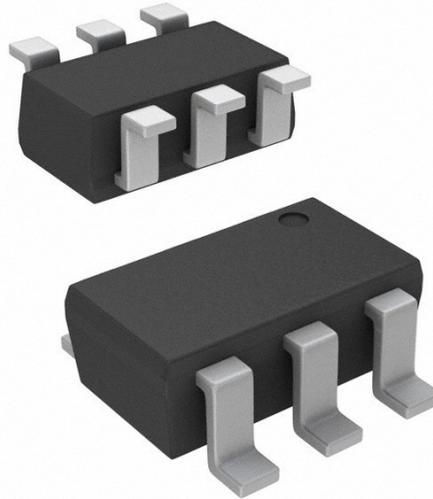
Fig. 3.17 - IC directional coupler with a very compact SOT package.

Fig. 3.18 - External directional coupler able to handle large input powers while providing high directivity.

Commercial directional couplers exist in a wide range of possible choices, depending on the application for which they are required. Small IC SMD directional couplers can be found, like the one presented in Fig. 3.17, but mostly they are able to accept only a low amount of power at the input (below 30 dBm). Also the coupling factor is usually large in this case (the Skyworks DC08-73LF having 16 dB of coupling).

Directional couplers for larger powers also exist, like the one in Fig. 3.18. This kind of devices (in particular the Agilent 775D illustrated above) can handle input powers up to 50 dBm, with a coupling of 20 dB and a directivity of 45 dB for the presented case. However, it can be seen that its large size is an inconvenient for small, portable applications. Also, integrating a large power directional coupler inside end user applications such as microwave ovens is not effective, as it increases significantly the production cost for the device. At the end of this section, it is interesting to provide a comparison between some of the designs that were illustrated and analysed. Performance in terms of the most important parameters, especially coupling factor and directivity is presented for several directional couplers in Table 3.1

Table 3.1 - Performance characteristics for selected directional couplers presented in Section 3.2.

Directional coupler	Coupling factor	Directivity	Considerations
Design reported in [18]	-3 dB	25 dB	Coupled line coupler, length of λ/3 at 4 GHz
Design reported in [20]	-3 dB	36 dB	Coupled line coupler, λ/4 long coupled segments
Design reported in [21]	-10dB	35dB	IPD integration process, compact 2.5 mm^2 total area
Design reported in [23]	-3 dB	>10 dB	Lumped elements implementation
Skyworks DC08-73LF	-16 dB	22 dB	Integrated directional coupler, low input power, low bandwidth (0.1 GHz)
Agilent 775D	-20 dB	45 dB	Large external directional coupler

From Table 3.1 it can be seen that very good results in terms of coupling factor and directivity can be obtained using external couplers. Contactless directional couplers made with coupled lines can also achieve good performance, but their size is large (usually quarter lambda, as presented in section 3.2), and also frequency dependent. This makes them not suitable for in-package integration.

Therefore, the idea of being able to integrate a mismatch detection circuit inside the package of a power transistor is clearly an attractive one. It would provide the power transistors with additional information, such that the dangerous operating conditions can be detected. This means a safer and potentially longer operation time for the device as a whole.

3.4   Bondwire coupler design

As it was presented in Chapter 2, in order to make use of a directional coupler to measure the reflection coefficient, this device should meet certain requirements, among which the most important ones are its directivity and its coupling factor. It is desirable that the coupler has a low enough coupling factor such that most of the power delivered by the power amplifier is reaching the output load, without being wasted by coupling it. Also, considering the limited area available inside the package, it would be difficult to fit down-converting mixers in order to

be able to use both the magnitude and the phase of the coupled waves. This is why a magnitude only measurement of the reflection coefficient is preferable. As presented in Chapter 2, magnitude only measurements rely on a good directivity of the directional coupler, which becomes then also an important requirement. However, the directivity and coupling are strongly influenced by the size and positioning of the directional coupler inside the package. Therefore, even if some ideal dimensions are determined in order to obtain the desired values, area limitations may force to settle for a lower accuracy implementation.

The idea of implementing the directional coupler presented in this work comes from making the most out of the already existing elements inside the package. It is known that the power transistor dies are connected to the outside package lead by means of bondwires. A photo representing this implementation is presented in Fig. 3.19.
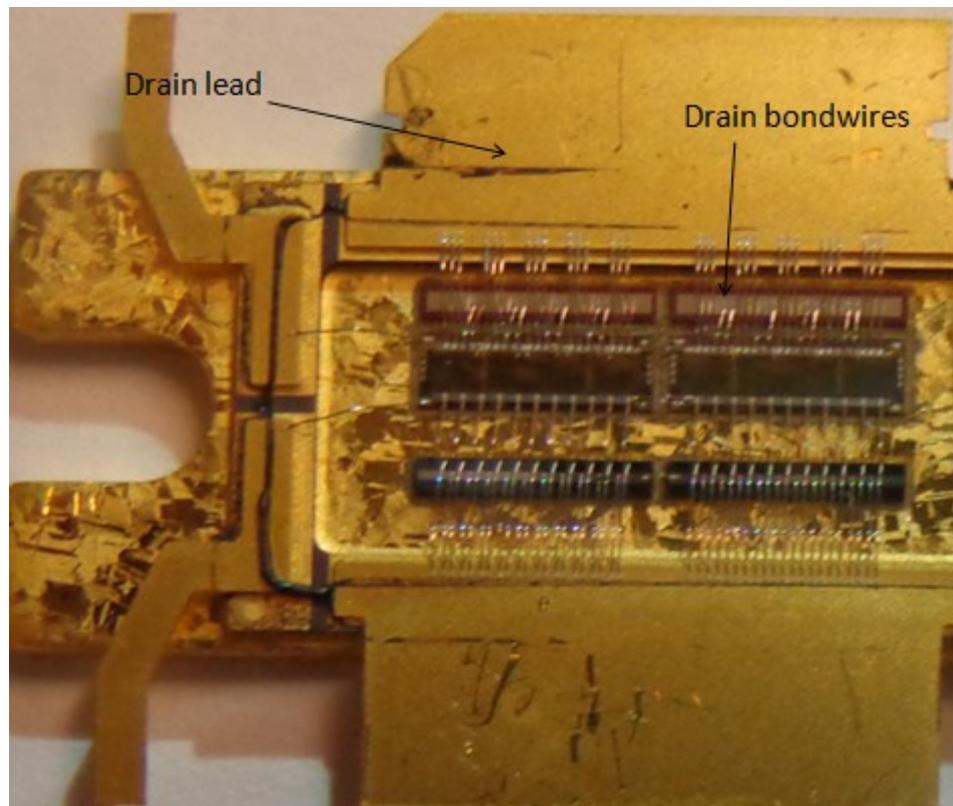
Fig. 3.19 - De-capped power transistor presenting the array of bondwires connecting the drain of the power bar to the package's drain lead.

The length, shape and height of the bondwires forming the bondwire array depend very much on the class in which the power transistor is designed to operate. As nowadays the bondwires are widely used to make also part of the output matching network, their length will define in an important way the inductance of this output matching network.

Power flowing through the bondwires towards the drain lead can be coupled to an additional microstrip line, or extra bondwire, placed close to the array. In this way, a directional coupler can be designed in package, by only using a coupled element placed in parallel with the

bondwires. These implementations use a minimum amount of area and no extra ICs are needed to couple the power.

Since the target of this project are high power transistors, powers in the order of 35 dBm or higher are expected to flow through the bondwire array. In order to allow a fraction as large as possible of this power to get into the load, the power coupled by the directional coupler has to be low. As mentioned earlier in this chapter, designing for any coupling level is not really possible in area limited environments. Therefore, trade-offs have to be made with respect to the coupling level, as well as with the directivity. Also, the proposed implementation will represent a non uniform coupler, a structure in which it is more difficult to design for a desired coupling factor and directivity than in the case of parallel, uniform couplers. For investigating the design space of possible bondwire based directional couplers, different analyses about the values that can be obtained in the sense of coupling and directivity are presented in the next sections of this chapter. The influence of factors such as the length of the bondwires and the distance where the coupled element is placed with respect to coupling factor and directivity is investigated, by performing simulations with different structures. As it will be seen in the rest of the following sections, the obtained results approach the trends illustrated in the theoretical investigation of the directional coupler shown in section 3.2, especially in the case of the coupling factor. The non uniform coupling mechanism can lead to directivity behaviours more difficult to predict than in the basic, uniform coupling cases. While a general idea about its variation can be made by analyzing the plots, the obtained directivity results were less matched to the ideal theoretical values than the obtained coupling factor. This is why in designs that require a higher, or less varying directivity, special compensation methods need to be applied to the design in order to improve its performance. These directivity enhancing techniques were not analyzed in this work, and represent at this point an important future step of this project.

The simplest situation of two parallel bondwires coupled to each other is depicted in Fig. 3.20.
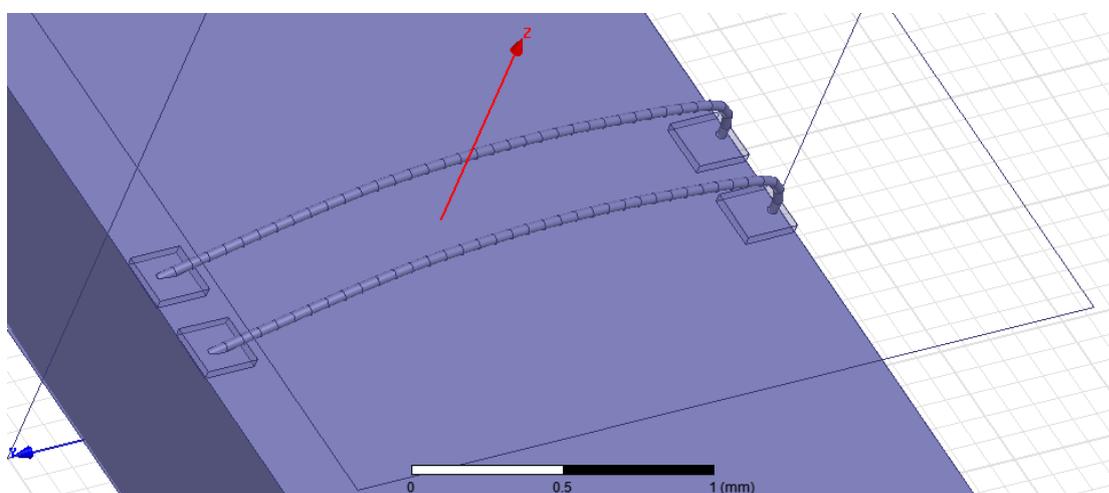
Fig. 3.20 - Ansys HFSS schematic representing a pair of coupled bondwires.

When RF power is applied at one side of the first bondwire, it will flow along it to the other end. Because of the coupling effect, a certain fraction of this power will get coupled also on the second bondwire. As it was mentioned before, this application will make use of the bondwire array connecting the drain of the power transistor's bar to the drain lead of the package. Therefore, a more realistic approach to the investigated problem would be to study not the coupling from one bondwire to another, but the coupling from a bondwire array to an additional coupled element. A very useful software for 3D EM simulations is Ansys HFSS. This software gives the user the possibility to create his own 3D circuit elements and simulate their effect. In particular for the analysed application, bondwires can be individually drawn and placed in any possible configuration by varying their parameters. A bondwire array consisting of seven parallel bondwires has been initially drawn. This number of parallel bondwires is varying in practice from application to application, depending on the requirements for the output matching network of the power transistor. The bondwires in this initial array have a length of 2.5 mm, and a maximum height of 0.7 mm over the ground plane. Their thickness is 25 μm. The substrate chosen for the simulations is a Rogers 3006 substrate, having the characteristics presented in Table 3.2.

Table 3.2 - Characteristics of the Rogers 3006 substrate.

Dielectric Constant	6.5
Dissipation Factor	0.002
Thermal Conductivity	0.79
Substrate Thickness	0.254 mm

Considering that the substrate on which the bondwires are placed is maintained constant during all the design process, the only parameters that can be changed in the above configuration are the length of the bondwires, their height over the ground plane and their relative position with respect to each other. Also, considering the design of the bondwire based directional coupler, there are additional design parameters that are influencing the overall coupler's performance, such as the type of the coupled element, or the distance between the coupled element and the bondwire array. Altogether, these parameters are affecting the electrical properties of the directional coupler in a certain way.

As a first test, an extra bondwire was placed next to the above described bondwire array. This implementation is shown in Fig. 3.21.
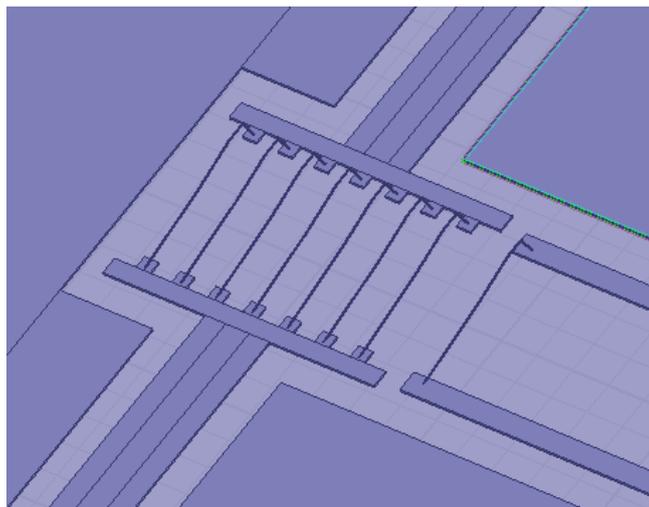
Fig. 3.21 - A coupled extra bondwire placed next to the bondwire array (Ansys HFSS schematic).

It is understandable that a very large number of possible layout options can be implemented, even in this simple example, in order to investigate the impact on the coupling factor and the directivity. However, due to the limited time available in this project, some starting restrictions were made in the layout process. The most important design decision that will be considered in all the following analysed examples is the distance between the bondwire array and the coupled element, which is represented by the extra bondwire in Fig. 3.21. This spacing has been fixed to 0.2 mm for all the following investigated cases, which represents the minimum microstrip spacing in the used PCB manufacturing process. The reasons for making this choice are both practical and application related. First of all, placing the coupled element close to the bondwire array does increase the coupling between the two of them, but however the coupling factor will still have a relatively low value, lower than -20 dB. In these cases of loosed coupling, the signal coupled into the extra bondwire will be close to the noise level present due to parasitic coupling. Therefore, increasing the coupling will lead to a better ratio between the signal level and the noise level at the coupled ports. In later implementations of this directional coupler, as it will be seen, the coupled element can be placed even underneath the bondwire array, in order to reduce the influence of noise to a minimum. Secondly, since the bondwire based directional coupler was in the end used only as the starting point for the integrated six port reflectometer described in Chapter 4, designing the best possible directional coupler in terms of coupling and directivity was not the objective of this work. It is therefore possible that by adjusting all the above mentioned design parameters in a different way, a better directivity than the ones reported in the next analysis is obtained, for example.

In this initial configuration, the presented coupler has a coupling factor of -20 dB and a directivity of 9.7 dB. By sweeping the length of the bondwires in the above figure between 1.2 mm and 6.2 mm, the impact on the coupling factor and directivity can be seen from Fig 3.22.
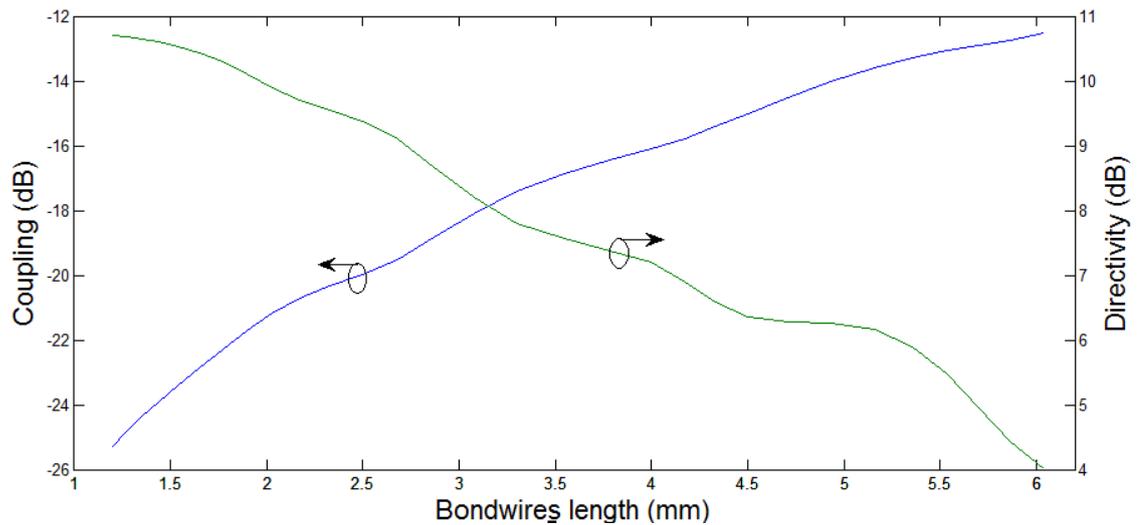
Fig. 3.22 - Coupling factor and directivity versus the swept length of bondwires in the bondwire array. The analysed layout is the one having an extra bondwire placed next to the bondwire array.

This plot shows that the coupling factor increases with the increase in the length of the bondwires, which was expected in the case of short coupled sections, as presented in section 3.2. However, the obtained directivity of below 10 dB (at 2.5 mm bondwire length) can be considered small compared to regular commercially available directional couplers. This is why other ways of creating the layout were also investigated.

Another possible way of implementing the directional coupler is by using a piece of microstrip transmission line coupled to the bondwire array. After doing this, the ends of the microstrip transmission line can be used as the coupled and isolated ports of the directional coupler. Note that this implementation will lead to a non uniform coupling mechanism, and also non homogenous conditions for the coupled section, because of the separation between the dielectric and air mediums. To couple power from the bondwire array into the microstrip line, this one has to be placed close to the array. As it is expected, depending on the distance from the array, more or less power will be coupled by the directional coupler. This is a useful property because at a later stage the distance at which this microstrip line is placed can be arranged such that the desired coupling factor is achieved. For the same reasons stated in the case of the extra bondwire directional coupler, the microstrip line was placed at a distance of 0.2 mm away from the bondwire array. This distance was not modified during any of the simulations that will be presented in the next paragraphs, and therefore its influence is not taken into consideration at this point. An HFSS schematic of this proposed implementation is presented in Fig. 3.23.

Regarding the directional coupler design, there is also another type of approach that can be taken. Because the bondwires connecting the drain of the transistor's power bar to the package outside lead have a certain height, it is also possible to place the coupled transmission line exactly underneath the bondwire array. This way of implementing has two quickly

51

observed advantages: a) there is no need for extra area outside the bondwire array to place the coupled line, and b) because the line is placed underneath the array, almost all of the coupled power will come from the bondwires, and so the coupling will be less influenced by parasitics, which can have a significant impact in package. For a better understanding of this proposed topology, an HFSS schematic representing the design is presented in Fig. 3.24.
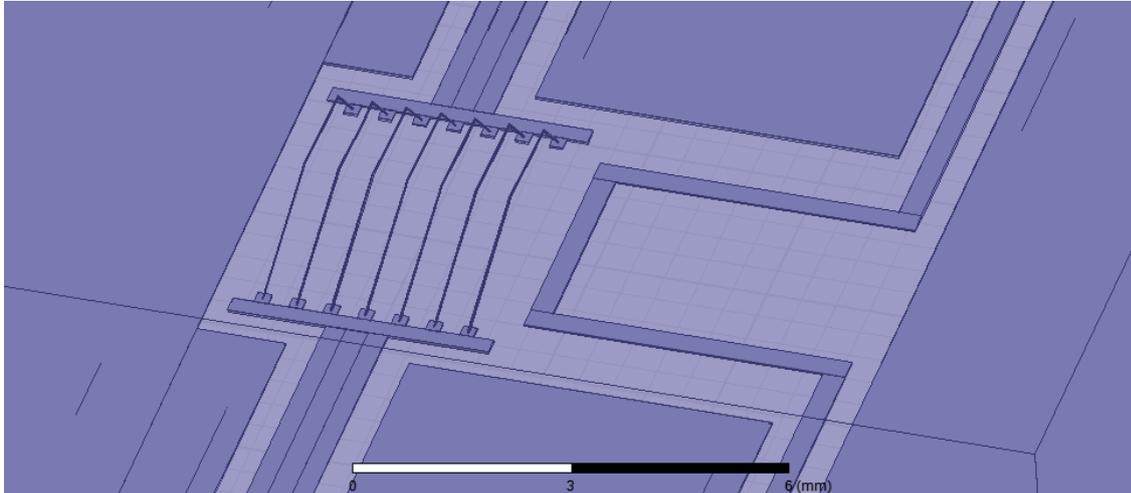
Fig. 3.23 - Directional coupled made by placing a coupled microstrip line next to a bondwire array.
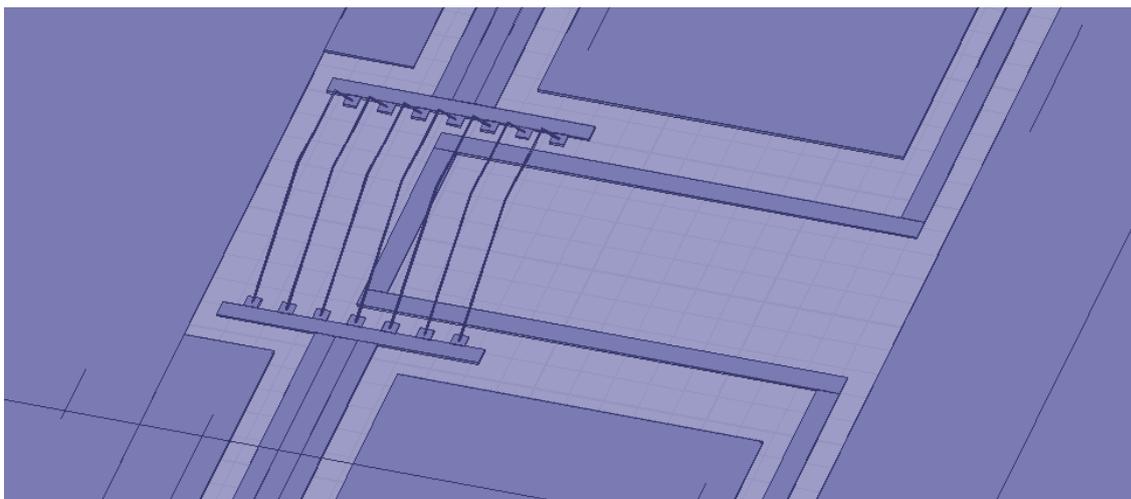
Fig. 3.24 - Directional coupler made by placing a coupled microstrip line underneath the bondwire array.

Once these two possible implementations have been proposed, the same test of sweeping the length of the bondwires in the bondwire array can be performed. The coupler's performance with respect to the bondwire length for the two investigated implementations is shown in Figs. 3.25 and 3.26.
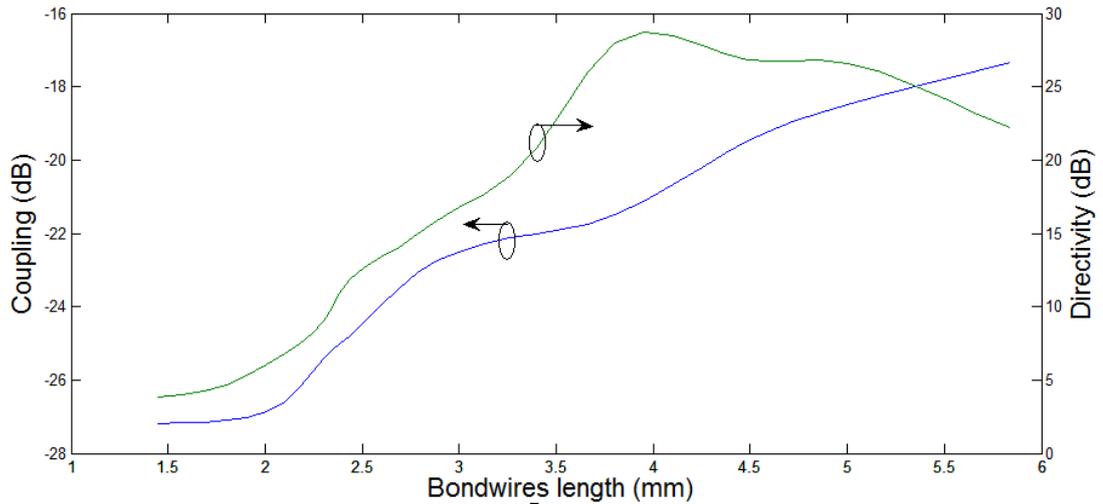
Fig. 3.25 - Coupling factor and directivity versus the swept length of bondwires in the bondwire array. The analysed layout is the one having a coupled microstrip line placed underneath the bondwire array.
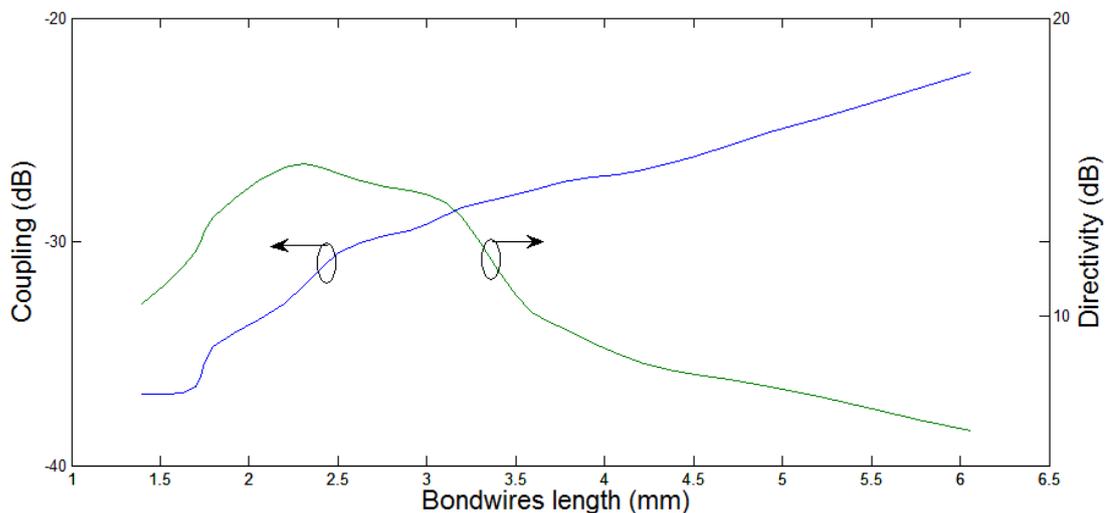
Fig. 3.26 - Coupling factor and directivity versus the swept length of bondwires in the bondwire array. The analysed layout is the one having a coupled microstrip line placed next to the bondwire array.

It can be observed the coupling factor increases again with the increase in the length of the bondwires, which is understandable according to the theory. The simulated directivity had a varying behaviour, due to the non homogenous nature of the designed coupler.

Also, what is important to observe is that both these two implementations perform in simulation significantly better that the one using an extra bondwire to create the coupler, under the specified conditions. The directivity of the designs with the microstrip line placed underneath the array and next to the array is in both cases larger. Also, the coupling factors are a lot smaller, especially in the case of the line placed to the side. Even if the coupling signal is desired to be larger than the noise level, the goal was to design a coupler that does not influence the performance of the main power transistor. Therefore, a looser coupling factor is still desirable.

53

For further confirming the obtained results, another simulator, ADS Momentum was used to design and simulate the layout with the coupled line placed near the bondwire array. The only difference is that in Momentum it is not possible to draw exactly the shape of the bondwires used in the bondwire array. This is why they were designed as perfectly parallel lines placed at a certain height over the ground plane, as presented in Fig. 3.27.
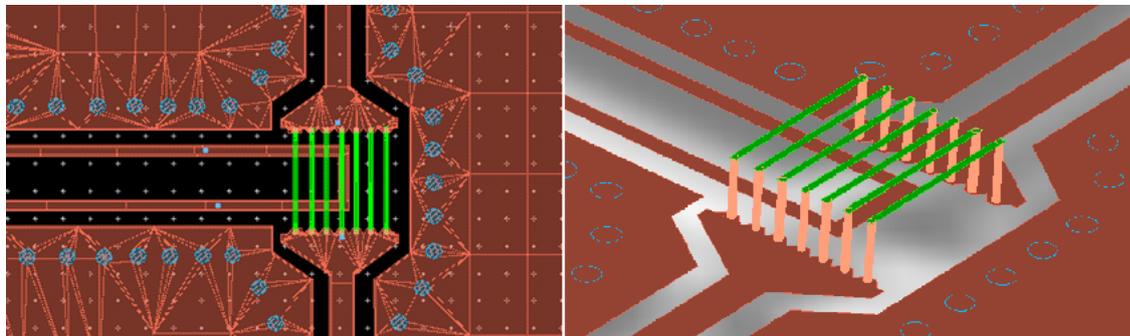
Fig. 3.27 - ADS Momentum layout for a coupled microstrip line placed underneath the bondwire array. Top view (left), and 3D view (right).

The results for the ADS Momentum measurements are presented in Fig. 3.28.
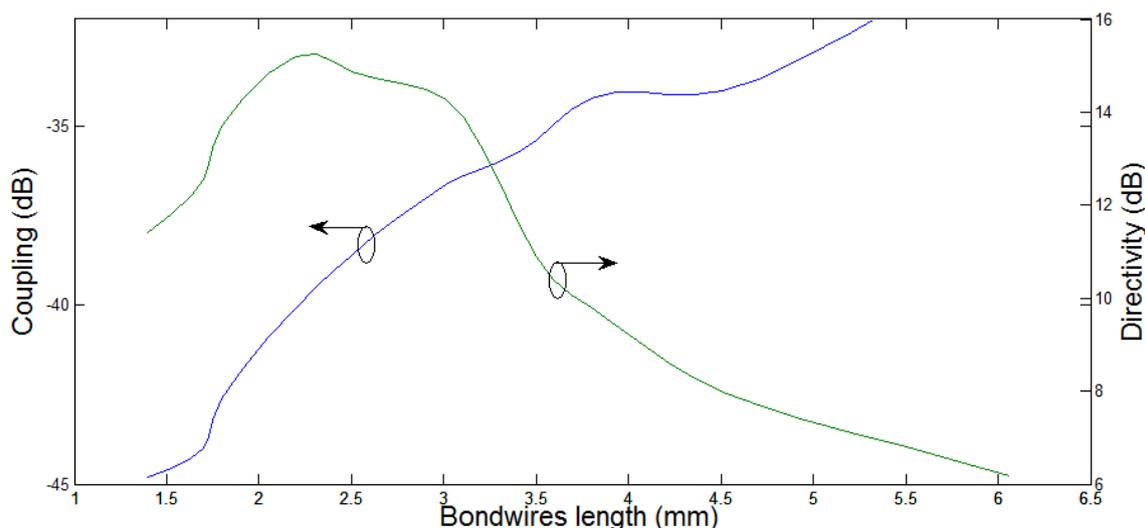
Fig. 3.28 - Coupling factor and directivity versus the swept length of bondwires in the bondwire array. The analysed layout is the one having a coupled microstrip line placed underneath the bondwire array. The simulator used was Agilent ADS.

It can be seen that the two simulators have similar result trends with respect to the directivity and the coupling factor, but slighty different in the returned numerical values. This is explainable, considering the fact that HFSS takes also into consideration the shape of the bondwire. Therefore, the bondwire will not be all the time at the same distance above the ground plane, as it was designed and simulated in ADS Momentum. Considering this, it is expected that the coupling factor returned by this simulator is different than the one obtained using ADS Momentum, which can also be seen in Fig. 3.29 which presents together the results of these two simulators.
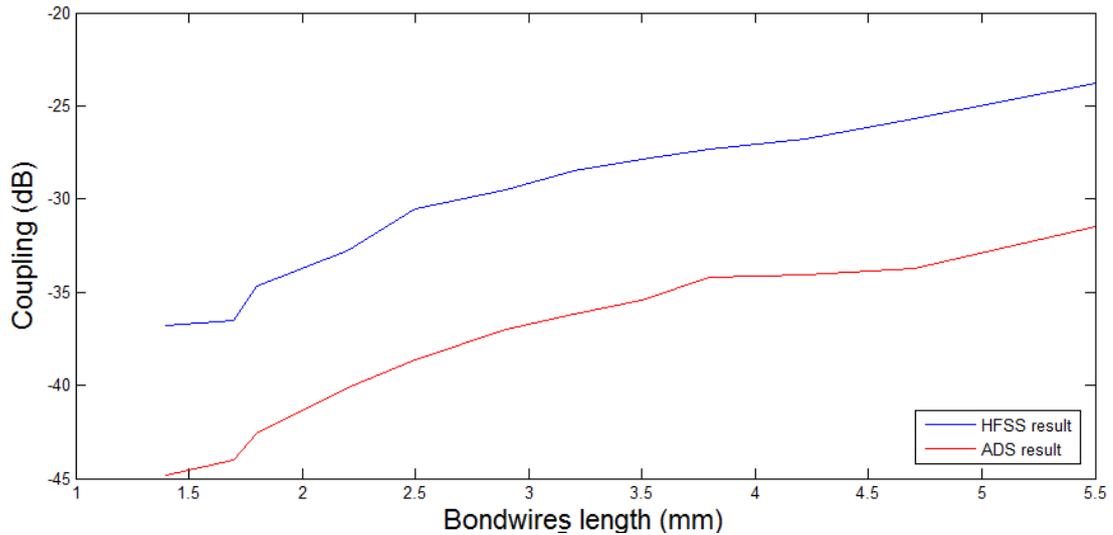
Fig. 3.29 - Comparison between results given by Ansys HFSS and Agilent ADS considering the coupling factor of two similar layouts.

In conclusion, it can be said the results given by Ansys HFSS should be more reliable as they take into consideration all the parameters of the designed directional coupler in a tri-dimensional manner, modelling better the proposed non-uniform coupler. This is why they were used as a reference for the measured results that will be presented in Chapter 7.

Even though a lot of possible design choices can be made regarding the bondwire based directional coupler, in practice this complete design liberty does not exist, as all the used parameters (coupler area, bondwire length, bondwire height) are limited by technical constraints. The next section of this chapter will analyse these constraints and try to illustrate the advantages and disadvantages of the analysed design choices.

3.5   Practical implementation constraints

The previous section started a more practical approach towards the design of directional couplers. Three possible ways of implementing a practical bondwire based directional coupler were investigated: an extra bondwire coupled to a bondwire array, a microstrip line placed underneath the bondwire array, and a microstrip line placed next to the bondwire array. In order to see the impact on the electrical properties, the length of the bondwires in the bondwire array was swept, while keeping all the other design parameters (such as bondwire height, bondwire spacing, spacing between the bondwire array and the coupled element, etc.) to a fixed value.

The conclusion of this simulated sweep was that the directivity is influenced differently by the three different proposed implementations. Regarding the coupling factor, its variation is closer to the expected one, as it increases with the increase in the bondwires length. However, it is interesting to observe that the three different topologies of analysed directional couplers also show different values for the coupling coefficient. The extra bondwire placed in

parallel with the bondwire array couples the most power from the array, especially because it is placed the closest, and at the same level with the main bondwires. Its simulated coupling factor for a 2.5 mm bondwire array is close to -20 dB. The microstrip line placed underneath the array ranks second with respect to the coupling factor. This can be explained by the fact that power couples from all the bondwires in the array, resulting a bigger overall coupled power. Finally, placing the microstrip line next to the array results in the lowest coupling factor, a little over -30 dB for a 2.5 mm bondwire array. This can be explained by the fact that power gets coupled mostly from the bondwire closest to the coupled line, the others having a lower influence, and therefore coupling less power.

This work mostly targets power transistors operating in Class E. In this particular regime of operation, the length of the bondwires connecting the drain of the power bar to the drain lead can be quite large, lengths of 5 mm being not unusual. However, when designing this integrated coupler, flexibility in the application type has also to be kept in mind. Therefore, it is desirable to obtain good results also with bondwires of 2 or 3 mm in length, as they are more common in other classes of operation. Having this in mind, a particular bondwire length of 2.5 mm was chosen for the design of the test boards that were later physically produced and measured in order to prove the principle. The results of these measurements are listed in Chapter 7.

Besides the limitation imposed by the length of the bondwires in the bondwire array, two other factors can be considered: the area available inside the package for placing the coupling element, and the influence of parasitics on the coupled power. From both these points of view, placing the coupled microstrip line underneath the bondwire array could be better. First, in this way the coupling element does not require additional area in the package, being placed in a position that is anyway wasted (underneath the already existing bondwires). Second of all, by positioning it there, most of the coupled power is actually coming from the power flowing through the bondwires, and the influence of parasitics is reduced to a minimum. On the other hand, the microstrip line placed next to the bondwire array might peak up internal package parasitics along with the useful power coming from the bondwires.

At this point, it is also good to give a practical target to be achieved by the produced directional coupler, as a range of possible implementations has been analysed and interpreted. From the above described simulations, it seems reasonable to target a directivity larger than 10 dB. Also, a coupling factor lower than -25 dB looks possible to achieve, especially with the implementations involving the coupled microstrip line. Therefore, these numbers were used from this point onwards as the design targets in the compact directional coupler design.

3.6   Comparison between proposed implementations

As it was presented in the previous section of this chapter, multiple possible implementations of the bondwire based directional coupler were investigated in this work. The goal was to inspect the design space of this kind of compact directional couplers, to observe the variation on directivity and coupling factor in the case of different topologies. Three possible implementations were designed as a layout and tested in two different softwares, Ansys HFSS and Agilent ADS Momentum. So far, all the presented results in terms of coupling factor and directivity were obtained by analysing the influence of the bondwires' length, and assuming that all the other design parameters are kept constant.

This section will start from these basic characteristics of the presented couplers (simulated directivity and coupling factor) and will analyse the impact of other factors, such as the distance away from the bondwire array where they are placed, the bondwire height, and the total area occupied by the resulting design.

The first factor that will be further analysed now is the height of the bondwires in the bondwire array. As it is expected, this should theoretically have an influence on the coupling factor. As a starting point, an array of seven bondwires, 2.5 mm long, and having a maximum height of 0.7 mm has been used. This is presented in a graphical way in Fig. 3.30.
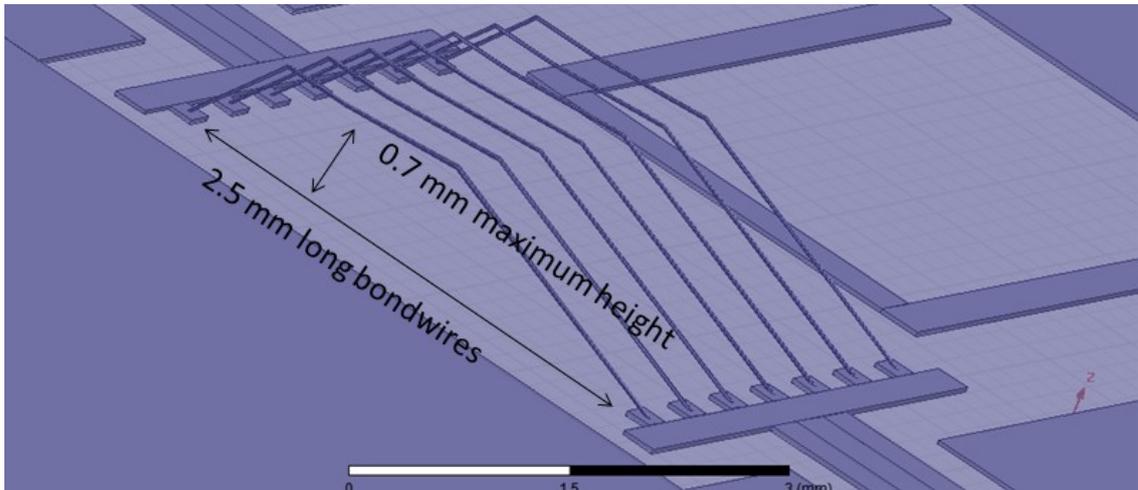
Fig. 3.30 - Representation of the bondwire array showing the length and maximum height of the bondwires.

Considering the implementation with the coupled microstrip line placed underneath the bondwire array, the height of the bondwires has been then swept, while all the other design parameters mentioned above (bondwires' length, spacing between the bondwires) were kept constant. The results in terms of coupling factor and directivity for this implementation are presented in Fig. 3.31.
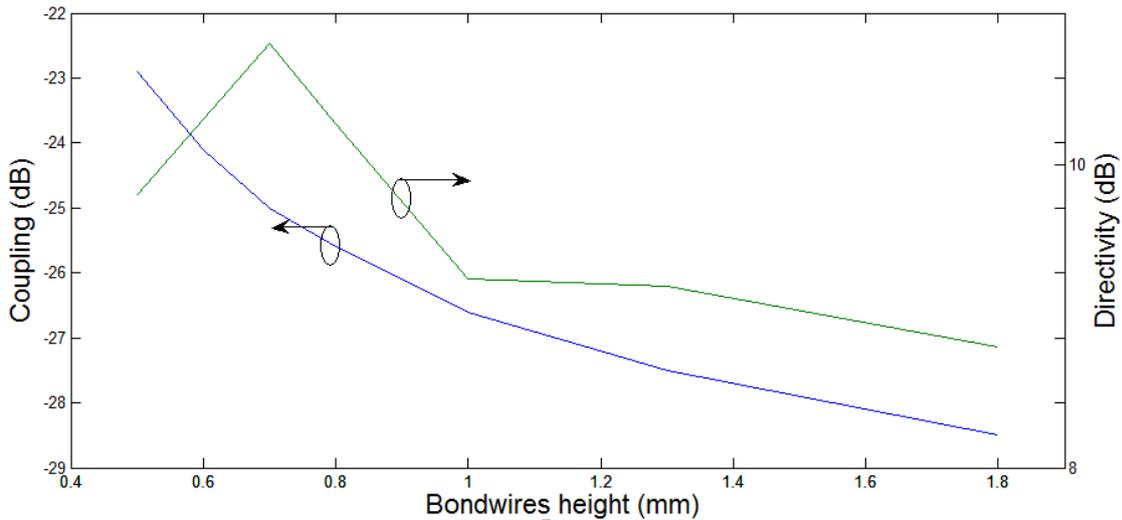
Fig. 3.31 - Impact of changing the bondwires height on the achieved coupling factor and directivity for a design having the coupled line underneath the bondwire array.

It can be seen that the coupling factor decreases as the height is increased to a maximum value of 1.8 mm, keeping all the other parameters at a constant value. Also, if the height is reduced to 0.5 mm, the coupling factor increases by 2 dB. Fig. 3.20 suggests that the coupling factor can be controlled up to some extent by the height of the bondwires in the array. However, the shape and length of the bondwires is usually controlled in order to realize the proper output matching network, and it is possible that the ability to change the height of them in a free way will not be always possible.

The same experiment was performed for the implementation with the microstrip coupled line placed next to the bondwire array. The result in terms of coupling and directivity as a function of the swept bondwire height are presented in Fig. 3.32.
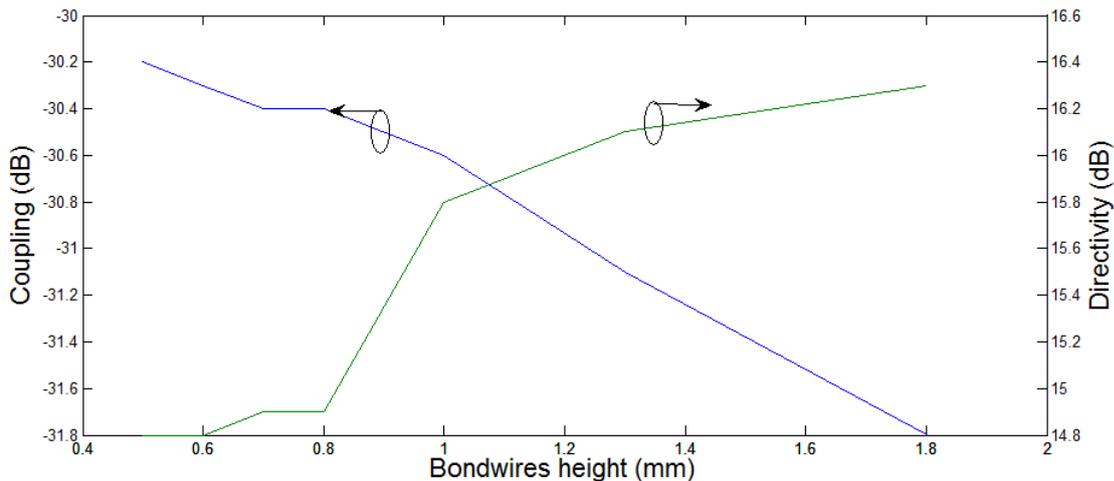
Fig. 3.32 - Impact of changing the bondwires height on the achieved coupling factor and directivity for a design having the coupled line next to the bondwire array.

Another way of reducing the coupling factor for the design having the coupled line outside the bondwire array is to increase the distance at which the line is placed apart from the array, as theoretically suggested in section 3.2. In all the simulations performed so far, this

distance was set to a value of 0.2 mm. The impact on the coupling factor from increasing this distance and keeping all the other parameters constant can be seen by making a sweep. The results are presented in Fig. 3.33.
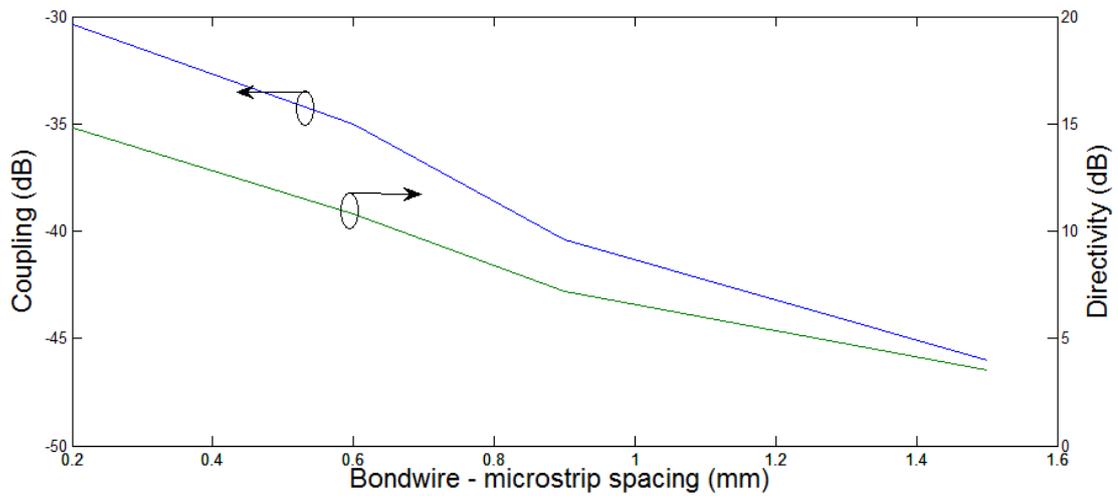
Fig. 3.33 - Impact of changing the bondwire-microstrip line spacing on the achieved coupling factor and directivity for a design having the coupled line next to the bondwire array.

It can be seen that the coupling is further reduced as the microstrip line is placed away from the bondwire array. However, even if in the simulator this result is possible, in reality the impact of parasitics can become larger as the coupled line is moved away from the bondwires. Also, another important limitation of this approach is the total area occupied by the coupling element. By moving the line further away from the bondwire array, more area is needed, which will quickly become a problem considering the strict limitations regarding the available area inside the package.

Considering all the simulations performed during this and the previous section, a couple of results and intermediate conclusions can be drawn. A table of advantages and disadvantages for the implementations with the coupled line placed underneath the array and next to the array is presented in Table 3.3.

Table 3.3 - Advantages and disadvantages for the designs with the coupled line placed underneath the bondwire array and next to the bondwire array. The conclusions are based on simulated results made under the above stated conclusions.

Coupled line underneath the bondwire array		Coupled line next to the bondwire array	
Advantages	Disadvantages	Advantages	Disadvantages
More compact design	Higher coupling	Good directivity	Larger occupied area
Low package parasitics influence		Low coupling	More exposed to parasitics
Medium/Good directivity			

In order to test in practice the designs, prototypes of both these two implementations were produced. The one having the microstrip line placed near the bondwire array has been also tested, and its S parameters were measured. The results obtained after the measurements were matched close to the simulated ones, a directivity of 14 dB and a coupling of -29 dB being reported. The whole set of measured S parameters will be presented in the chapter dedicated to the measurements and later in the Appendix. Also the implementation with the microstrip line placed underneath the bondwire array has been used in practice during the measurements of the compact six port reflectometer design. These results will also be presented in the Chapter 7, and a wider view on the compact six port reflectometer will be given in the next chapter, which is completely dedicated to it.

References

[1] D. M. Pozar, "Microwave Engineering", ch. 7, Wiley, 2012.

[2] E. G. Cristal, "Coupled Transmission Line Directional Couplers With Coupled Lines of Uneven Impedances", G-MTT International Symposyum Digest, 1966.

[3] R. Mongia, I. Bahl, P. Barthia, "RF and Microwave Coupled Line Circuits", Artech House, 1999.

[4] B. Sheleg, B. E. Spielman, "Broadband directional couplers using microstrip with dielectric overlays," IEEE. Transactions on Microwave Theory and Techiques., vol. MTT-22, 1974.

[5] M. Moradian, K. Khalaj, "Improvement of the Characteristics of Microstrip Parallel Coupled Line Coupler by Means of Grooved Substrate", Progress in Electromagnetic Research, vol. 2, 2008.

[6] A. Podell, "A High Directivity Microstrip Coupler Technique", IEEE MTT-S International Microwave Symposium Digest, 1970.

[7] S. L. March, "Phase Velocity Compensation in Paralel Coupled Microstrip", IEEE MTT-S International Microwave Symposium Digest, 1982.

[8] F. Masot, F. Medina, M. Horno, "Theoretical and Experimental Study of Modified Coupled Strip Coupler", Electron. Letters, vol. 28, February 1992.

[9] T. G. Bryant, J. A. Weiss, "Parameters of Microstrip Transmission Lines and of Coupled Pairs of Microstrip Lines", IEEE Transactions on Microwave Theory and Techniques, vol. MTT-16, no. 12, December 1968.

[10] E. G. Cristal, L. Young, "Theory and Tables of Optimum Symmetrical TEM-Mode Coupled Transmission Line Directional Couplers", IEEE Transactions on Microwave Theory and Techniques, vol. MTT-13, no. 5, September 1965.

[11] R. Levy, "Tables for Asymmetric Multi Element Coupled Transmission Line Directional Couplers", IEEE Transactions on Microwave Theory and Techniques, vol. 12, issue 3.

[12] C. B. Sharpe, "An Equivalence Principle for Nonuniform Transmission-Line Directional Couplers", IEEE Transactions on Microwave Theory and Techniques, vol. MTT-15, no. 7, July 1967.

[13] W. P. Ou, "Design Equations for an Interdigitated Directional Coupler", IEEE Transactions on Microwave Theory and Techniques, February 1975.

[14] W. E. Caswell, "The Directional Coupler", IEEE Transactions on Microwave Theory and Techniques, February 1966.

[15] V. Tas, A. Atalar, "Using Phase Relations in Microstrip Directional Couplers to Achieve High Directivity", IEEE Transactions on Microwave Theory and Techniques, vol. 61, no. 12, December 2013.

[16] A. Pourzadi, A. R. Attari, M S. Majedi, "Directivity-Enhanced Directional Coupler Using Epsilon Negative Transmission Line, IEEE Transactions on Microwave Theory and Techniques, vol. 60, no. 11, November 2012.

[17] S. Lee, Y. Lee, "A Design Method for Microstrip Directional Couplers Loaded With Shunt Inductors for Directivity Enhancement, IEEE Transactions on Microwave Theory and Techniques, vol. 58, no. 4, April 2010.

[18] C. Caloz, A. Sanada, T. Itoh, "A Novel Composite Right-/Left-Handed
Coupled-Line Directional Coupler With Arbitrary Coupling Level and Broad Bandwidth", IEEE Transactions on Microwave Theory and Techniques, vol. 52, no. 3, March 2004.

[19] A. M. Abbosh, M. E. Bialkowski, "Design of Compact Directional Couplers for UWB Applications", IEEE Transactions on Microwave Theory and Techniques, vol. 55, no. 2, February 2007.

[20] J. E. Morris, A 3-dB Directional Coupler for Microwave Integrated Circuits", IEEE Transactions on Microwave Theory and Techniques, July 1968.

[21] S. Shim, S. Hong, "A CMOS Power Amplifier With Integrated-Passive-Device Spiral-Shaped Directional Coupler for Mobile UHF RFID Reader", IEEE Transactions on Microwave Theory and Techniques, vol. 59, no. 11, November 2011.

[22] U. Shah, M. Sterner, J. Oberhammer, "High-Directivity MEMS-Tunable Directional Couplers for 10–18-GHz Broadband Applications", IEEE Transactions on Microwave Theory and Techniques, vol. 61, no. 9, September 2013.

[23] R. W. Vogel, "Analysis and Design of Lumped- and Lumped-
Distributed-Element Directional Couplers for MIC and MMIC Applications", IEEE Transactions on Microwave Theory and Techniques, vol. 49, no. 2, February 1992.

4. Compact six port reflectometer

4.1 Introduction

The use of compact directional couplers as a way of coupling the forward and reflected waves has been described and analyzed in the previous chapter. Due to their implementation easiness and the straight forward measurement capabilities, when combined with down converting mixers and low IF (vector) detection, this approach has been for a long time the preferred way of measuring device mismatch / load reflection coefficients. However, as it was more clearly underlined in the dedicated chapter, it has significant disadvantages in terms of complexity, size and costs, yielding the idea of using a different measurement approach for this specific application.

In the aimed approach, both phase and amplitude of the coupled waves are measured in order to determine the complex reflection coefficient at the output port. To avoid the complexity of the down-converting mixer approach, a modified six-port reflectometer method is followed which can provide an elegant way of detecting Γ_L while still permitting a very compact design. As it makes use only of the magnitudes of the coupled waves, it eliminates the need to use mixers in order to obtain the phase. Also, even though a large directivity is still desirable (especially in certain design implementations), the demands are now more relaxed, as a non-perfect directivity can still be corrected by applying a calibration step.

4.2 Six port theory

The six port reflectometer has been analysed and developed continuously since it was introduced almost 50 years ago. It evolved from only a theoretical way of measuring the mismatch into one of the most compact and reliable devices that can be used as low complexity network analyser. Considering the fact that its basic functionalityis more complex than the basic directional coupler design alone, a good amount of attention has to be used both in physically designing the layout, as well as in the algorithms used to manipulate the obtained data. This section will focus on the theoretical background behind the functionality of the six port reflectometer. Section 4.3 of this chapter will offer a view on the way in which the six port reflectometer was developed in time, together with an inspection of some remarkable published designs.

The theory behind the six port reflectometer has a similar starting point as the directional coupler. The waves travelling between two ports (input port and output port) are coupled to (multiple) detection points in order to obtain information about the mismatch present

at the output port. While in the directional coupler the coupled waves are sampled at two positions, in the case of the six port reflectometer four sampling points are required to get all the necessary data. In this way, by measuring four magnitudes it is possible to determine the value of the complex reflection coefficient at the output port. The way in which the method works, can be illustrated starting from the schematic drawing of the six port reflectometer presented in Fig. 4.1. This six port reflectometer assumes a contactless way of coupling the waves flowing between the input and the output port. This approach is very similar to the one that will be later used in the implementation proposed in this work.

Port 1   Port 2

b1   a2

E   LOAD

a1   Coupling structure   b2

P3   P4   P5   P6
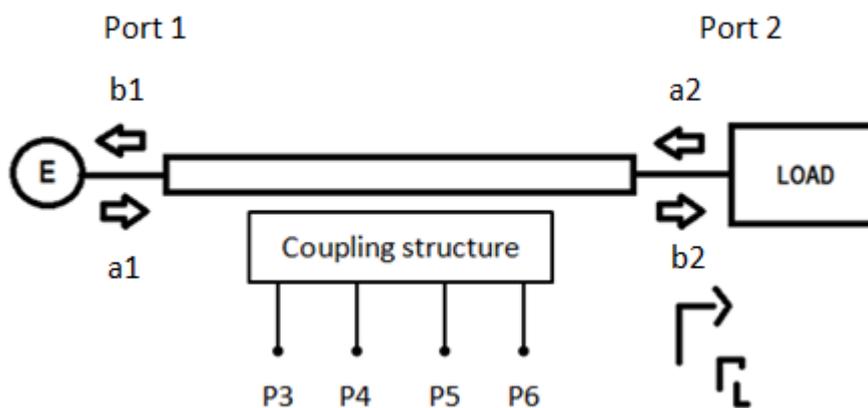
Fig. 4.1 - Diagram representing the basic functionality of a six port reflectometer.

In this drawing, the RF input power gets injected at port 1. Port 2 has a variable impedance, such that the amount of power that gets reflected back from it varies with the loading condition.

The way in which the four collected powers (P_3-P_6) help in finding the exact complex reflection coefficient is illustrated in Fig. 4.2. The method has been described in more detail in [1] and [2], and can be quickly explained as follows.
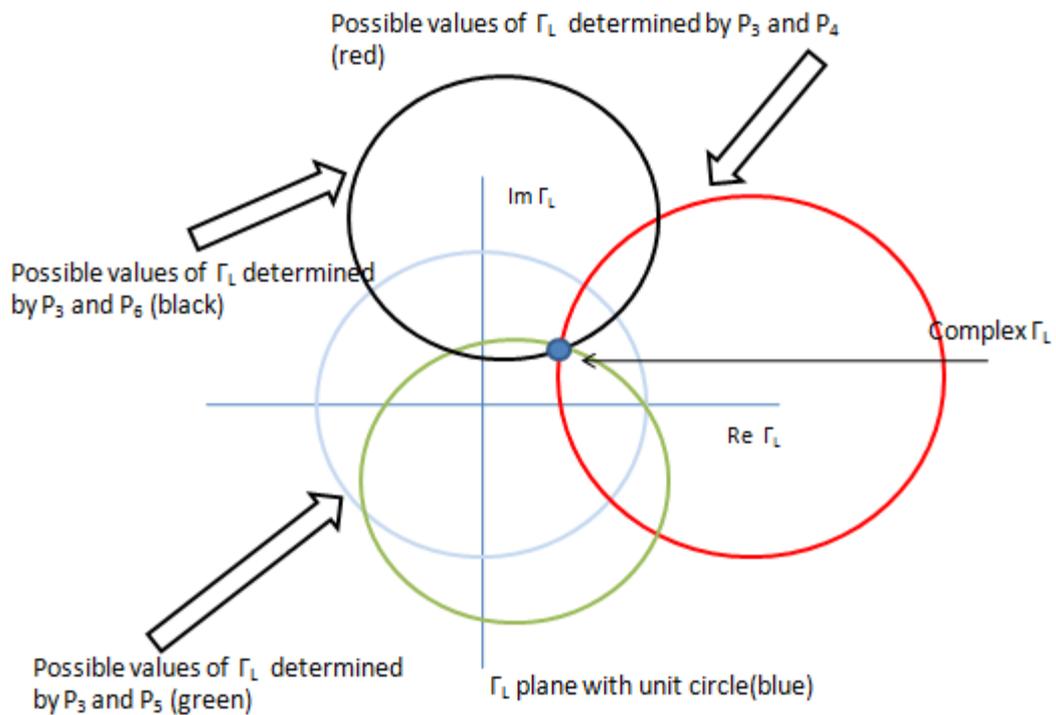
Fig. 4.2 - Calculation of the complex reflection coefficient as the intersection of 3 circular loci, each determined by a pair of power detectors

If any two independent powers can generate a circle of possible Γ_L values, then it means that three of these pairs will generate three circles in the same plane. If the three pairs are chosen by selecting a common voltage in all of them (in this example detector 3) and relating all the other three detectors to the common one, than the obtained circles will ideally intersect in only one point, which is the complex reflection coefficient in the Γ_L plane. In reality, there will be always noise in the readout system, voltage linearization errors, or other errors originating from various reasons. This means that the circles will most likely not intersect in a unique point, but they will create an area within which the correct Γ_L is located. Considering that the correct value of the reflection coefficient is only one point inside this area, it means that the smaller the intersection area, the higher the accuracy with which the reflection coefficient is being determined. This situation is graphically presented in Fig. 4.3.
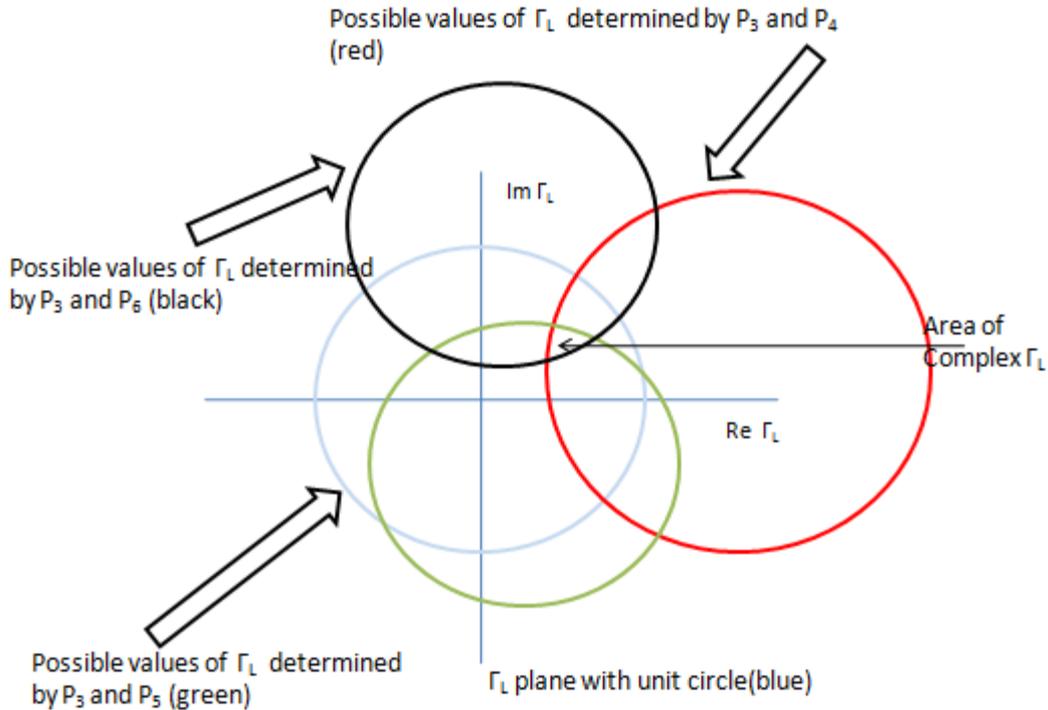
Fig. 4.3 - Error in the calculation of the reflection coefficient caused by noise present in the power detectors.

During the years, extensive analysis on the impact of detector noise on the calculated value of Γ_L have been performed, as it will be later shown. Before starting a deeper mathematical analysis of the six port functionality and the influence of noise in its operation, it is important to observe the distribution of the forward and reflected "a" and "b" waves at the input of each port of the circuit. This is presented in Fig. 4.4.
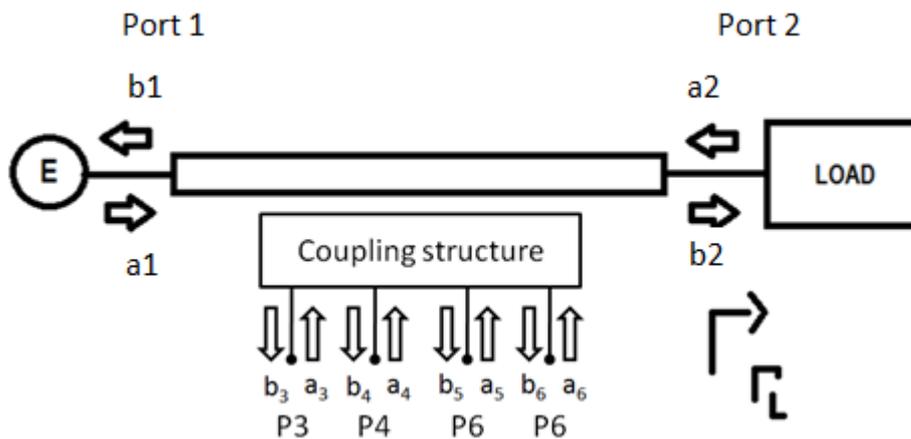
Fig. 4.4 - Schematic presenting the "a" and "b" waves present at the ports of the six port reflectometer.

The four powers detected at the detection ports (P_3-P_6) can be written in terms of the forward and reflected waves as presented in Eq. 4.1 - 4.4.

$$P_3 = |A*a_2 + B*b_2|^2 \qquad (4.1)$$

$$P_4 = |C*a_2 + D*b_2|^2 \qquad (4.2)$$

$$P_5 = |E*a_2 + F*b_2|^2 \qquad (4.3)$$

$$P_6 = |G*a_2 + H*b_2|^2 \qquad (4.4)$$

Rewriting them in a slightly different form puts into light the impact of the above powers on the reflection coefficient, as presented in Eq. 4.5 – 4.8.

$$P_3 = |A|^2|b_2|^2|\Gamma_L\text{-}q_3|^2 \qquad (4.5)$$

$$P_4 = |C|^2|b_2|^2|\Gamma_L\text{-}q_4|^2 \qquad (4.6)$$

$$P_5 = |E|^2|b_2|^2|\Gamma_L\text{-}q_5|^2 \qquad (4.7)$$

$$P_6 = |G|^2|b_2|^2|\Gamma_L\text{-}q_6|^2, \qquad (4.8)$$

with q_3=-B/A, q_4=-D/C, q_5=-F/E, q_6=-H/G.

By observing the above equations, it can be concluded that each pair of power detectors will determine a circular locus of possible Γ_L values. In order to have a relation also with the amount of power injected at port 1 in Fig. 4.4 (forward wave), usually these four obtained powers are used under the form of three ratios. In this sense, port 3 is considered a reference, and the power ratios (or normalized powers) are defined as P_4/P_3, P_5/P_3, and P_6/P_3. Later on, during the whole usage of the six port reflectometer, only these ratios will be taken into consideration and used in the calculation and calibration algorithms.

At this point, the designs describing the six port reflectometers divide in two main parts. Engen [1] proposed a design in which one of the four ports, the reference port, is directly coupled to port 1 of the reflectometer (the port where the input power is injected), and it is not sensitive to port 2 (the port from which the reverse power wave is originating). Considering port 3 as the reference port, Eq. 4.1 can be simplified to

$$P_3 = | B*b_2|^2 \qquad (4.9)$$

Constructing the three power ratios from this new set of power equations leads to Eq. 4.10 – 4.12.

$$\frac{P4}{P3} = \frac{|\Gamma L - q4|^2}{|\frac{B}{C}|^2} \qquad (4.10)$$

$$\frac{P5}{P3} = \frac{|\Gamma L - q5|^2}{|\frac{B}{E}|^2} \qquad (4.11)$$

$$\frac{P6}{P3} = \frac{|\Gamma L - q6|^2}{|\frac{B}{G}|^2} \qquad (4.12)$$

The "q" points in the above equations have a practical geometrical interpretation, as they represent the centres of the three circles that will determine in the end the value of Γ_L, as their intersection. Also, the radius of these circles can be written as presented in Eq. 4.13 – 4.15:

$$R_1 = |\Gamma L - q4| \qquad (4.13)$$

$$R_2 = |\Gamma L - q5| \qquad (4.14)$$

$$R_3 = |\Gamma L - q6| \qquad (4.15)$$

Considering again the representation in Fig. 4.4, Fig. 4.5 shows the influence of the newly introduced parameters (the "q" points and the three radii) on the determination of the complex Γ_L.

Γ_L plane with unit circle(blue)
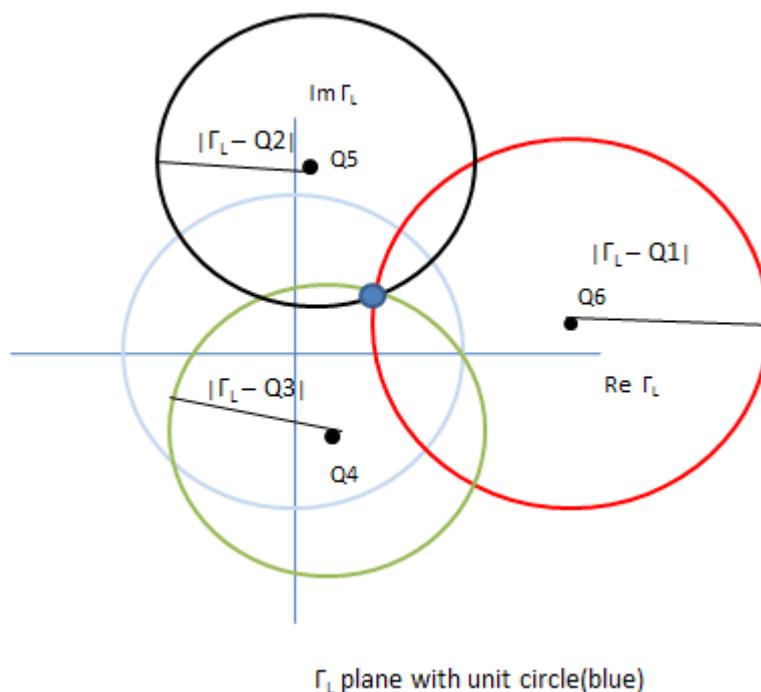
Fig. 4.5 - Geometrical significance of the Eq. 4.10 – 4.15 on the calculation of the complex reflection coefficient.

Now it is easily seen that each pair of power detectors determine a circular locus of possible Γ_L values, in the Γ_L plane, which was earlier described in the beginning of the chapter. The influence of noise in the detectors was also investigated in this situation, and an ample discussion is offered in [1]. Depending on the amount of noise in the detectors, the value of the reflection coefficient will be sensitive to the variations in the three circles radius. The circles' centres do not represent a problem with respect to noise in this implementation, as they are not depending on the power readings. The conclusion drawn in [1] is that in order to have the best noise performance, the three centres need to be placed at equal distance from the origin of the Γ_L plane, and the radial distance between each two of them to be 120˚. In other words, the centres need to be the peeks of an equilateral triangle with the centre in the origin of the Γ_L plane, situation graphically presented in Fig. 4.6.

Γ_L plane with unit circle(blue)
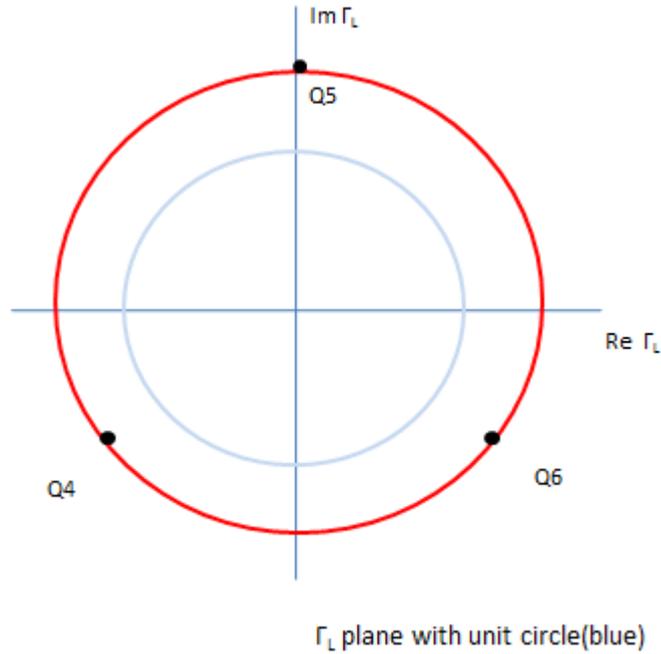
Fig. 4.6 - Ideal placement of the Q points in order to minimize the influence of detector noise in the determined reflection coefficient. This placement takes into consideration a six port design where one of the detectors is used as a reference port.

An even deeper analysis was later performed in [3], the conclusion being that the influence of noise is even further reduced if the centres are placed at a distance between 2 and 3 away from the origin of the Γ_L plane.

However, in practice it is not always possible to have one of the four detectors coupled only to the forward power wave. Another approach to the design of the six port reflectometer is to also make this port sensitive to both forward and reflected waves, such that the power equations describing the ports are the same defined in Eq. 4.1 – 4.4.

Dividing three of these powers to the reference port (for example port 3) leads to the three power ratios that are required for the functionality of the six port reflectometer. These three equations are now.

$$\frac{P4}{P3} = \frac{|\Gamma L - q4|^2}{|\Gamma L - q3|^2} \quad (4.16)$$

$$\frac{P5}{P3} = \frac{|\Gamma L - q5|^2}{|\Gamma L - q3|^2} \quad (4.17)$$

$$\frac{P6}{P3} = \frac{|\Gamma L - q6|^2}{|\Gamma L - q3|^2} \quad (4.18)$$

Still, the Γ_L locus determined by each pair of power detectors is a circle, like in the previous situation. The difference is now that the centre of the circle is not independent of the detected power, and its value can be anywhere on the line connecting a pair of "q" points. This is presented in Fig. 4.7.
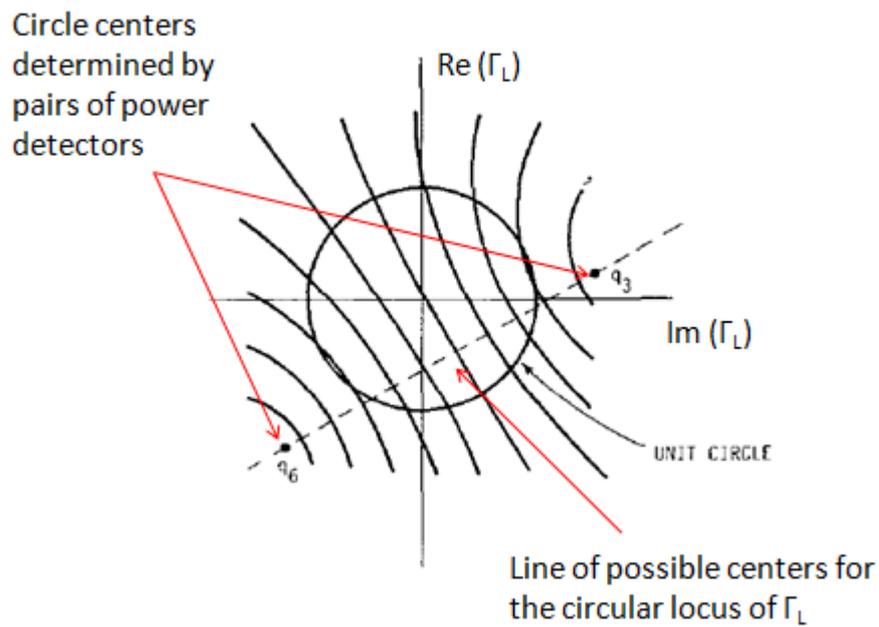
Fig. 4.7 - Position of the centre of the circular locus determined by two power detectors. In the described situation the centre is power dependent and can lie on a line uniting two"q" points.

Analysis on the impact of noise have been performed also for this situation. It was concluded [4] that designing the layout such that the four "q" points have an equal magnitude and are placed equally distant on a circle with the centre in the origin of the Γ_L plane minimizes the influence of the noise at the detector ports. The way in which the four "q" points should be ideally chosen is presented in Fig. 4.8.

Γ_L plane with unit circle(blue)
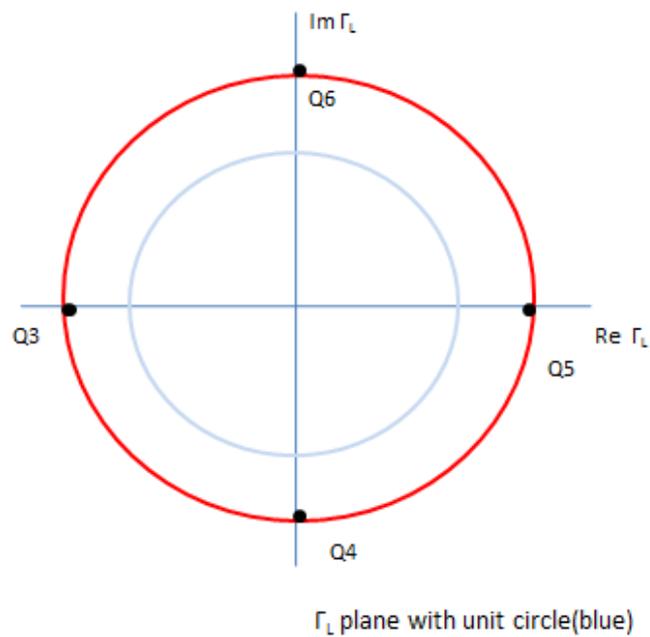
Fig. 4.8 - Ideal placement of the Q points in order to minimize the influence of detector noise in the determined reflection coefficient. This placement takes into consideration a six port design where none of the detectors is used as a reference port.

In this approach, the detector ports are sampling both the forward and reflected waves at exactly 90° shift between each two consecutive detection points. While some designs have no problem in separating the forward and reflected waves (as it will be presented in the next section), in others the directivity of the design will play a very important role and can be a limiting factor. Considering a design that has a medium to high directivity (as it is the situation in this work), special attention has to be given in improving the noise performance, and a new approach in placing the detector points will be developed in Section 4.4 of this chapter.

Once the four voltages are collected, the six port reflectometer requires and initial calibration step in order to be used later in reflection coefficient measurements. There are several known ways of calibrating the six port reflectometer, and some of them will be analysed in the chapter dedicated to the calibration algorithms. The basic requirement that all these algorithms share is that the six port circuit is linear. This means that the powers collected at the detection ports vary in a linear way with the RF power applied at the input, not depending on the existing loading condition at the output port. A convenient way to determine the power coupled into the detectors is to use diode detectors, also known as amplitude detectors. These kinds of circuits make use of a diode (usually a Schottky diode) to convert the RF power applied at its input to a DC voltage at the output. In practice, the output DC voltage returned by the diode is not always linear with the applied input power. In fact, this condition is met only at very low input power levels, situation in which the diode is working in the square law regime. When the input powers are getting higher, the diode is not returning a proportional DC voltage

71

anymore. In order to satisfy the six port requirement of linear response, a diode linearization step has to be also performed. This will be presented in Chapter 6. Once linear voltages are available, the six port reflectometer can be used to measure any loading condition inside the Smith chart.

Based on the principles illustrated in this section, a proposed topology for the six port reflectometer has been developed and tested, while still keeping the package integration size requirements. Before starting the description of this implementation, it is useful to provide a perspective of some representative six port designs published in literature and analyse their performance and limitations.

4.3 Literature review

The six port reflectometer is currently a fully established way of measuring the reflection coefficient at the output of any power amplifier. From its very early days and till present time, it knew a constant attention, in both terms of design, as well as calibration algorithms. What is more admirable about this circuit is that after several decades of existence, it's still a topic that generates a large number of scientific papers each year. Even though analysing the chronological development of this device is actually more the scope of a full book, as seen in [5], this section proposes to realize a succinct view on the way in which the six port developed, and its most important milestones until present day. Various published designs will also be shown for a clearer look on the practical requirements on this topic.

The six port reflectometer design began in an incipient form back in 1947, when the paper of Samuel [6] first described an oscillographic way of measuring the reflection coefficient, by making use of a length of waveguide with four power probes placed inside. This implementation also illustrated one of the problems that are even in the present day existent in the design of such circuits. Because the spacing between each two independent power detectors is frequency dependent, the six port reflectometer gives sometimes a narrow bandwidth. The quest to improve this issue was followed in subsequent papers by Cohn and Hoer [7] [8] who proposed implementations that slightly increased the bandwidth of operation. A milestone in the history of the six port junction was represented by the paper of Engen [9], which proposed for the first time this circuit as a viable solution to replace the use of directional couplers in the sense of measuring the reflection coefficient. This was a very important step, as heterodyne detection was at that time the solution of choice in detecting the output mismatch. Engen also wrote the first major paper on the six port technology [1] in 1977, a paper that remains up to date one of the major references in the six port literature. It presented in a concise way the method of using amplitude detectors to calculate Γ_L, it analysed the influence of detector noise, and it provided useful design guidelines.

The measurement of the S parameters of a particular device got also a new approach together with the development of the six port reflectometer. It was very quickly found that two six ports can be used as a simple way of fully measuring the S parameters of a device under test (DUT). The first paper introducing this concept was written by Hoer [10] and proposed the topology presented in Fig. 4.9.
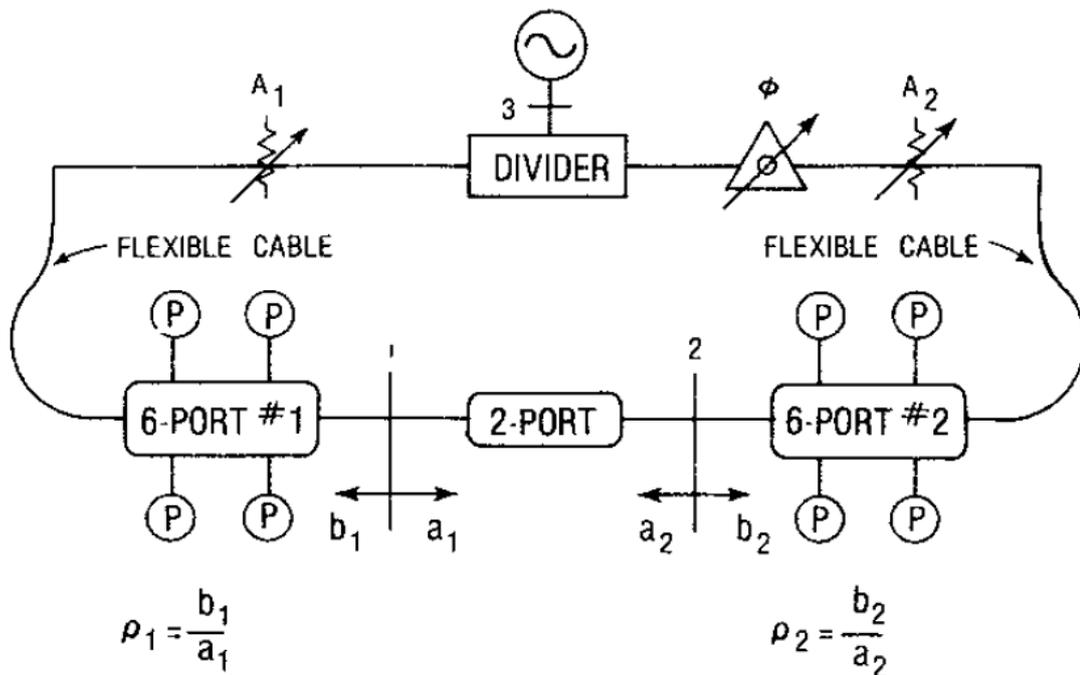
Fig. 4.9 - Way of measuring the S parameters of a device by using 2 six port reflectometers, as suggested in [10].

The paper of Engen [1] also first introduced the idea that adjusting the design of the six port can lead to an improvement in terms of noise. He suggested that the centres of the circles representing the locus of Γ_L as determined by a pair of power detectors must lie on circle, and have a spacing of 120° between each of them. This consideration was valid if one of the detection ports is selected as a reference port and it is sensitive only to the forward power wave. In practice, this specific phase shift of 120° proved to be difficult to achieve, and some published implementations managed to obtain a spacing of 90°, 90°, 180° [11], as presented in Fig. 4.10, or 135°, 135° and 90° [12], as presented in Fig. 4.11.
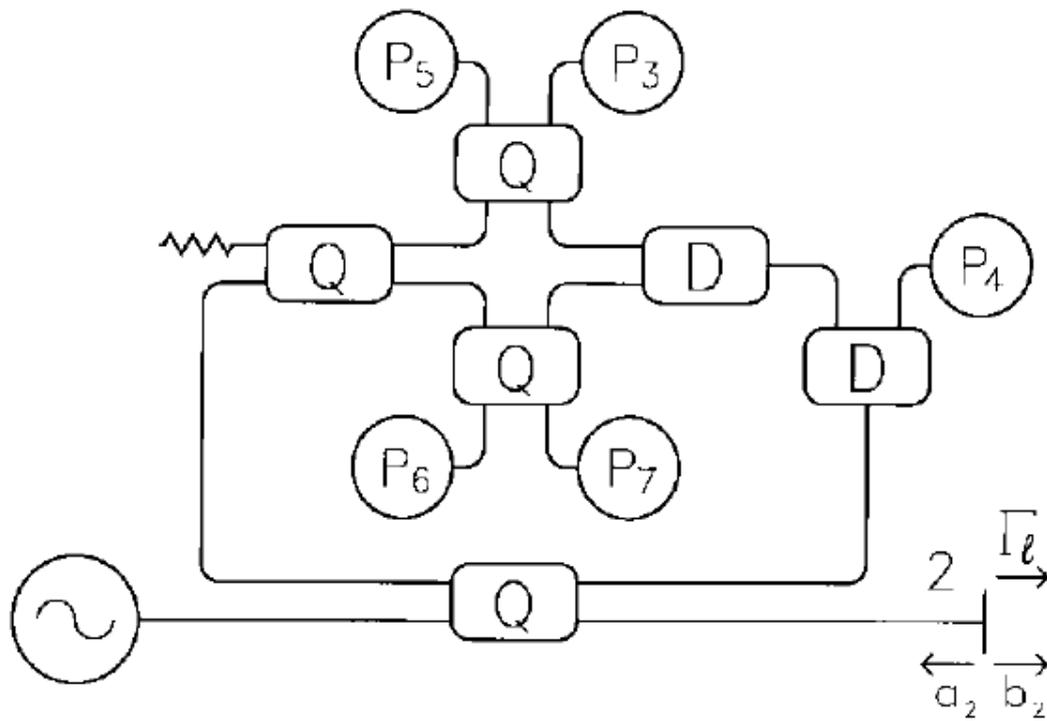
Fig. 4.10 - Block diagram of the six port reflectometer described in [11].
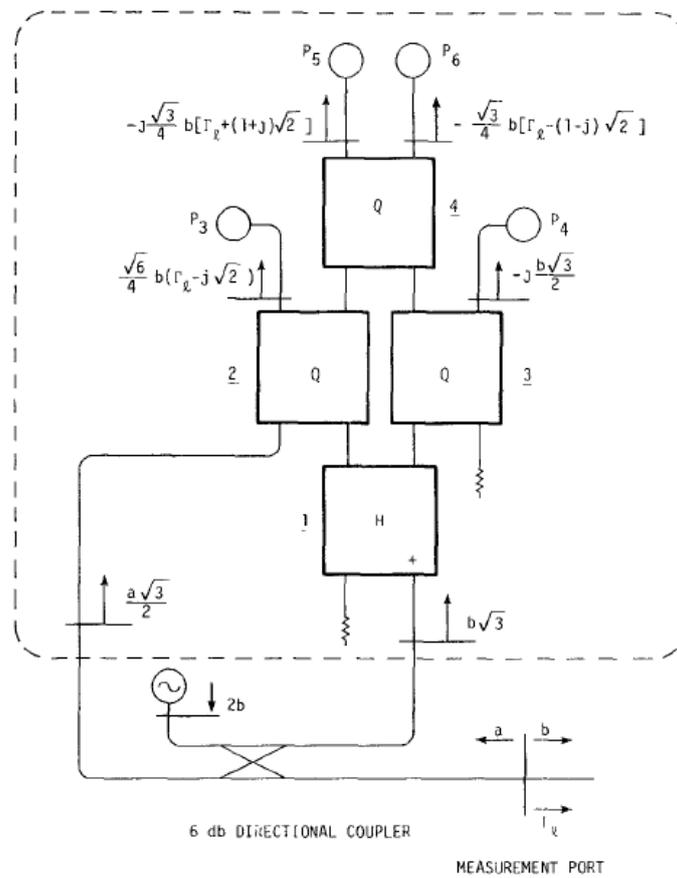
Fig. 4.11 - Block diagram of the six port reflectometer described in [12].

74

The common feature about these two designs is the fact that both of them use quadrature couplers in order to create the desired phase shift between the detectors. Therefore, their size is considerable (especially at lower frequencies) and the amount of power coupled by the detection ports is relatively high. A different approach was taken by the circuit introduced in [13], which made use of a directional coupler, together with a four port ring. Inside the ring, one of the ports was the port where the unknown load was placed. This implementation, which is presented in Fig. 4.12, had therefore again one of the four detection ports sensitive only to the forward wave (the port connected through the directional coupler).
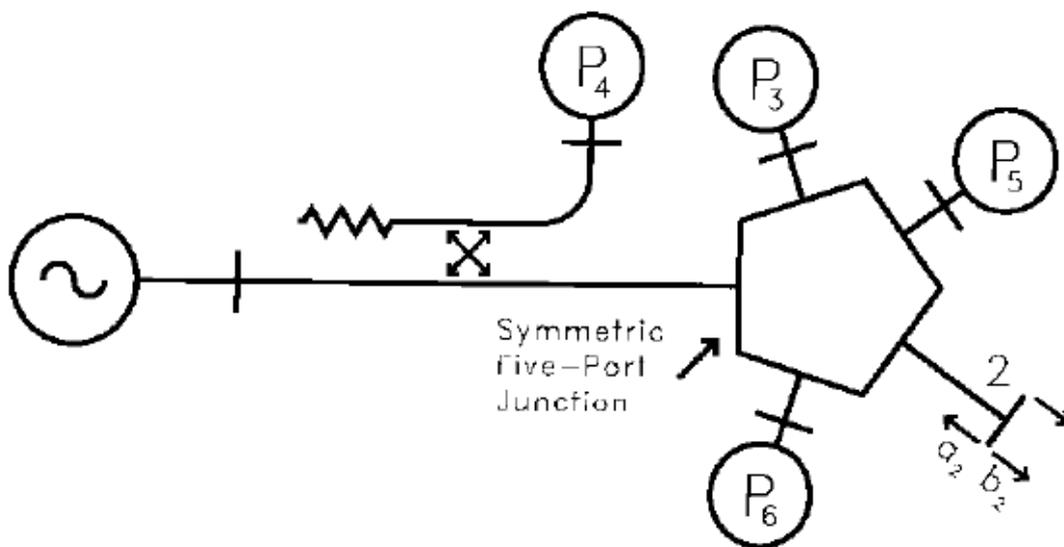
Fig. 4.12 - Block diagram of the six port reflectometer described in [13].

It was stated that a different category of six port circuits does not assume this reference port configuration. This is the case if none of the four power detectors is sensitive only to the forward wave. The basic way of creating a six port without a reference was presented in several papers, among which [14] and [15]. These circuits are presented in Figs. 4.13 and 4.14. Paper [14] makes use again of quadrature couplers in order to create the required 90° multiples shifts between the forward and reflected waves. The six port from [15] has one quadrature coupler and two rings in order to obtain the four required powers.
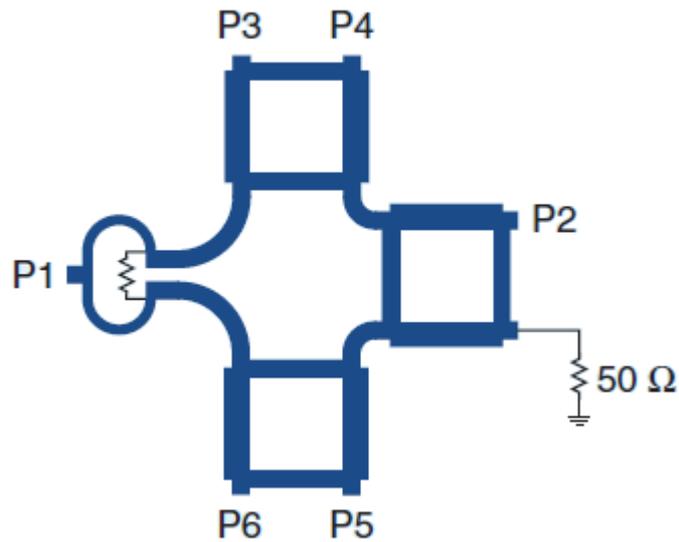
Fig. 4.13 - Six port reflectometer without a reference detector, as described in [14].
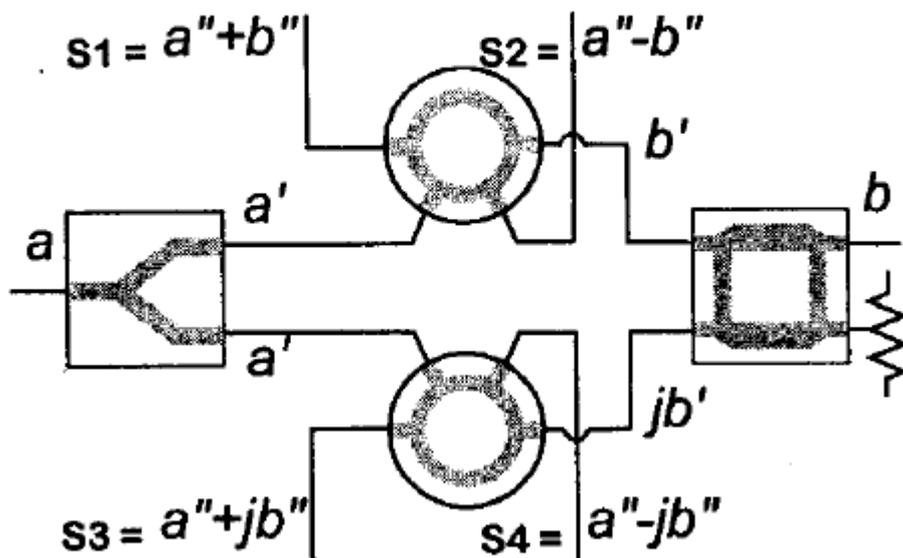
Fig. 4.14 - Six port reflectometer without a reference port, as described in [15].

Nowadays most of the published six port reflectometers make use of one of these presented topologies. Good modern examples of six ports including a reference power port were published in [16] - [18]. Figs. 4.15 and 4.16 present the circuit designs published in [17] and [18].
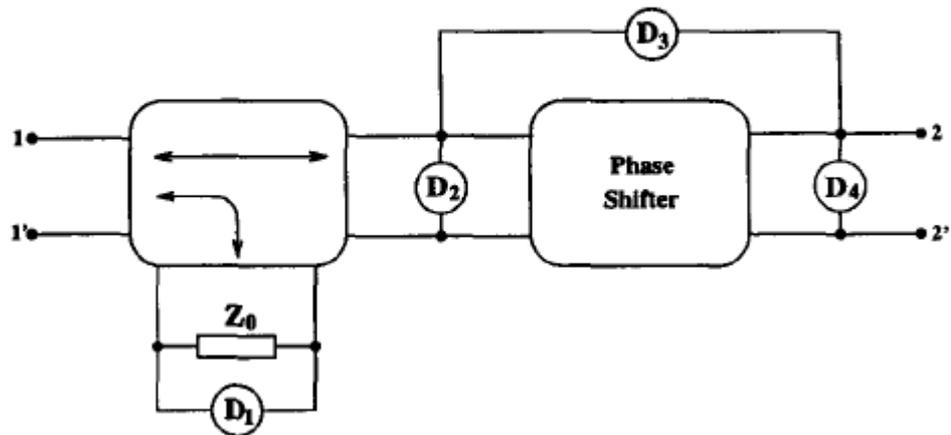
Fig. 4.15 - Block diagram of the six port reflectometer described in [17].
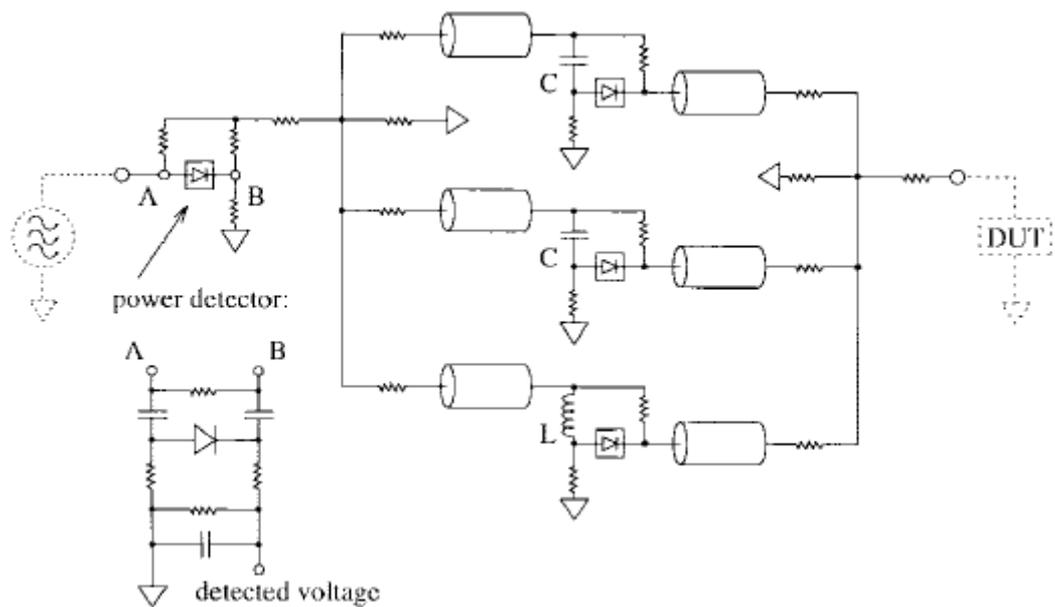
Fig. 4.16 - Block diagram of the six port reflectometer described in [18].

Six port designs without a reference port were also developed and good examples of this kind can be found in [18] - [20]. Figs. 4.17 and 4.18 represent the schematically drawn circuits presented in [19] and [20]. It is useful to observe that the design in [20] makes use of lumped elements in order to generate the desired phase shifts between the four power detectors. As it will be mentioned later in this chapter, a lumped element implementation can result in a design more compact than the ones making use of transmission lines as phase shifting elements.
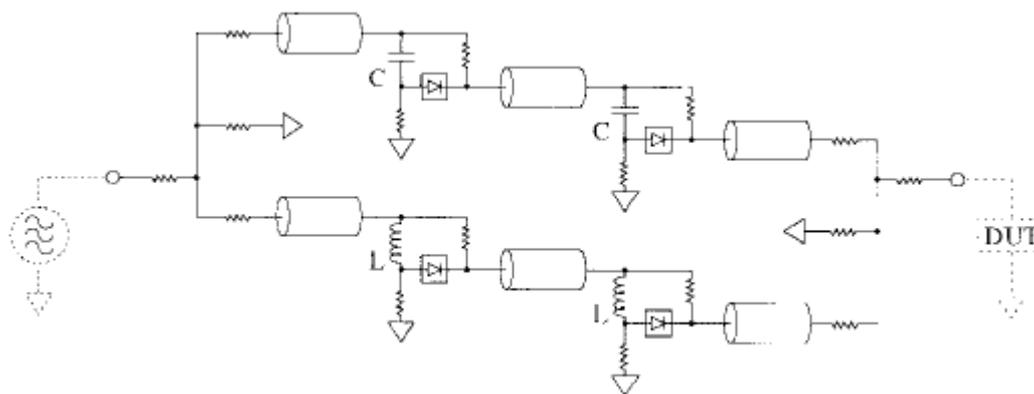
Fig. 4.17 - Block diagram of the six port reflectometer described in [11].
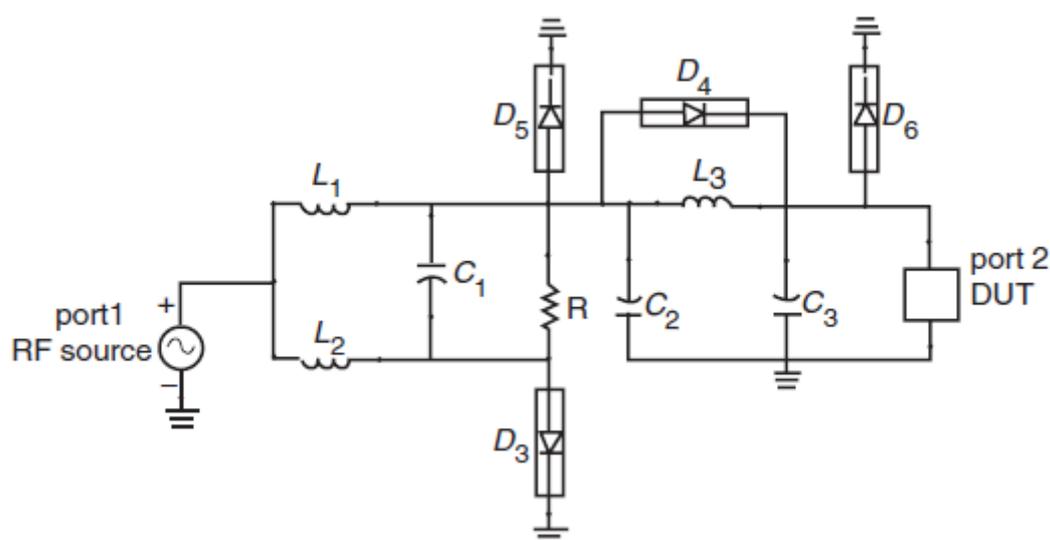
Fig. 4.18 - Block diagram of the six port reflectometer described in [20].

It can therefore be seen the fact that six port technology has evolved a lot during these decades. It is also worth mentioning papers that took some time to create an overview of the current six port literature. Great examples of this kind can be found in [3] [11] [14].

Some remarkable examples of the six port measurement technique were shown so far in this section. However, a deeper check on the above presented topologies shows one problem that was very often neglected. This is the size of the six port junction. When package integration is not the target of the design, the occupied area is not so important. Analysing the previous presented six port designs leads to the conclusion that it is very difficult to talk about their package integration. This is because most of them make use of branch line couplers, ring couplers or microstrip line phase shifters in order to create the required conditions at the detection ports. Considering the design procedure for those components (for example branch line couplers require $\lambda/4$ segments), the total resulted area for the six port is quite large. Several attempts on integrating the six port were however been done, as published for example in [17]

78

and [21]. By using the MMIC integration process, the sizes of the final layouts in these 2 examples are very compact, being 2 mm^2 [17] and 2.5 mm^2 [21]. In particular applications, integrated versions such as these ones can be very effective. However, they cannot be used in situations in which power has to be coupled in a contactless manner, like is the case in this work. In the design that will be introduced in the next section, the standing wave is first recreated in a contactless manner, then sampled by power detectors with correct phase shifting between them. This approach results in a package integratable design like the ones presented above, but for the first time designed for a particular application range: power amplifier output mismatch detection.

The goal of this project was to create a compact, package integratable six port reflectometer to analyse the waves flowing on the bondwire array present inside a transistor's package. Some of the presented designs from this section have impressive characteristics, especially with respect to their noise accuracy. Even though the final design is different than the ones illustrated in the above examples, the aim of this thesis was to reach competitive performance characteristics, while also managing to keep the design area to a minimum. In order to achieve this, a different way of making the coupling (contactless coupling), as well as a novel way to place the power detectors were introduced, and will be further described in Section 4.4 of this chapter.

4.4 Proposed implementation

The non MMIC six port reflectometer designs already published in literature presented in the previous section share the size problem. They are not targeted for package integration and therefore the authors were not constrained by the size of the whole circuit. On the other hand, the attempts to make MMIC package integrated six port reflectometers resulted in very compact designs, but placed the power detectors in between the input and the output ports of the circuit. The main goal of this work is to make a compact mismatch detection circuit, which is capable to fit inside the package of a power transistor device, while also coupling the power in a contactless manner, therefore influencing as little as possible the performance of the power transistor. The first problem that comes into mind when talking about in package coupling is the way in which the coupling is done. This issue has been already discussed in Chapter 3. The proposed idea was to make use of the bondwires connecting the drain bar of the power transistor to the package drain lead. The number of bondwires present inside a power amplifier package is varying from application to application. However, the principle proposed in this work does not depend on this number, and it is universally functional with any output bondwire array. In order to be able to couple some of the power flowing through the bondwires, a coupling element has to be designed and placed next to the bondwire array.

The schematic idea in which the coupling from the main line is performed in the case of the proposed six port reflectometer was presented in Fig. 4.1. On the coupled structure four power detectors will be placed. If power is going to be reflected from port 2 in Fig. 4.1 (i.e. we have a reflection coefficient bigger than 0), a standing wave will exist along the main line, as it was illustrated in Fig. 2.3. This situation is presented here again in Fig. 4.19 for convenience.
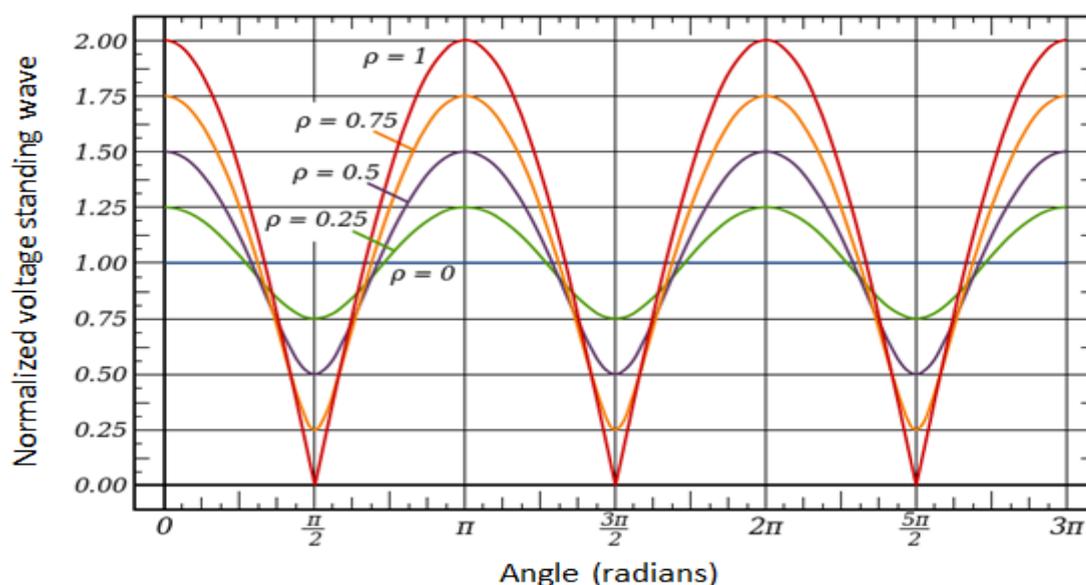
Fig. 4.19 - Standing wave ratio present on a transmission line terminated with various mismatched load impedances. $\rho = |\Gamma_L|$.

The secondary line will couple a fraction of the power flowing through the main one, depending on the coupling factor. Then, this line is sampled at four different points in order to obtain four powers. It was explained in the chapter dedicated to the directional coupler that two voltage magnitudes can determine a circular locus of possible Γ_L values in the Γ_L plane. Therefore, three pairs of detectors will lead to three circular loci for Γ_L, which will ideally intersect in a single point, representing the complex value of the reflection coefficient.

It was presented earlier in this chapter that the biggest limitation in the accuracy of the six port reflectometer is represented by the detector noise. This is why all the six port designs that are published nowadays are built in such a way that the impact of this noise is reduced to a minimum. Design considerations on this subject have already been presented in Section 4.2. It was shown that different ways to reduce the noise impact apply depending on the chosen six port architecture. One way to design the six port circuit for minimum noise impact is to consider one of the four detection ports as a reference, and determine the reflection coefficient as the intersection of three circles having the centres placed on a equilateral triangle on a circle with the centre in the origin of the Γ_L plane. In the design that has been introduced in this section, it is however not possible to use one of the detectors as a reference, as it is not possible to make the detector sensitive only to the forward wave. This problem was investigated also in literature, as saw in Section 4.2. The conclusion was to position the four "q" points introduced

in Section 4.2 on a circle with the centre in the origin of the Γ_L plane, with 90° spacing between each two of them. The way in which this phase shift is achieved in practice is by using quadrature couplers placed conveniently between the input port (port 1) and the output port (port 2), such that the forward and reflected power waves appear with a shift of 90° at each detector port. Unfortunately, again this approach is not possible in our discussed case. Because ports 1 and 2 (input and output) are connected together by the bondwire array, it is not possible to place the quadrature couplers directly between them such that the waves are sampled individually. The way in which the coupling is done in our situation is by the use of a directional coupler placed close to the bondwire array. However, because of a medium achieved directivity (10 to 15 dB depending on the selected directional coupler design), it is not possible to fully separate the forward and reflected waves, and therefore individual 90° shifting of them is not possible. As these limitations (especially the directional coupler's directivity) cannot be solved within the context of very low area, a new way of limiting the impact of detector noise was developed.

As explained, depending on the loading conditions present at port 2, a standing wave will exist along the bondwires. The goal in placing the four detectors is to put them in four independent locations along the standing wave. This means they cannot be placed randomly, because in a worst case scenario two of them can sense the same voltage in two different points along the standing wave. This wave is always periodic, with the period of π. This amount of phase shift can be achieved by a $\lambda/2$ length of microstrip transmission line at the design frequency. Considering this, it is reasonable to think that if all the four detectors are placed within this $\lambda/2$ length, then all of them will have an individual position along the standing wave, and it is impossible that two detectors will sense the same point. Continuing with the conclusion that all four detectors have to be placed inside the same standing wave period, next the proper positioning of the power detectors in order to minimize the noise impact has to be investigated. Due to certain factors, such as non-ideal voltage readout, or voltage linearization error, the detector indication will have a certain noise level added over the correct value. Ideally, in a noiseless situation, the detectors can be placed anywhere within a period of the standing wave, situation in which all of them will still sense independent positions. However, because of the noise, their position along the pattern can deviate depending on the noise level, and they can end up giving the same output for different positions in case they are placed too close to each other. This possible situation is depicted in Fig 4.20.
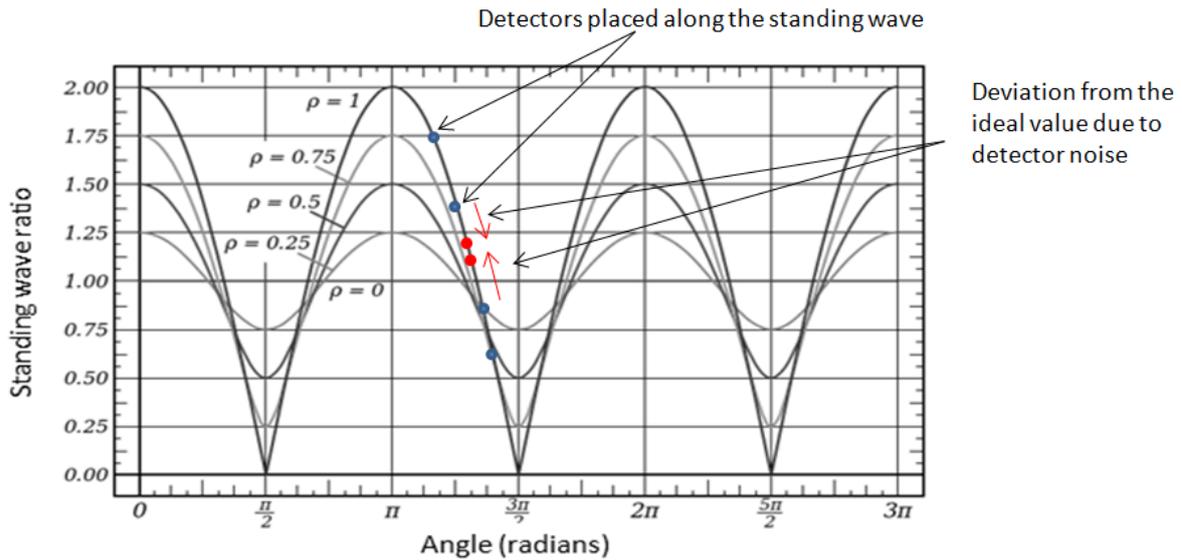
Fig. 4.20 - Effect of noise on a set of power detectors placed very close to each other on the standing wave period.

A logical inspection of the problem suggests that the best way to minimize the noise impact is to place the detectors as far away from each other as possible. In the analysed case, considering the $\lambda/2$ spatial periodicity, the detectors can be placed each at $\lambda/8$ distance from the next one, thus covering the whole pattern. This is presented in Fig. 4.21.
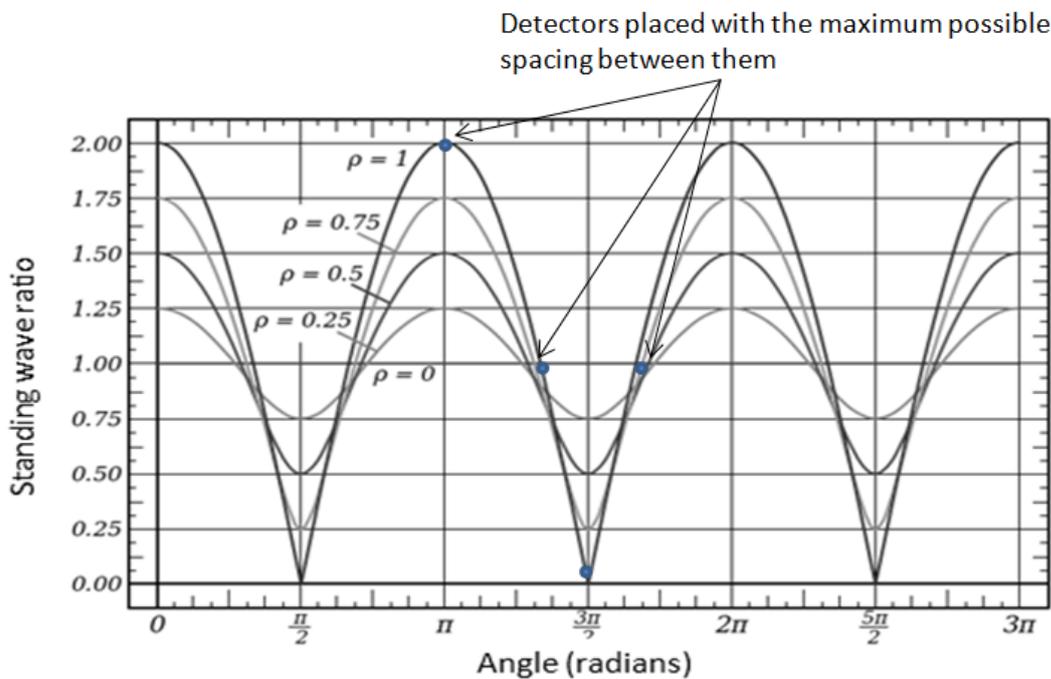
Fig. 4.21 - Proposed placement for the four power detector, providing the maximum spacing between each of them inside a period of the standing wave.

The frequency range that the application is targeting is the ISM band centred at 2.45 GHz. At this frequency the wavelength on a 6.5 ε_r substrate has a length of 48 mm. Considering the periodicity of the standing wave, the period will have $\lambda/2$ mm or 24 mm. The bondwire lengths

82

that are considered in application target usually have lengths varying between 1.5 and 4 mm, and rarely reaching more than 6 or 7 mm. Thus, placing a simple microstrip line underneath them will cover only a very small portion of the standing wave period, and would be of no use with respect to the noise minimizing solution described above. The approach that was taken to solve this issue is to close the coupled microstrip line in a loop of exactly $\lambda/2$ length at the design frequency. In this way, the forward and reflected waves from the bondwire array are coupled in the loop, and they interfere along it. Thus, the standing wave pattern existing along the bondwire array is recreated inside the loop. The loop implementation can also easily accommodate the required 24 mm in total to get the whole period of the standing wave. Finally, the loop is tapped four times, with a distance of $\lambda/8$, or 6mm between each two consecutive tapping positions. The taps will represent the four detector ports. The above described implementation is presented as an ADS Momentum layout in Fig. 4.22.
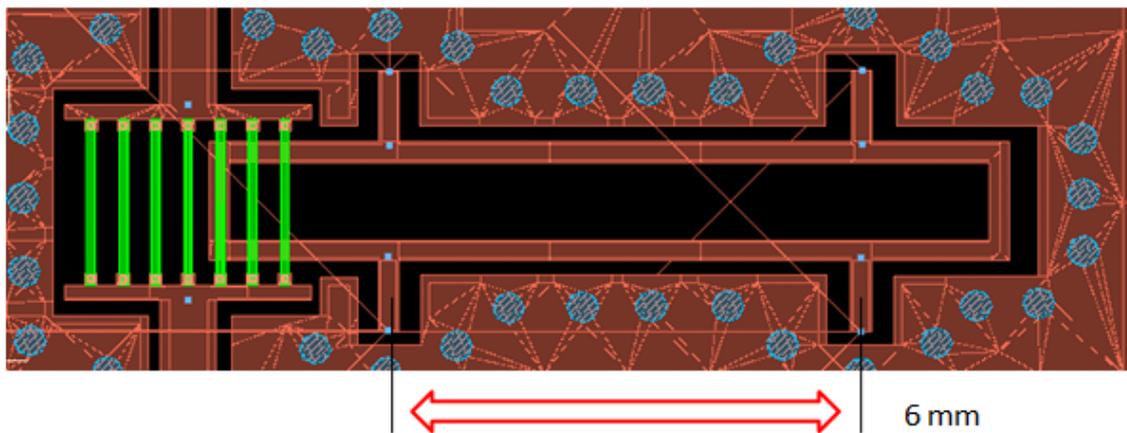
Fig. 4.22 - ADS Momentum layout illustrating the proposed spacing between two consecutive detectors.

The green lines represent the bondwire array, while the brown line is the microstrip loop. It can be seen that the loop is tapped four times, each time at a distance of 6 mm from the previous tap. The whole loop and tap points are surrounded by a ground plane.

The discussion made in the previous chapter regarding ways of coupling power from the bondwire array holds also for the coupled loop. Considering the above figure, power gets coupled into the loop at its left side. Considering only the closest two tapping points from the bondwire array, this implementation is identical to the directional couplers analysed in Chapter 3. Thus, one can choose again from the analysed ways of coupling, involving the loop placed underneath the bondwires, the loop placed next to the bondwires, and an extra bondwire placed next to the bondwires. For the reasons highlighted in the previous discussion (highest directivity, lowest coupling factor considering a bondwire length of 2.5 mm), the implementation with the loop placed at the side of the bondwire array would give the best performance. However, in practice there are several limitations that make this choice less reliable. First of all, placing the side of the coupled loop exactly underneath the bondwire array

will result in a more uniform coupling, from all the bondwires, compared with the first option which was mostly coupling power from the side bondwire. Related to this is also the issue of unbalancing the bondwire array. It is known that this bondwire array plays an important role in creating the output matching network of the power amplifier. Placing the coupled microstrip line at the side of the array will therefore have a different, non-uniform impact on the array's bondwires, unbalancing the behaviour of the matching network. Finally, placing the loop next to the bondwires instead of placing it underneath the array adds 2 extra mm to the horizontal length of the loop. Since we are targeting package integration, every economy in area is highly priced. Therefore, a trade-off has been made and the implementation with the side of the loop placed underneath the array was physically produced and tested, the results being shown in Chapter 7 of this work. Images of the Ansys HFSS graphical model, as well as the produced prototype test board are presented in Figs. 4.23 and 4.24.
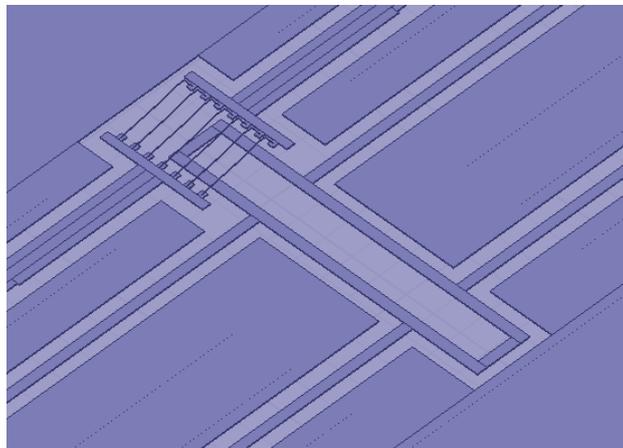
Fig. 4.23 - Ansys HFSS layout of the proposed six port design.
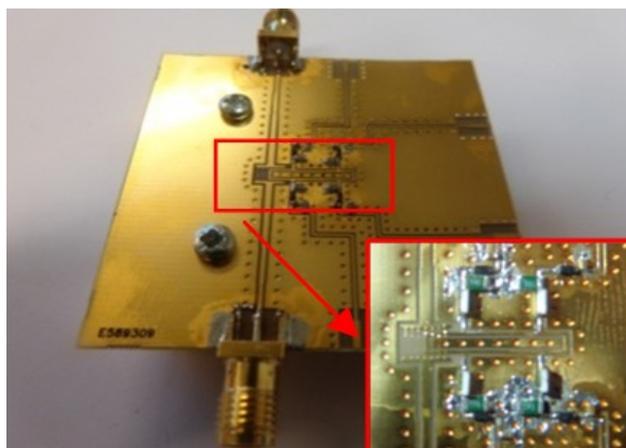
Fig. 4.24 - Produced test board of the proposed six port design.

Once the loop implementation has been validated, possible ways of making it smaller, still using transmission lines as phase shifters, can be analysed. If the distance between each two consecutive detectors is kept constant at the value of 6 mm, then the loop can be designed

in a different way, minimizing the total occupied area, as presented in Fig. 4.25. Simulations were made on this kind of modified layout and returned the same good results.
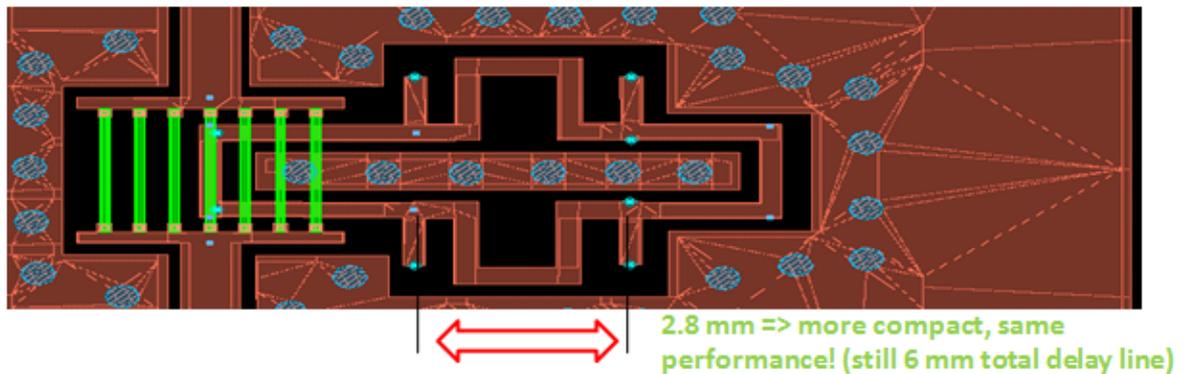
Fig. 4.25 - Possible way of reducing the total six port reflectometer's area by shrinking the lines connecting two consecutive detectors.

It was stated earlier in this section that the whole effort put in placing the power detectors at certain spacing between them helps in minimizing the influence of the detector's noise. In order to prove the validity of the proposed implementation in terms of noise performance, several tests were performed, the results being described in the next section.

4.5   Noise analysis

The most important reason why the 45° shift between two consecutive detectors approach was taken was to minimize as much as possible the influence of noise. Noise in the detector readings can arise from various factors, including noise introduced by the readout circuit, or linearization errors. Before the final test board was produced, simulations were performed to observe the influence of noise to the final determined reflection coefficient. First, 1000 uncorrelated random noise samples were created. They were later added to the ideal detector voltage readings, as taken from the simulated schematics. The noise samples were created with an amplitude -50 dB lower than the maximum detector returned DC voltage. Therefore, a dynamic range of 50 dB was assumed for this simulation. This dynamic range is comparable to commercial log detectors, and even lower than the dynamic range obtained using the custom made power detectors built for this application as it will be seen in Chapter 6. Therefore, the errors introduced in this step are even bigger than the worst case error that could happen during the six-port operation.

First, the noise samples were added to voltage readings generated by a loop with 10° shift at the design frequency between two consecutive detectors. This means that each two consecutive detectors are separated by 1.3 mm, and they are much closer than the desired λ/8 distance. Different loads covering the Smith chart were analysed and the results are plotted in Fig. 4.26.
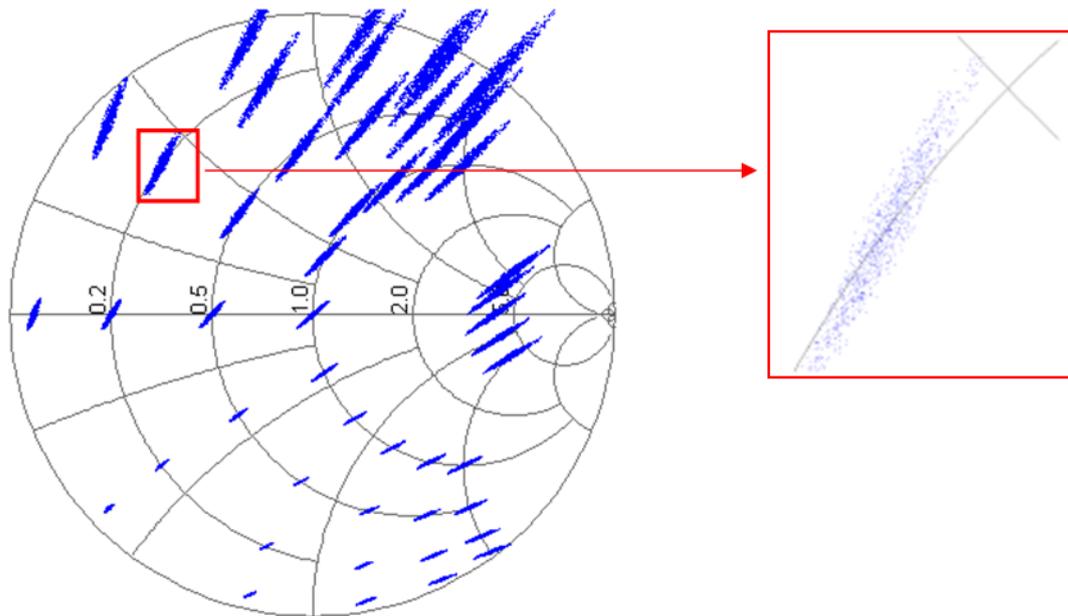
Fig. 4.26 - Monte Carlo noise analysis of a six port reflectometer design where the power detectors are placed on a loop with 10˚ phase shift between each two consecutive ones. The error is the result of a random -50 dB noise applied to each detector.

It can be seen that the noise is seriously affecting the determined Γ_L result, even though the noise amplitude is 50 dB lower than the detector reading. The spread gets larger as the impedances are placed closer to the edge of the Smith chart. This is because in that region certain detectors will always return a very low value, which will get at one point even comparable to the noise floor.

Next, the same experiment was made using a loop with 45˚ shift at the design frequency between each two consecutive voltage detectors. This is the phase shift at which the influence of noise should be minimized. The results for the same points on the Smith chart as in Fig. 4.26 are presented in Fig. 4.27.
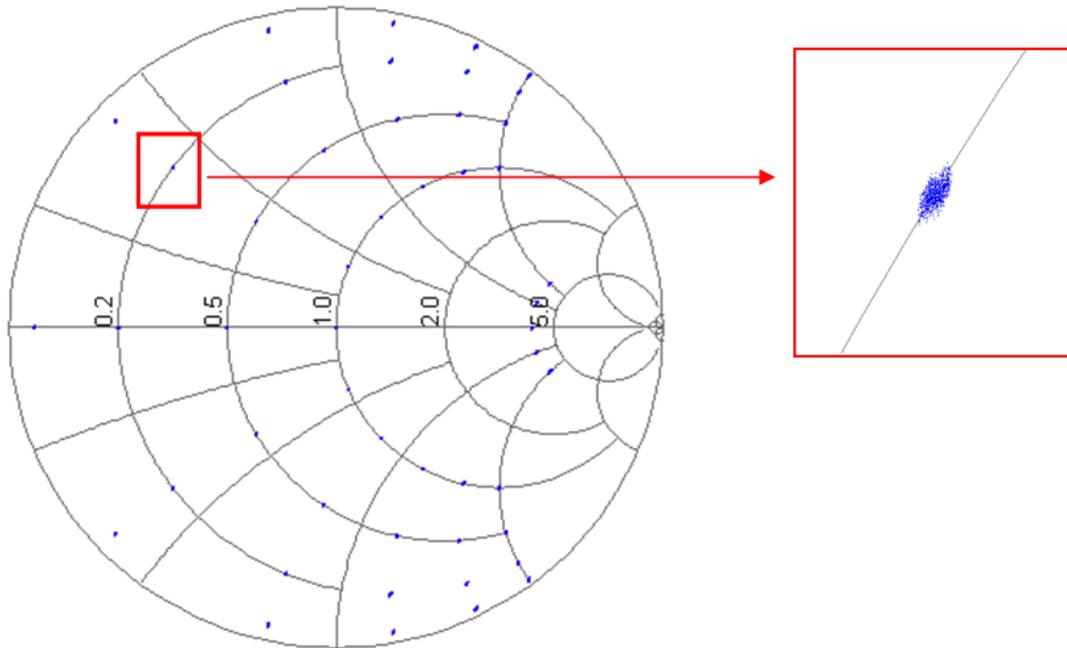
Fig. 4.27 - Monte Carlo noise analysis of a six port reflectometer design where the power detectors are placed on a loop with 45˚ (optimum) phase shift between each two consecutive ones. The error is the result of a random -50 dB noise applied to each detector.

Now the advantage of the 45˚ shift implementation is visible. Having the same amount of noise present at each detector, the spread in the calculated reflection coefficient has reduced significantly. Also, even the points located near the edge of the Smith chart are offering reliable results now, even though the influence of noise on them is still larger.

It is interesting to obtain also some information about the bandwidth of the designed six-port reflectometer. When calculating the length of the microstrip line to create the 45˚ shift, a frequency of 2.45 GHz was considered. If the frequency is changed, then the length of the microstrip transmission line between each two consecutive detectors will not be $\lambda/8$ anymore, but will become either smaller or larger. By keeping the circuit dimensions constant, and sweeping the frequency of the applied signal at the input port, the error versus frequency plot can be determined. This is presented in Fig. 4.28.
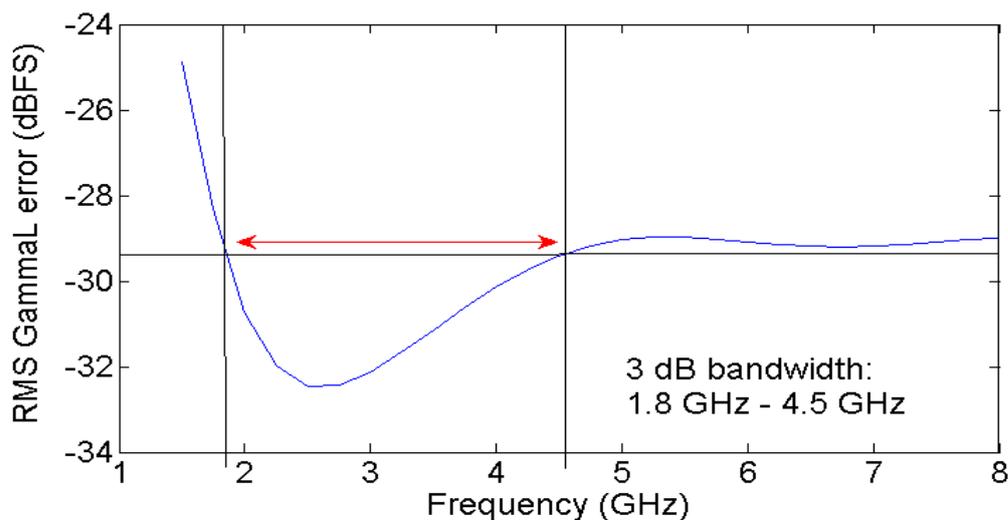
Fig. 4.28 - Bandwidth of operation for a proposed design operating at 2.45 GHz central frequency.

The rms error in the calculation of one sample reflection coefficient has been plotted. It can be seen that the error is minimum at the centre frequency of 2.45 GHz, as expected. When the frequency moves away from this centre point, the rms value of the error gets larger. The 3 dB error bandwidth can be determined using the lowest value of the error and the values located 3 dB higher on both sides. This 3 dB bandwidth is found to be 2.7 GHz, between 1.8 GHz and 4.5 GHz. This bandwidth specification adds flexibility to the design, as the frequency of operation can be shifted from the design frequency without introducing a significant amount of error to the determined result.

This section provided simulation results showing the utility of designing the six port reflectometer as proposed in Section 4.3 of this chapter. Considering the fact that this design approach was taken mostly in order to achieve a package integratable design, a proposed way of practically integrating the six port into an already existing power transistor package will be presented in the next section.

4.6 Package integration

The starting goal of the project was to integrate mismatch sensing circuitry inside power amplifier packages. This is why the six port dimensions were reduced to a minimum, while still keeping the original accuracy specification. The PCB containing the microstrip loop that is used to couple the power from the bondwire array has in the end compact dimensions, 9.4 mm x 4 mm, with 0.2 mm height. This small area permits the loop to be integrated inside a power amplifier package, without modifying the design of the transistor's internal power dies. The targeted package is the SOT111A package, presented in Fig. 4.31.
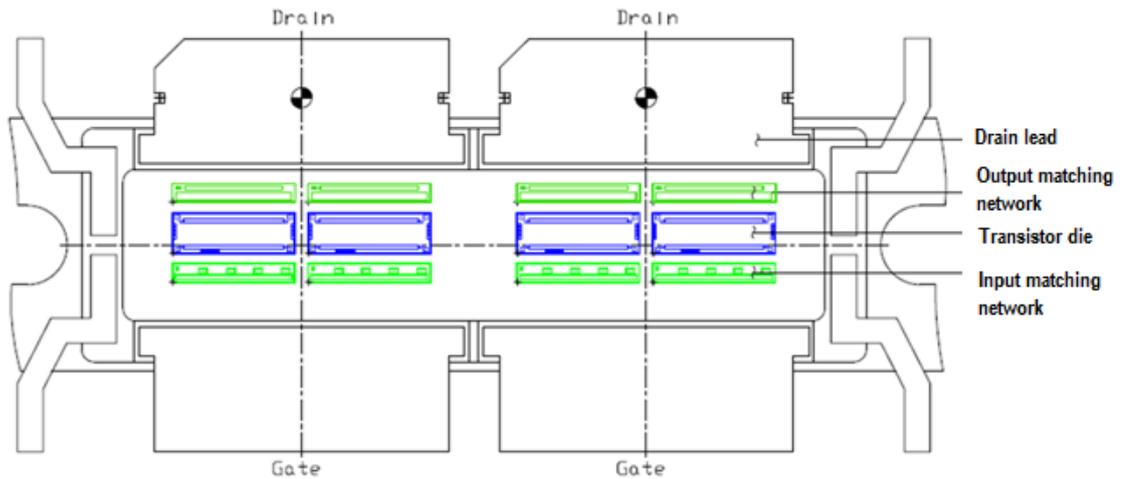
Fig. 4.29 - Commercial SOT111A power transistor package.

Originally, this package was designed to host four power transistor dies, as presented in the figure above. If two of the four dies are removed from the package, there is enough free space available to place the designed coupled loop, as well as the diode power detectors. Schematically, the microstrip loop will be placed in the package as presented in Fig. 4.32, as close as possible to the bondwires connecting the drain bar to the drain outside lead.
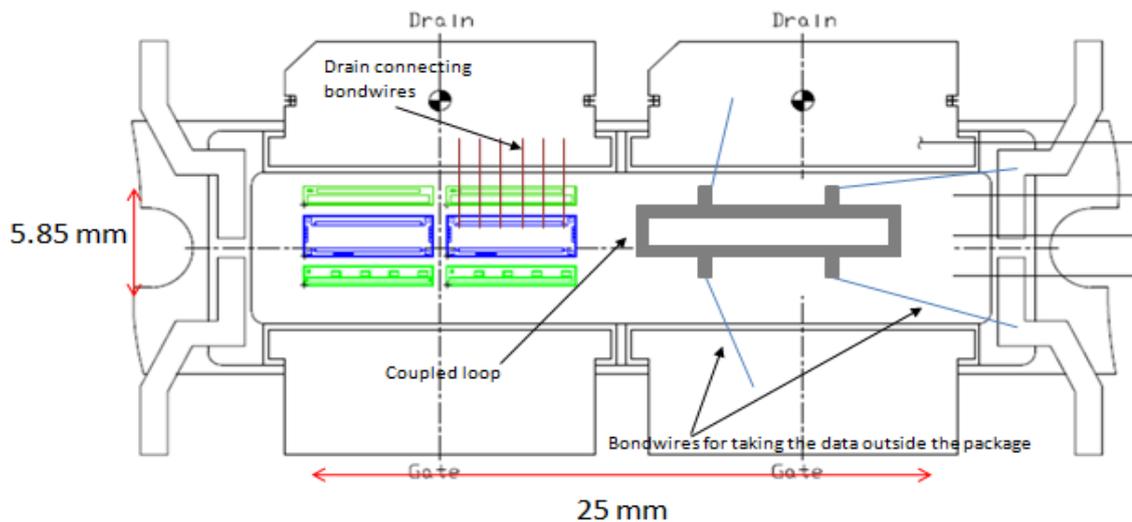
Fig. 4.30- SOT111A package with 2 power dies removed and the proposed coupled loop placed on the right hand side.

By analysing the specified package dimensions, it can be seen that the coupled microstrip loop can easily fit in the right hand side half of the package. Also, another reason why this package was chosen is the available extra outside leads, to the sides of the package. After the power was coupled to the microstrip loop and converted to DC voltage by the diode detectors, one needs to route these voltages outside of the package in order to be further used and processed. The extra four pins available on this package are perfect for the four diode detector outputs, and simple bondwire based connections from the output of the diode detector

to the pins are enough to transfer the voltage. Also, since this voltage is DC, it does not matter the length or size of these bondwires, which makes the design more flexible.

In practice, one microstrip loop with four diode detectors has been successfully placed inside the transistor's package, as indicated schematically in the above figures. The result is shown in Fig. 4.33.
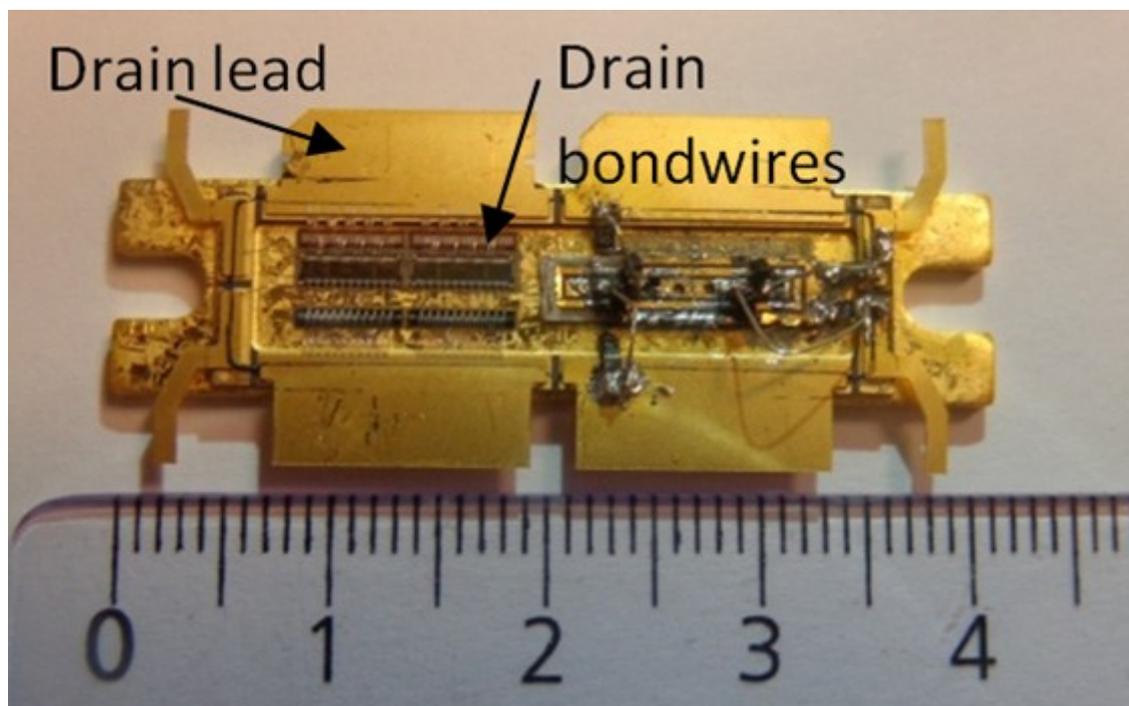
Fig. 4.31 - Practical implementation of the drawing in Figure presenting the coupled loop PCB placed in package next to the power transistor dies.

It was mentioned in Section 4.3 of this chapter that implementing the phase delay elements with lumped components instead of transmission lines could be a valuable way of reducing the size of the reflectometer loop. The limited time available for this project did not permit a practical implementation involving lumped element. However, this approach is one of the important next steps that will be made in the development of the proposed six port reflectometer, and a basic description of the method will be given in the "Future work" section from Chapter 8.

An approach for a package integratable six port directional coupler was presented and its functionality was demonstrated by simulations during this chapter. Obviously, no matter how accurate a simulation might be, practical measurement data is always required to prove a principle. Measurement results for this six port reflectometer will therefore be given in Chapter 7. In order to calculate the value of the reflection coefficient at the output port, an extra step has to be made besides monitoring the four detected powers. This is an initial six port calibration. Several algorithms of calibrating the six port junction will be presented in the next chapter, before they are used to demonstrate the practical functionality of the design in Chapter 7.

References

[1] G. F. Engen, "The Six Port Reflectometer: An Alternative Network Analyzer", IEEE Transactions on Microwave Theory and Techniques, vol. MTT-25, no. 12, December 1977.

[2] G. F. Engen, "Determination of Microwave Phase and Amplitude From Power Measurement", IEEE Transactions on Instrumentation and Measurement, vol. IM-25, no. 4, December 1976.

[3] K. Staszek, S. Gruszczynski, K. Wincza, "Theoretical Limits and Accuracy Improvement of Reflection-Coefficient Measurements in Six-Port Reflectometers", IEEE Transactions on Microwave Theory and Techniques, vol. 61, no. 8, August 2013.

[4] S. O. Tatu, K. Wu, "Six Port Technology and Applications", Telsiks 2013.

[5] F. M. Ghannouchi, A. Mohammadi, "The Six Port Technique", Artech House, 2009.

[6] A. L. Samuel, "An oscilloscope method of presenting impedances on the reflection-coefficient plane," Proc. IRE, vol. 35, pp. 1279–1283, November. 1947.

[7] S. B. Cohn and N. P. Weinhouse, "An automatic microwave phase measurement system," Microwave Journal, vol. 7, pp. 49–56, February 1964.

[8] C. A. Hoer, "The 6-port coupler: A new approach to measuring voltage, current, power, impedance, and phase," IEEE Transactions on Instrumentation and Measurements, vol. IM-21, November 1972

[9] G. F. Engen and C. A. Hoer, "Application of an arbitrary six-port junction to power measurement problems," IEEE Transactions on Instrumentation and Measurements , vol. IM-21, November 1972.

[10] C. A. Hoer, "A Network Analyzer Incorporating Two Six Port Reflectometers", IEEE Transactions on Microwave Theory and Techniques, vol. MTT-25, no. 12, December 1977.

[11] G. F. Engen, "A (Historical) Review of the Six-Port Measurement Technique", IEEE Transactions on Microwave Theory and Techniques, vol. 45, no. 12, December 1977.

[12] G. F. Engen, "An Improved Circuit for Implementing the Six-Port Technique of Microwave Measurements", IEEE Transactions on Microwave Theory and Techniques, vol. MTT-25, no. 12, December 1977.

[13] E. R. B. Hansson, G. P. Riblet, "An Ideal Six-Port Network Consisting of a Matched Reciprocal Lossless Five-Port and a Perfect Directional Coupler", IEEE Transactions on Microwave Theory and Techniques, vol. MTT-31, no. 3, March 1983.

[14] A. Koelpin, G. Vinci, B. Laemmle, D. Kissinger, and R. Weigel, "The six-port in modern society", IEEE Microwave Magazine, supplement, December 2010.

[15] J. Hyyrylainen, L. Bogod, S. Kangasmaa, H.-O. Scheck, and T. Ylamurto, "Six-port direct conversion receiver", Proc. 27th EuMC, vol. 1, pp. 341–346.

[16] K. Staszek, S. Gruszczynski, K. Wincza, "Broadband Measurements of - Parameters Utilizing 4x4 Butler Matrices", IEEE Transactions on Microwave Theory and Techniques, vol. 61, no. 4, April 2013.

[17] M. Ratmi, B. Huyart, E. Bergeault, L. Jallet, "A New Structure for a Six-Port Reflectometer using a Silicon MOSFET for Power Measurement" .

[18] J. Hesselbarth, F. Wiedmann, B. Huyart, "Two New Six-Port Reflectometers

Covering Very Large Bandwidths", IEEE Transactions on Instrumentation and Measurements , vol. 46, no. 4, August 1997.

[19] X. Z. Xiong, V. F. Fusco, "Wideband 0.9GHz to 5GHz six-port and its application as digital modulation receiver", Microwaves, Antennas and Propagation, IEE Proceedings, 2003.

[20] S. O. Tatu, E. Moldovan, K. Wu, R. G. Bosisio, "A New Direct Millimeter Wave Six-Port Receiver", Microwave Symposium Digest, 2001 IEEE MTT-S International.

[21] C. H. Wang, H.-Y. Chang, P.-S. Wu, K.-Y. Lin, T.-W. Huang, H. Wang, and C. H. Chen, "A 60 GHz low-power six-port transceiver for gigabit software-defined transceiver applications" Proc. 2007 IEEE Int. Solid-State Circuits Conf. (ISSCC'07), pp. 192–193.

5. Calculation and calibration algorithms

The previous two chapters presented the theoretical background as well as the design procedure for the bondwire based directional coupler followed by the bondwire based six port reflectometer.

After designing the coupling structure, one can use the information at the detection ports in order to determine the reflection coefficient at the test port. During this work, two different types of coupling structures were investigated: a simple two port directional coupler, and a four detector port loop structure constituting, which together with the main line acts like a six port reflectometer. This chapter will make an overview of the most important algorithms analysed for both of these two implementations in order to calculate the value of the reflection coefficient.

5.1 Directional coupler implementation

The measurement of the complex reflection coefficient at the output port of a power transistor does not represent a difficult measurement in today's applications if the required hardware is available. Depending on the detection circuit architecture, particular parameters are needed in order to determine the complex value of Γ_L. Several ways of doing this were mentioned in Section 2.4 of Chapter 2. The techniques divide in two main categories depending on the measured information, as follows: measurements in which the magnitude and phase of the coupled signal are available, or measurements in which only the magnitude of the coupled signal is available. The first option can be implemented by using a directional coupler together with a downconverting mixer measuring system. A discussion about the basic down converting mixer approach was earlier introduced in Chapter 2.

Alternatively, one can use only the magnitude of the coupled signal, which is easier to collect, in order to measure the magnitude of the reflection coefficient. This comes at the expense of needing a very good directivity between the coupled forward and reflected waves. This is because in the absence of phase information, the calculation method assumes that the signal at the forward coupled port represents only a fraction of the forward wave (the "a" wave), and the reverse coupled port couples only a fraction of the reverse wave (the "b" wave). In practice, industrial applications use large external directional couplers which are designed especially in order to achieve a high directivity. In this sense, directivities in the order of 30 - 45 dB are available, and the Γ_L magnitude measurements performed in this way are able to achieve errors below -50 dB.

As it was presented in a previous chapter, good directivity (over 30 dB) is hard to achieve in small, package integrated applications, such as the presented one. The measured directivity for one of the test bondwire couplers produced reported a result of 14 dB, which would introduce significant error in the calculation of Γ_L in case only the magnitudes of the coupled signals were used. Considering this practical limitation, a good approach towards the measurement of the complex reflection coefficient, while still making use of a medium directivity coupling structure is to increase the number of detectors from two to four, and rely only on magnitude information.

5.2 Six port reflectometer implementation

The most important reason of analysing and designing a six port reflectometer for reflection coefficient measurement is the ability of this circuit to calculate Γ_L by only using DC information. This would reduce the need for down converting mixers, which means a lower complexity for the overall detection circuit. Once the DC voltages are read, information about the RF power that gets coupled into that port is already available. More information about this procedure can be found in the section dedicated to the diode linearization technique. By knowing the powers, one can choose one of the calibration methods and algorithms that work for the six port reflectometer. Three of these methods were analyzed during this work, and they will be described in the following sub sections.

5.2.1 The use of measured S parameters

The method of measuring the S parameters of the device and then using them in order to find the reflection coefficient has been mentioned also in the chapter dedicated to the bondwire directional coupler. For this procedure, complex voltages are needed together with the measured S parameters. The idea of using complex voltages still stands also for the six port reflectometer, in which case any two of the four detection ports can be selected. However, this does not make sense, since the biggest reason why the six port reflectometer was introduced was to remove the complex voltage detection problem. By just using the DC voltages at the four ports, the reflection coefficient can still be accurately determined. In the following discussion, we assume for now that the S parameters of the six port network are known (e.g. measured using a network analyser), and also that the four detectors are matched as well as possible at their input, therefore having a low return loss. Later on we discuss the more general case, when the properties of the six-port reflectometer are not known on forehand.

For the six-port network, the schematic image presenting the forward and reflected power waves at all ports was presented in Chapter 4, and it is reproduced here again for convenience in Fig. 5.2.
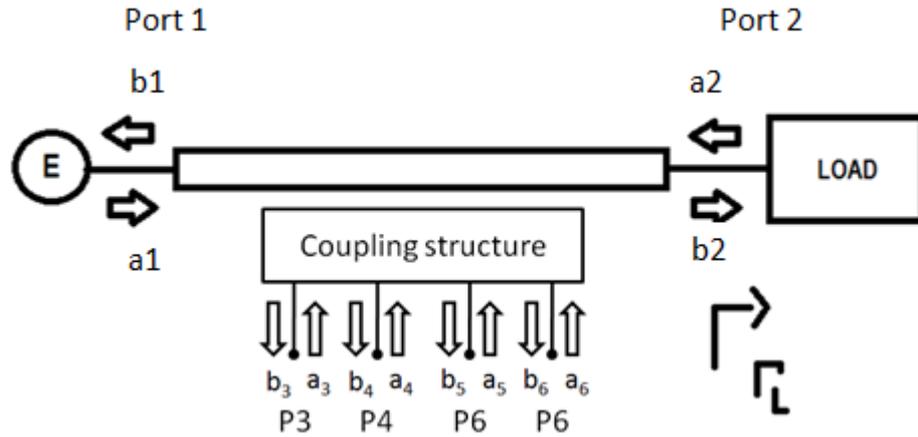
Fig. 5.1 - Schematic representation of the 6 port network, indicating the forward and reflected power waves as each port.

These forward and reflected waves are related to each other by the S matrix of the six-port network, as presented below.

$$
\begin{pmatrix} b_1 \\ b_2 \\ b_3 \\ b_4 \\ b_5 \\ b_6 \end{pmatrix}
=
\begin{pmatrix}
S_{11} & S_{12} & S_{13} & S_{14} & S_{15} & S_{16} \\
S_{21} & S_{22} & S_{23} & S_{24} & S_{25} & S_{26} \\
S_{31} & S_{32} & S_{33} & S_{34} & S_{35} & S_{36} \\
S_{41} & S_{42} & S_{43} & S_{44} & S_{45} & S_{46} \\
S_{51} & S_{52} & S_{53} & S_{54} & S_{55} & S_{56} \\
S_{61} & S_{62} & S_{63} & S_{64} & S_{65} & S_{66}
\end{pmatrix}
\begin{pmatrix} a_1 \\ a_2 \\ a_3 \\ a_4 \\ a_5 \\ a_6 \end{pmatrix}
$$

By starting with the assumption that the four detection ports are perfectly matched, one can consider the reflection coming back from them to be 0. In this way all the four waves b_3 - b_6 will be 0, and they can be excluded from the matrix.

This makes it possible to create the following system of nonlinear equations,

$$|b_3|=|S_{31}*a_1+S_{32}*a_2| \qquad (5.1)$$

$$|b_4|=|S_{41}*a_1+S_{42}*a_2| \qquad (5.2)$$

$$|b_5|=|S_{51}*a_1+S_{52}*a_2| \qquad (5.3)$$

$$|b_6|=|S_{61}*a_1+S_{62}*a_2|, \qquad (5.4)$$

which can be solved in an iterative way in order to determine a_1 and b_1. Finally, the reflection coefficient at the output port can be determined as a_1/b_1.

This method gives 100% correct results for perfectly matched detectors. In reality the detectors will not be perfectly matched at the input. This means that a certain amount of calculation error will be present in the final result, depending on the detector's return loss.

In conclusion, the S parameters method is able to provide good results in the specified conditions, as long as the S parameter matrix is known onforehand. As such an extra step is

required (measuring the S parameters with a network analyser) but no initial calibration needs to be made afterwards.

However, in practice it might not be always possible to measure the S parameters of interest. For example, in the case of the designed package integrated six port reflectometer that is the subject of this thesis, one of the network ports, more exactly port 1, will not be available for probing. This is because this port represents the drain of the power amplifier's die, and the die is placed inside the transistor's package. Alternative methods of calibrating the six port reflectometer do exist however published in literature. The next sub section will describe the use of a calibration method that requires seven known impedance standards presented at the output port.

5.2.2   Using an initial calibration step with seven standards

If the S parameters of the six port network are not known, then an initial calibration step needs to be made in order to use the six port reflectometer for Γ_L measurements. Several calibration methods are presented in literature, depending on the amount of impedance standards that are available to the user. A calibration method that has the minimum mathematical effort is presented in [1] and has also been tested in this work. Seven well determined impedance standards are needed, in the following way: five standards all around the edge of the Smith chart (magnitude of the reflection coefficient equal to 1), one matched load (magnitude of reflection coefficient equal to 0) and one load located inside the Smith chart (magnitude of reflection coefficient between 0 and 1). This distribution of the calibration standards along the Smith chart is presented in Fig. 5.6.
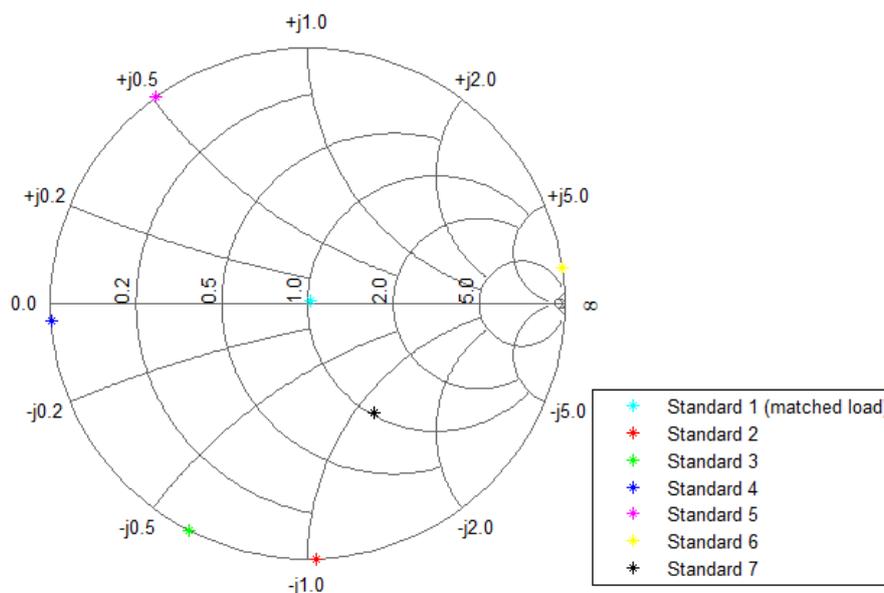
Fig. 5.2 - Example of the distribution of the 7 well known standards required for the proposed six port calibration method published in [2].

During the calibration procedure, 11 calibration coefficients need to be determined, such as presented by the equations below.

With the seven well defined standards, one can make a linear system of seven equations for both the real and imaginary parts of the reflection coefficients associated with these seven standards.

$$A = \frac{R_6 * \Lambda_{63} + R_5 * \Lambda_{53} + R_4 * \Lambda_{43} + R_3}{D_6 * \Lambda_{63} + D_5 * \Lambda_{53} + D_4 * \Lambda_{43} + 1} \qquad (5.5)$$

$$B = \frac{I_6 * \Lambda_{63} + I_5 * \Lambda_{53} + I_4 * \Lambda_{43} + I_3}{D_6 * \Lambda_{63} + D_5 * \Lambda_{53} + D_4 * \Lambda_{43} + 1} \qquad (5.6)$$

$$\Lambda_{ij} = \frac{P_i}{P_j} \qquad (5.7)$$

In Eq. 5.5-5.7 A and B are the real and imaginary parts of the well defined standards used in the calibration process, P_k is the power coupled by detector "k" and R_3-R_6, I_3-I_6, D_4-D_6 are the coefficients to be determined. A derivation of these equations can be found in [2].

After the linear system is solved, all the 11 coefficients are known (R_3-R_6, I_3-I_6, D_4-D_6), and the system is ready to determine the reflection coefficient of any other load connected to port 2.

The additional important thing regarding this calibration technique is that the mismatch at the detector ports does not represent a problem anymore, as long as the mismatch remains constant during the whole operation of the six port reflectometer.

The seven standards method represents an attractive way of calibrating the six port reflectometer because of its mathematical simplicity. However, sometimes it might be difficult to find seven well defined impedance standards to use during the calibration procedure. Also, using such a big number of standards can increase the chance of introducing errors into the calculations. This is why in general, practical six port reflectometer designs are mostly calibrated using a method that requires the minimum amount of precisely defined standards. Such a method, using three well known standards, is described in the next section.

5.2.3   Using an initial calibration step with three standards

Even if the previous calibration technique returns good results and does not depend on the detector's input matching, the problem represents the need for seven well known standards that have to be used. Another popular method to calibrate the six port reflectometer requires only three well defined standards, a short, an open, and a matched load. This method is described in [2]. It consists of two different steps. During the first stage, nine independent loads covering the whole Smith chart are presented to the test port, and all the four power responses at the detection ports are measured and saved. The difference compared to the previously presented calibration algorithm is that the nine loads don't need to be well defined and not even necessarily known to the user. The four power values detected at each of these nine measurements are used to form a nonlinear system of equations that will provide solutions

representing the calibration coefficients. As the procedure is not as straightforward as in the case of the previous calibration method and different published sources introduce partially different notations, it will be explained in more detail in the next lines.

The goal of the first step is to determine the value of the complex reflection coefficient in a plane which is known in literature as the W plane [2]. The calculation of this complex Γ_L in the W plane can be done by initially determining five calibration parameters, named p, q, r, A_5 and A_6. These parameters are related to the four powers collected at the detection ports by Eq. 5.8.

$$p * p_4^2 + q * A_5^2 * p_5^2 + r * A_6^2 * p_6^2 + (r - p - q) * A_5^2 * p_4 * p_5 + (q - p - r) * A_6^2 * p_4 * p_6 + (p - q - r) * A_5^2 * A_6^2 * p_5 * p_6 + p * (p - q - r) * p_4 + q * (p - p - r) * A_5^2 * p_5 + r * (r - p - q) * A_6^2 * p_6 + p * q * r = 0 , \quad (5.8)$$

where $p_4 = P_4/P_3$, $p_5 = P_5/P_3$, $p_6 = P_6/P_3$, and P_3, P_4, P_5, P_6 are the four power ratiosas collected fromthe power detectors.

By dividing all the terms in the above equation with the product p*q*r, the simplified equation 5.9 is obtained.

$$x_1 * p_4^2 + x_2 * p_5^2 + x_3 * p_6^2 + x_4 * p_4 * p_5 + x_5 * p_5 * p_6 + x_6 * p_4 * p_6 + x_7 * p_4 + x_8 * p_5 + x_9 * p_6 + 1 = 0 , \quad (5.9)$$

Where the p_k terms have the same meaning as the ones explained in Eq. 5.8.

In this equation the nine "x" coefficients are defined after the above described division as presented in Eq. 5.10-5.18.

$$x_1 = \frac{1}{q*r} \quad\quad\quad (5.10)$$

$$x_2 = \frac{A_5^4}{p*r} \quad\quad\quad (5.11)$$

$$x_3 = \frac{A_6^4}{p*q} \quad\quad\quad (5.12)$$

$$x_4 = (r - p - q) * \frac{A_6^2}{p*q*r} \quad\quad\quad (5.13)$$

$$x_5 = (q - p - r) * \frac{A_6^2}{p*q*r} \quad\quad\quad (5.14)$$

$$x_6 = (p - q - r) * \frac{A_5^2 A_6^2}{p*q*r} \quad\quad\quad (5.15)$$

$$x_7 = \frac{p - q - r}{q*r} \quad\quad\quad (5.16)$$

$$x_8 = \frac{(r - p - q) * A_5^2}{p*r} \quad\quad\quad (5.17)$$

$$x_9 = \frac{(r - p - q) * A_6^2}{p*q} \quad\quad\quad (5.18)$$

Observing Eq. 5.9, it can be seen that the nine unknown "x" coefficients can be determined as the solution of a linear system of nine equations. This system is formed by taking

the required power ratios resulted by using nine not necessarily known standards at the output port (port 2) of the six port reflectometer. After the "x" terms were determined, a nonlinear system of equations can be formed using equations 5.10-5.18 in order to calculate the five required W plane parameters p, q, r, A_5, A_6. It is easier to define a first estimate solution from which the iterative process of calculating the solution to the non linear system will be started. This first estimate can be calculated from the determined "x" coefficients as presented in Eq. 5.19-5.23:

$$r = \frac{2*x_5 - x_7*x_9}{2*x_1*x_9 - x_5*x_7} \tag{5.19}$$

$$q = \frac{2*x_4 - x_7*x_8}{2*x_1*x_8 - x_4*x_7} \tag{5.20}$$

$$p = \frac{2*x_5 - x_7*x_9}{2*x_1*x_9 - x_5*x_7} + \frac{2*x_4 - x_7*x_8}{2*x_1*x_8 - x_4*x_7} + \frac{x_7}{x_1} \tag{5.21}$$

$$A_5 = \left(x_2 * \left(\frac{2*x_5 - x_7*x_9}{2*x_1*x_9 - x_5*x_7} + \frac{2*x_4 - x_7*x_8}{2*x_1*x_8 - x_4*x_7} + \frac{x_7}{x_1}\right) * \left(\frac{2*x_5 - x_7*x_9}{2*x_1*x_9 - x_5*x_7}\right)\right)^{\frac{1}{4}}$$

$$\tag{5.22}$$

$$A_6 = \left(x_3 * \left(\frac{2*x_5 - x_7*x_9}{2*x_1*x_9 - x_5*x_7} + \frac{2*x_4 - x_7*x_8}{2*x_1*x_8 - x_4*x_7} + \frac{x_7}{x_1}\right) * \left(\frac{2*x_4 - x_7*x_8}{2*x_1*x_8 - x_4*x_7}\right)\right)^{\frac{1}{4}}$$

$$\tag{5.23}$$

With the initial estimate and the nonlinear system, the five W plane parameters can be determined. After this step has been performed, the complex reflection coefficient placed in the W plane can be calculated as:

$$W = (p_4 - A_5^2 * p_5 + r)\frac{1}{2*\sqrt{r}} + j * \frac{[r*(p+q-r)+(p-q+r)*p_4-(p-q-r)*A_5^2*p_5 - 2*r*A_6^2*p_6]}{\pm 2*\sqrt{r*(2*p*q + 2*q*r + 2*p*r - p^2 - q^2 - r^2)}} \tag{5.24}$$

It can be seen that a small ambiguity regarding the sign of the imaginary part of the reflection coefficient is present. This ambiguity can be further eliminated by measuring a (partly) known complex impedance.

The part described above represents the six to four port reduction, as it is known in literature. After this step has been completed, the determined value of the reflection coefficient has to be placed back in the Γ_L plane, so a short-open-load correction is performed.

This method corrects any port mismatch and gives 100% accurate results if the reflection coefficient at the respective port remains constant during the whole measurement and does not have a variation with different loads applied at port 2. Due to the less number of accurate standards required, this calibration algorithm is preferable, despite its larger computational effort.

This chapter presented several ways in which both the directional coupler and the six port reflectometer can be used. These algorithms vary in complexity and the choice of the most suitable one to use depends strongly on the application. During the time spent on this thesis project, all the above illustrated methods were tested. Some of them were also tested using real measured data, the results being available in Chapter 7.

However, before being able to use these calibration algorithms, one needs to collect in an accurate way the voltages present at the detection ports. The approach that was taken in this work was the use of diode based power detectors, for reasons such as cost, area, and low complexity. The next chapter is dedicated to their design, various tested implementations, linearization procedures and measured results.

References

[1] D. Woods, "Analysis and Calibration Theory of the General Six Port Reflectometer Emplying 4 Amplitude Detectors", Proc. IEE, vol 126, no. 2, February 1979.

[2] G. F. Engen, "Calibrating the Six-Port Reflectometer by Means of Sliding Terminations", IEEE Transactions on Microwave Theory and Techniques, vol. MTT-26, no. 12, December 1978.

6.Power detector design

6.1 The need to use detectors

Chapters 3 and 4 were dedicated to the analysis of two individual ways of measuring the reflection coefficient at the output port of a power amplifier. These methods involve the use of a bondwire based directional coupler, as described in Chapter 3, or a bondwire based six port reflectometer, as described in Chapter 4. No matter which of these two methods is chosen, one still needs to read the voltages coupled at the detection ports, in order to use them later in the calculations. It was concluded in Chapter 2 of this thesis that an approach which uses only the magnitudes of the coupled voltages as inputs is preferable in comparison with both magnitude and phase detection. This is because magnitude detection methods are easier to implement in practice, they have a lower area requirement, and they are less dangerous to introduce spectral noise/interferes in the system (e.g. LO leakage through the mixers).

Because with a simple directional coupler with magnitude detectors only the magnitude of the reflection coefficient can be calculated, Chapter 4 of this thesis proposed the design of a six port reflectometer as a cheap, compact way to obtain Γ_L in its complex form. The six port reflectometer requires only the magnitude of the powers coupled at its four detection ports to calculate the complex reflection coefficient. These powers are later used in one of the six port calibration algorithms presented in Chapter 5 in order to make the six port reflectometer able to measure any complex reflection coefficient at the output port. Even if in simulators like Agilent ADS this procedure is straightforward, in practice it is difficult to obtain the high frequency powers present at the four detection points. For this, one would need external power meters coupled to the detection ports (ports 3-6) in order to read the required powers. Considering the fact that this project is designed for package integration purposes, this possibility is not any more valid, and another way to sense the high frequency power in a more compact way has to be used. Diode based power detectors have been used for those kinds of purposes for a long time and vast literature exists regarding the subject [1] – [4]. Even though the accuracy provided by a simple and compact diode detector can never be identical with the one provided by a standalone power meter, these detectors can be successfully used in applications where a small percentage of error can be tolerated or does not introduce a significant error in the overall measurement and algorithm procedure.

A diode detector is a circuit consisting of a diode and some additional passive components. The most popular diodes used for these kinds of applications are the Schottky diodes, even though point contact diodes were used for similar goals in the past [6]. The typical diode detector circuit is depicted in Fig. 6.1.
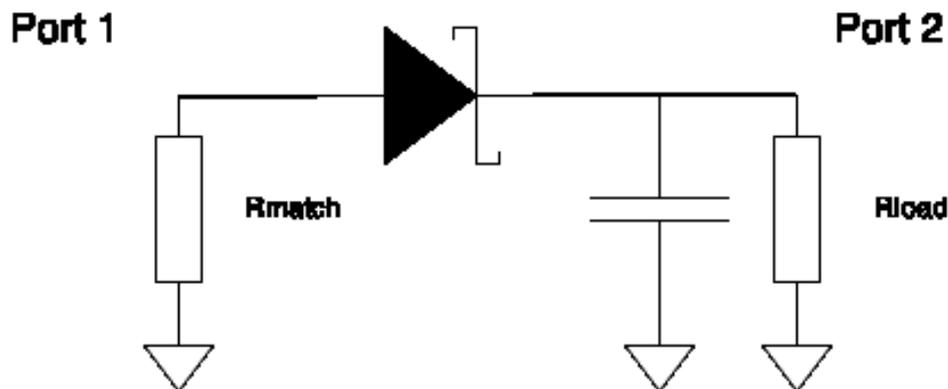
Fig. 6.1 - Basic diode power detector circuit.

RF power is applied at port 1 of the circuit, and the diode is converting this power into a DC voltage which can be read at port 2. An extra capacitor used to filter the higher order harmonics at port 2 is used. Also, there is usually a matching resistor placed at the input of the circuit, as presented in Fig. 1. This resistor matches the input of the diode detector to the impedance of the RF power generator (usually 50 Ω), such that the return loss of the detector is reduced to a minimum. Using the DC voltage extracted from port 2 is more convenient than using the high frequency power from port 1. The DC voltage can then be routed out of the package and read by a readout system, or applied to an ADC for further processing.

In order to determine the RF power present at the input of the diode, a relation between DC voltage and RF input power has to exist. Ideally, the easiest relation is a linear variation of the DC voltage with the input RF power. However, the output of a Schottky diode with respect to the input power is presented in Fig. 6.2.
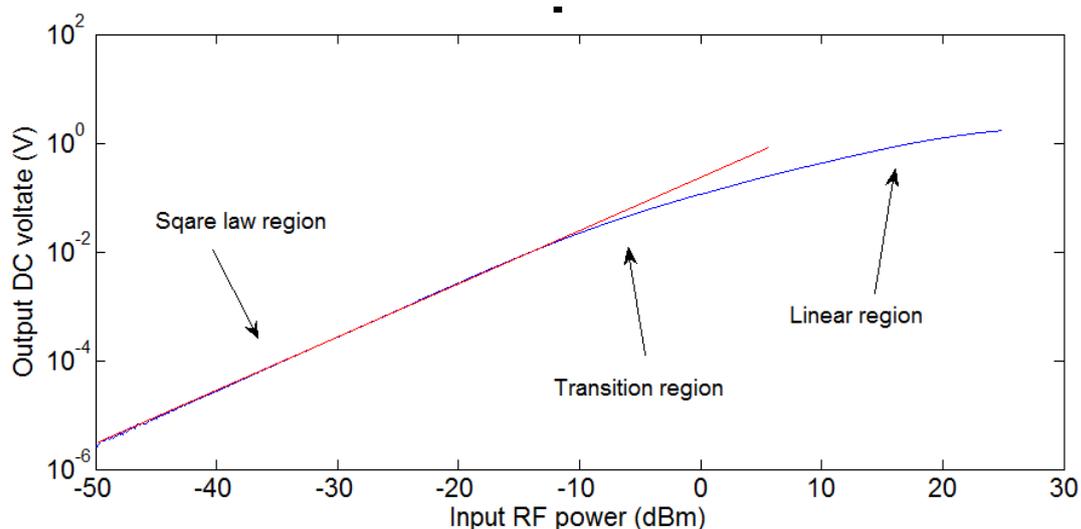
Fig. 6.2 - Usual Schottky diode output voltage vs. input power plot representing the three different operating regimes.

It can be seen that for very low input power levels (usually below -20 dBm) the output voltage varies linearly with the RF power. This is the square law region. After a certain level of

power at the input, the DC output starts to deviate from the square law relation. There is the transition region, usually between -20 and 10 dBm input, followed by the linear region, at high power levels, in which the input power is proportional to the square of the DC output voltage. Most of the diode detector examples presented in literature take advantage of the square law region. This is because it is the simplest one to use, with almost no extra mathematical processing which needs to be applied to the DC voltage in order to get the input power. Some papers are describing ways to take into account the deviation from the square law regime and minimize this variation by a linearization initial step [5] [6]. However, focusing on only one variation regime for the diodes seriously diminishes the dynamic range over which the diode can still sense and give meaningful information about the power level at the input. Moreover, since this project is designed for use in high power transistors, the power coupled into the detector ports will not be always so low such that the diodes can work comfortably in the linear regime. Finally, very low power levels (for example below -30 dBm) will also result in very low voltages generated by the diode (in the order of μV). This means extra demands for the read out circuit with respect to its noise floor. For all these reasons, a high dynamic range linear diode was aimed in the design. Because making the linearization for a large input dynamic range is not as comfortable as making it for a smaller one, special attention has to be paid in calculating the coefficients of the polynomial function which will represent the relation between the DC voltage and the input power.

6.2   Requirements for the detectors

The set of requirements used for designing the diode detectors was demanding, due to the nature of the application. First, since package integration of the whole system was targeted from the beginning, a compact detector was not only desirable, but also necessary. The second most important requirement was that the return loss of the detectors is small, and also independent of the power applied at the input of the diode. This means that the input impedance of the diode detector should be set as close as possible to 50 Ω (the source impedance) and also kept very constant at any input power level. The reason why the input impedance of the diode detector should not vary with power is that the six port calibration algorithm assumes a perfectly linear network. If the input impedance of the detectors varies, then the power coupled into the ports does not vary linearly with the power injected at port 1, which makes the initial diode linearization step not possible anymore. In particular for this application, we need a large dynamic range for the diode detectors. They should be able to give relevant information about input powers ranging from very low levels, up to the maximum level that can be applied at the input without damaging the diode. This requirement comes with additional conditions for the detectors with respect to maximum power handling, and minimum output voltage that can be detected by the readout system. Finally, the accuracy of the linearization step has to be good in

order to use the DC information returned by the diode. Because in the described six port calibration algorithm an error of -22 dB in the used power leads to less than -30 dB error in the calculated Γ_L, this -22 dB maximum error has been chosen as the accuracy specification of the linearization step over the whole dynamic range.

6.3   Linearization algorithm

Most of the diode linearization algorithms presented in literature are aiming to minimize the deviation from the square law regime. These techniques are very efficient if one is aiming for sensing low power levels. Also, since at low power levels the diode has a mostly linear relation between output voltage and input power, the user can even choose to do no linearization at all, the error being still in a reasonable low magnitude if the voltage readout system can handle low voltage values. At higher input power levels the output voltage starts to deviate from the square law regime and the relation between input power and output voltage can be modelled using the following exponential equation.

$$P_{RF} = k * V_{DC}^{\sum_1^n X_i * V_{DC}^i},\qquad (6.1)$$

where n is the order of the polynomial representing the exponent of the DC voltage and k is a constant.

Depending on the order n, a better accuracy in the detected power can be achieved. As suggested in previous works, for the region around the square law regime, a polynomial of the 10th order is good enough to obtain good results [7]. For higher levels of the input power however (the transition region), more terms in the polynomial function are required to keep the same accuracy level. Finally, when the output voltage enters the linear region, again the order of the polynomial function can be relaxed. In this work the order of the polynomial function was set to a constant value of 10 for the whole dynamic range of the input RF power. This is because at low power levels the noise of the readout system represents a considerable amount of the read voltage, and a lower order polynomial would have been not able to accurately linearize the DC voltage within the specified accuracy. Also, at high power levels the magnitude of the DC voltage at port 2 of the diode reaches significant levels even over 1.5 V in some cases depending on the diode. Then, a high polynomial order is again beneficial for good accuracy on larger voltages. The order can still be lowered in this region with the condition to take more sample points in the linearization process. The first option was chosen because making more very accurate sample measurements for the linearization process can be more demanding than using only mathematical ways to improve the accuracy. As specified, lower order linearizations are also possible, and an additional example presenting the accuracy results for a 5th order polynomial is plotted at the end of this chapter.

The basic linearization algorithm starts from the relation including the DC output voltage and RF input power. By taking the logarithm of both sides, one is able to form a linear system of equations of the form presented in Eq. 6.2 – 6.4.

$$\frac{\log(P_{RF1})}{\log(V_{DC1})} = x_0 + x_1 * V_{DC1} + x_2 * V_{DC1}{}^2 + \cdots + x_n * V_{DC1}{}^n + \frac{1}{\log(V_{DC1})} + k \quad (6.2)$$

$$\frac{\log(P_{RF2})}{\log(V_{DC2})} = x_0 + x_1 * V_{DC2} + x_2 * V_{DC2}{}^2 + \cdots + x_n * V_{DC2}{}^n + \frac{1}{\log(V_{DC2})} + k \quad (6.3)$$

....

$$\frac{\log(P_{RFm})}{\log(V_{DCm})} = x_0 + x_1 * V_{DCm} + x_2 * V_{DCm}{}^2 + \cdots + x_n * V_{DCm}{}^n + \frac{1}{\log(V_{DCm})} + k \quad (6.4)$$

In this system, the unknowns are the constant k, plus the coefficients $x_0...x_n$, depending on the chosen order of the polynomial function, where n represents the order. V_{dc1} and P_{RF1} represent the DC output voltage and the RF input power associated to the first reference point taken in the linearization algorithm. Similarly, V_{dcm} and P_{RFm} represent the DC output voltage and the RF input power of the mth reference point taken in the linearization algorithm, where m is the total number of reference points, m>=n+2. By selecting at least n+2 sample points covering the whole voltage range of interest, one can form a linear system to be solved for the n+2 unknowns. Selecting more sample points results in an over determined system, which gives even better quality solutions.

Mathworks Matlab was used for the linearization procedure. This brought some extra mathematical issues which are not present in the theoretical approach. If the difference between the lowest detected voltage and the highest detected voltage becomes very large, which is the case when using a wide dynamic range, Matlab reports an ill conditioned linear system, and the above described method does not work anymore. Also, very low voltages represent a problem when they are taken to high powers, as it is done in the polynomial function. Normalizing all the voltages with respect to the highest one helps with the condition that during all the following calculations the input voltages are scaled in the same way. By normalizing all the DC voltages with respect to the highest output voltage (the one obtained by applying the largest input power), Eq. 6.2-6.4 become:

$$\frac{\log(P_{RF1})}{\log(V'_{DC1})} = x_0 + x_1 * V'_{DC1} + x_2 * V'_{DC1}{}^2 + \cdots + x_n * V'_{DC1}{}^n + \frac{1}{\log(V'_{DC1})} + k \quad (6.5)$$

$$\frac{\log(P_{RF2})}{\log(V'_{DC2})} = x_0 + x_1 * V'_{DC2} + x_2 * V'_{DC2}{}^2 + \cdots + x_n * V'_{DC2}{}^n + \frac{1}{\log(V'_{DC2})} + k \quad (6.6)$$

....

$$\frac{\log(P_{RFm})}{\log(V'_{DCm})} = x_0 + x_1 * V'_{DCm} + x_2 * V'_{DCm}{}^2 + \cdots + x_n * V'_{DCm}{}^n + \frac{1}{\log(V'_{DCm})} + k$$

$$(6.7)$$

In the above equations, V'_{dcm} represents the normalized DC voltage reading of the mth reference point taken for the linearization algorithm, as in $V'_{dcm}=V_{dcm}/V_{dcmax}$, where V_{dcmax}

represents the DC voltage obtained when the largest input RF power is applied to the detector. Considering these new notations, normalized DC voltages were used for the linearization step in the performed calculations.

6.4   Detector implementations

In order to determine the best power detector that matches the previously underlined specifications, three possible implementations were analysed. First, the basic diode detector circuit was tested, as it was presented in Fig. 6.1. The biggest problem that was found for this detector was that its input impedance was dependent on the input power applied at port 1 of the six port reflectometer. At low input power levels the input impedance is close to the desired value of 50 Ω, but this impedance starts to drop at higher input powers.

This would make the linearization procedure and six port calibration impossible because the six port circuit would not be linear anymore. For the second implementation, presented schematically in Fig. 6.3, a fix was found for the input matching problem.
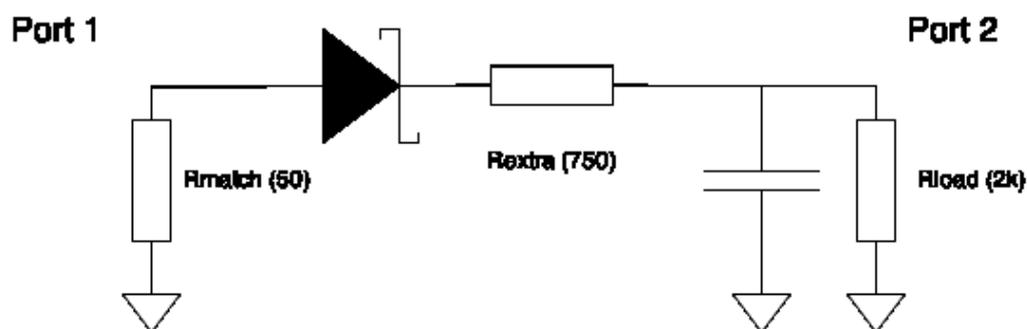
Fig. 6.3 - Modified diode power detector for improved input matching.

An extra resistor placed after the Schottky diode keeps the input impedance a lot more constant with the variation in the input power level. The Schottky diode used was a Skyworks SMS7621-079LF. This diode gives an output voltage smaller than 100 μV when powers below -10 dBm are applied at the input. This led to a problem regarding the low end of the dynamic range, as the detected voltages were comparable to the noise floor of the used readout circuit. In order to measure the performance of the diode detector presented schematically in Fig. 6.3, this detector was used at all the four detection ports of the proposed six port reflectometer circuit earlier described in Chapter 4. The test setup for this measurement is presented in Fig. 6.4.
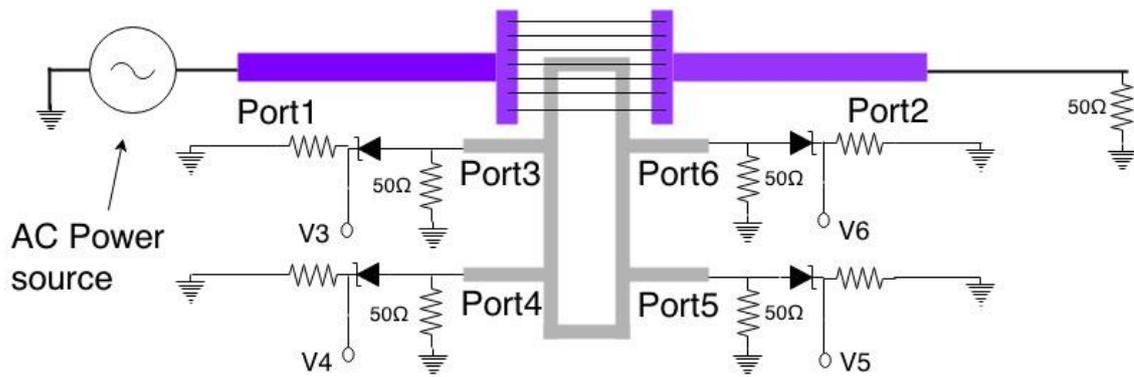
Fig. 6.4 - Measurement setup for testing the behavior of the diode based power detector from Fig. 6.3.

In this experiment, RF power is injected at port 1 of the circuit from Fig. 4 and the power level is swept between 10 and 40 dBm. At port 2, the output port, a matched load was placed and kept constant during the power sweep. Ports 3-6 were equipped with the above presented diode detectors, and the DC voltage of port 3 was read. It is very important to mention that the noise floor of the voltage readout circuit in this experiment was at 100 µV. The diode DC voltage response versus the applied input power at port 1 is presented in Fig. 6.5.
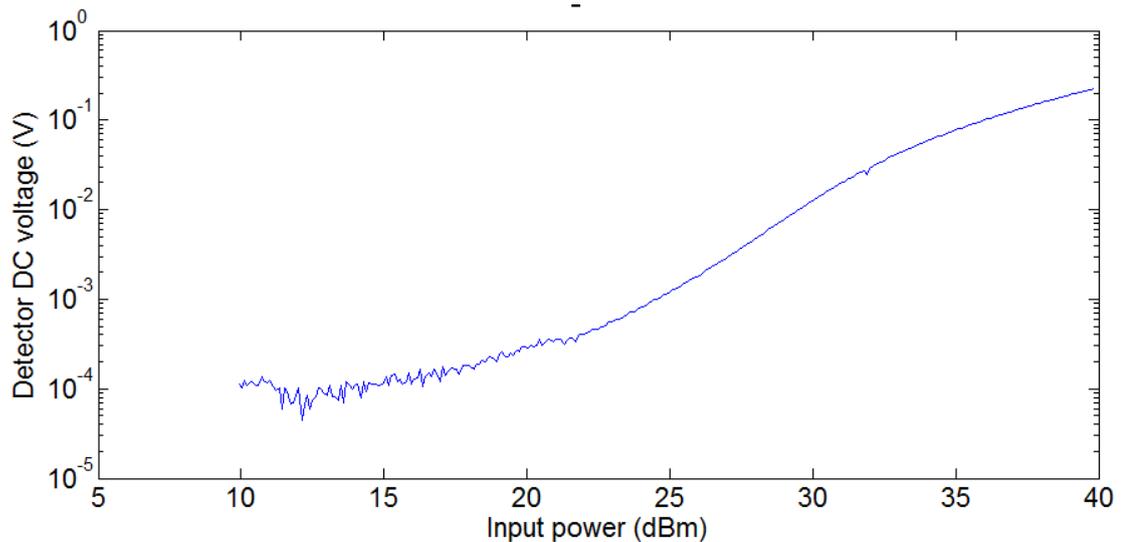
Fig. 6.5 - Response of the diode power detector from Fig. 6.3 for a sweep of 10 to 40 dBm at port 1 of the six-port network in Fig 6.4.

The high end of the dynamic range is set by the heating handling capabilities of the input matching resistor in the diode detector. Typical SMD 0805 resistors have a specification of 0.1 W, which means that they can be used up to 15 dBm input power without the risk of having a significant change in the value of their resistance. Considering that the proposed six port network has a coupling of -25 dB between the main line (the bondwire array) and the highest coupling detection port (port 3 in Fig. 4), 40 dBm of maximum input power were applied at port 1. As it can be seen from the above plot, the useful dynamic range of the analysed detector (higher than the noise floor of the readout circuit) lies between 10 and 40 dBm power at port 1. By removing the voltage range over which noise has a significant impact,

because of the readout circuit's noise floor, we are dropping an extra 14 dB, remaining with 16 dB of effective dynamic range. After a linearization step has been performed using the collected raw DC voltage presented in Fig. 5, the calculated linear power versus the actual power applied at port 1 in Fig. 6.4 is presented in Fig. 6.6.
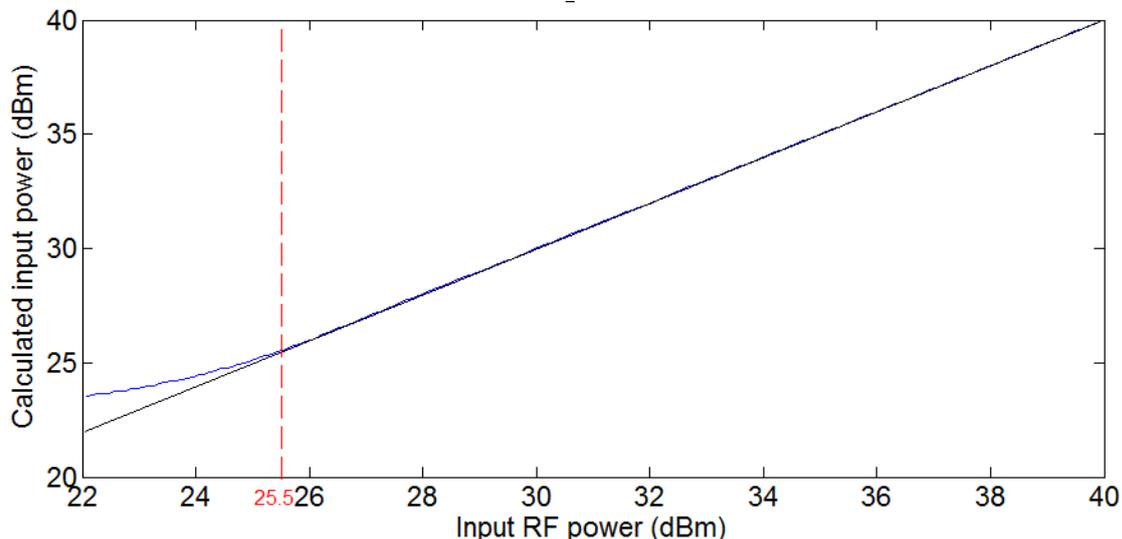
Fig. 6.6 - Linearization result for the raw measured data presented in Fig. 6.5.

After the linearization step, the calculated input power should be equal to the actual power that is applied at port 1 of the circuit in Fig 6.4. From Fig. 6.6 it can be seen that the analyzed diode detector can be linearized over an input dynamic range of 14.5 dB.

Because of the low dynamic range obtained using the second detector, a further analysis was performed in order to increase its performance. The noise limited diodes were replaced with Skyworks SMS7630-079LF, a Schottky diode capable of giving up to eight times larger voltage for the same power applied at the input. This can be explained by the fact that the saturation current of this diode Is, has a larger value than the saturation current of the Skyworks SMS7621-079LF diode (5 µA compared to 40 nA).

A different input matching technique was also used. A resistive divider of 49 Ω and 1 Ω was placed in front of the diode, such that a small fraction of the input power actually reaches the diode (Fig. 6.7).
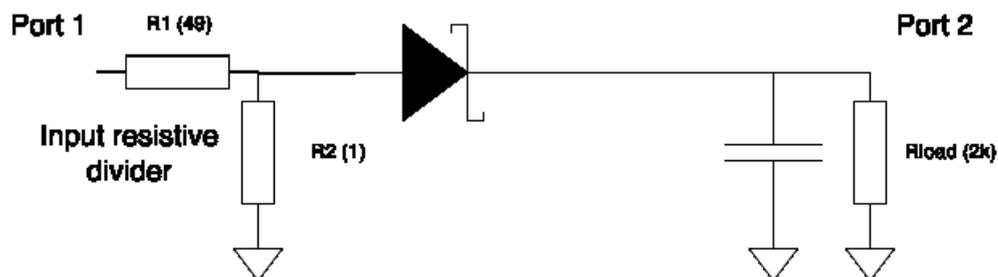
Fig. 6.7 - Improved diode power detector with input power divider implementation.

This approach also made the input matching constant with power level, as presented in Figs. 6.8-6.10.

Fig. 6.8 - Return loss of the improved diode power detector when a 0 dbm power level is applied at its input.
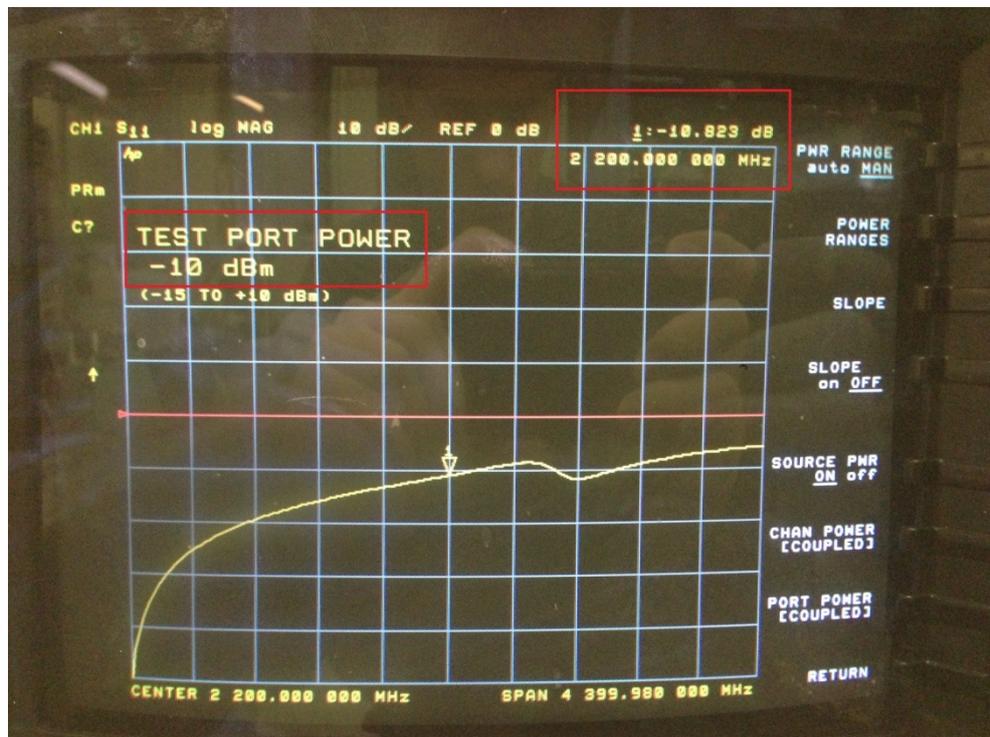
Fig. 6.9 - Return loss of the improved diode power detector when a -10 dbm power level is applied at its input.
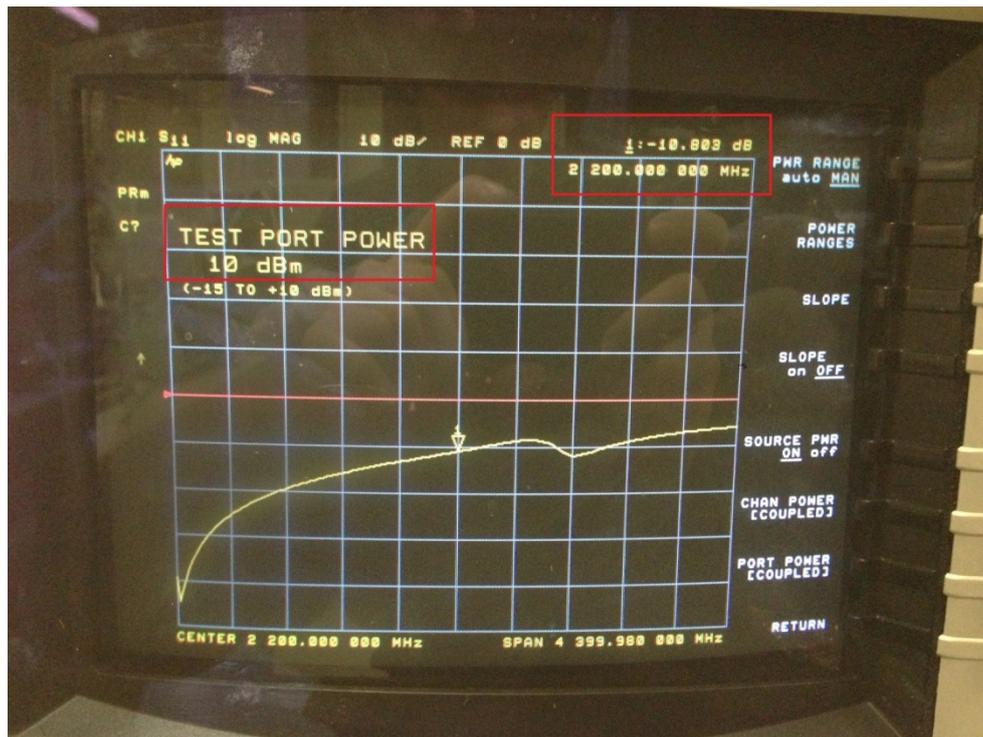
Fig. 6.10 - Return loss of the improved diode power detector when a 10 dbm power level is applied at its input.

From these figures one can also see the value of the return loss of this detector, is below-10 dB at the centre frequency of 2.2 GHz.

A similar test experiment like in the case of the second proposed detector was made for the third one as well. All the test conditions were identical, such as the impedance placed at port 2, and the readout circuit for reading the detected DC voltages. The difference was the range of RF input power applied at port 1, which was this time between -20 and 40 dBm.

Considering the limitations due to readout circuit noise and input resistor heating, now the range of powers that can be safely applied at port 1 of the six port network is between -5 and 40 dBm, 15 dB higher than the previous detector, as it can be seen in Fig. 6.11.
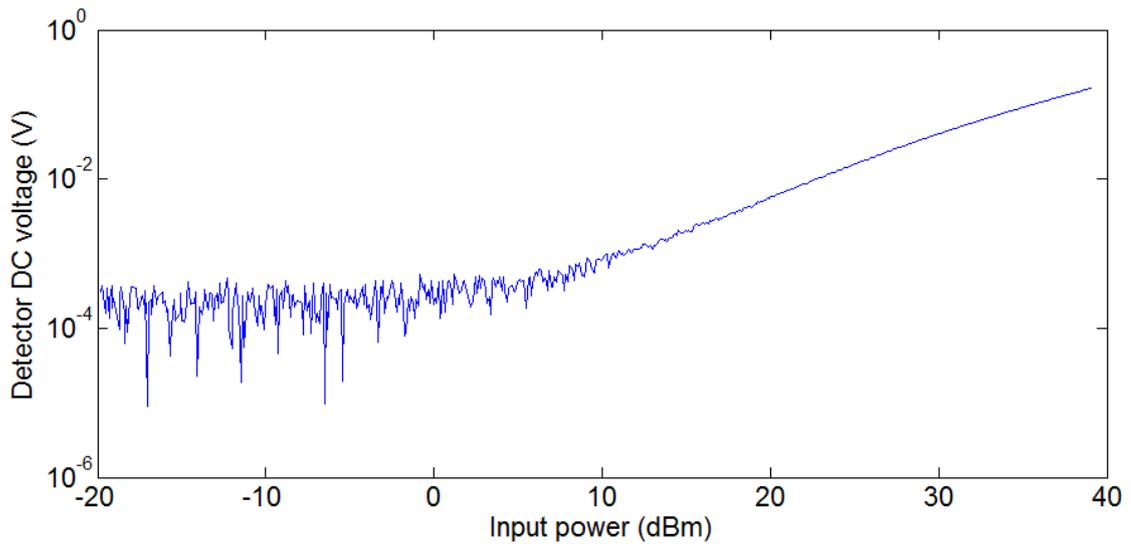
**Fig. 6.11 - Response of the diode power detector from Fig. 6.7 for a sweep of -20 to 40 dBm at port 1 of the six-port network in Fig 6.4.**

However, the visible noise influence on the low voltage levels (close to 100 µV) will limit the range of linearized voltages after the linearization step. This plot of linearized input power versus applied input power is presented in Fig. 6.12.
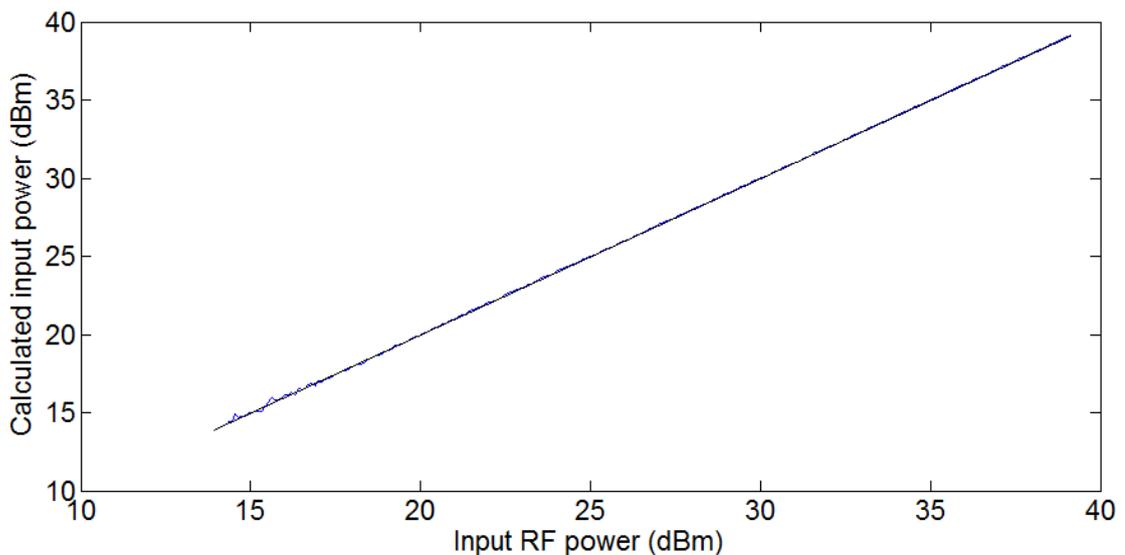
Fig. 6.12 - Linearization result for the raw data presented in Fig. 6.11.

It can be seen that the obtained linear dynamic range is 25 dB for this detector. Compared to the performance of the previous detector, illustrated in Fig. 6.6, a more than 10 dB increase in the dynamic range can be observed.

If RF power is applied directly at the input of the detector and a better readout circuit is used, one can test the linearization procedure over a larger dynamic range. A voltage linearization targeting a 75 dB dynamic range has been performed using the above described diode detector. Plots presenting the linearization curve, as well as the relative linearization error are presented in Figs. 6.13 and 6.14. It can be seen that the detector achieves the desired 75 dB of dynamic range, with an error lower than -20 dBFS, and with an rms value of -37 dBFS. For

determining the linearization coefficients, 50 out of the total of 770 measured voltage points were used.
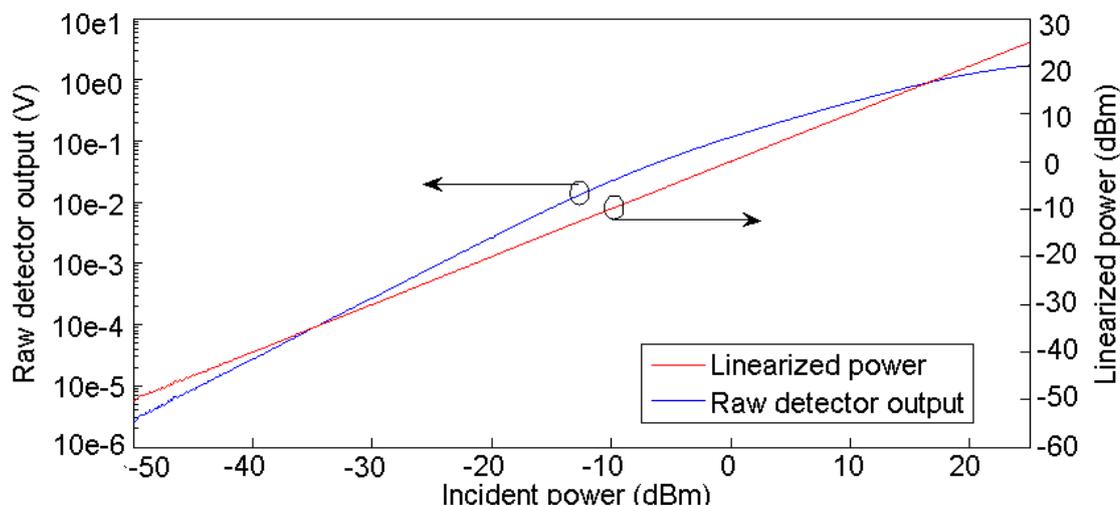
Fig. 6.13 - Linearization curve for the third analysed detector (red) and raw DC voltage (blue) vs. input power.

For each input power level, the linearization error (in dB) is plotted in Fig. 14.
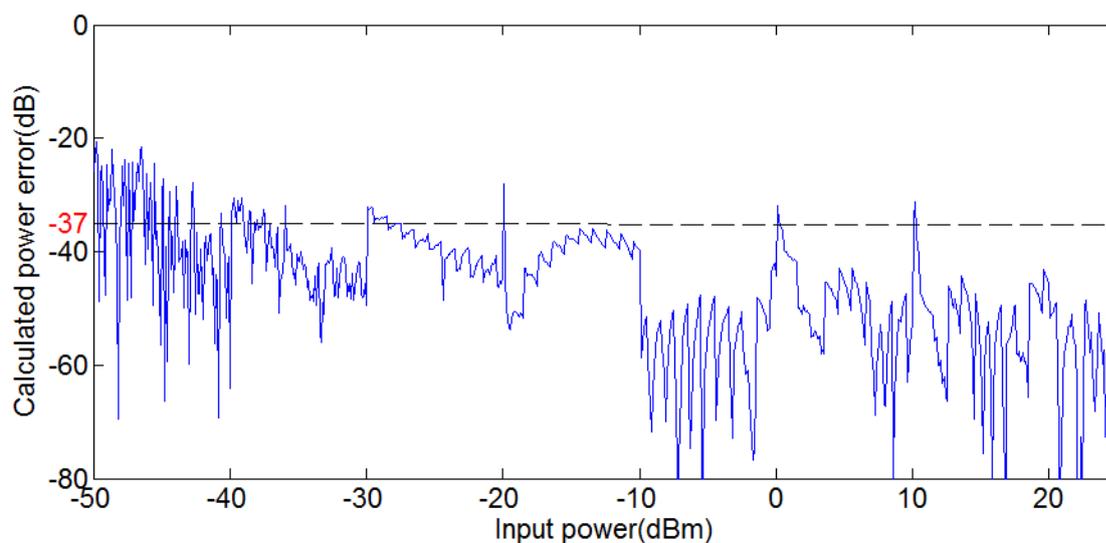
Fig. 6.14 - Error of the calculated power (in dB) as a function of the reference input power.

There are some spikes present once at the start of every power decade, which are the result of a slow settling of the power source and should be ignored in the final result.

It was specified earlier in this chapter that an accuracy of -22 dB in the linearized voltage is good enough to obtain less than -30 dB error in the determined Γ_L. The amount of error present in the end result depends on the computational effort that one puts in the linearization algorithm. It can be seen in Fig. 6.14 that a linearization algorithm using 50 reference points and a 10th order polynomial function results in an error of less than the initial target of -22 dB. However, if one decides to tolerate more error in the final result, the algorithm can be simplified, by using a lower order for the polynomial function, and a lower number of

112

reference points in the linearization procedure. For a practical example, only 30 reference points and a 5th order polynomial were selected for another linearization procedure. The error in the determined power over the whole detector dynamic range is presented in Fig. 6.15.
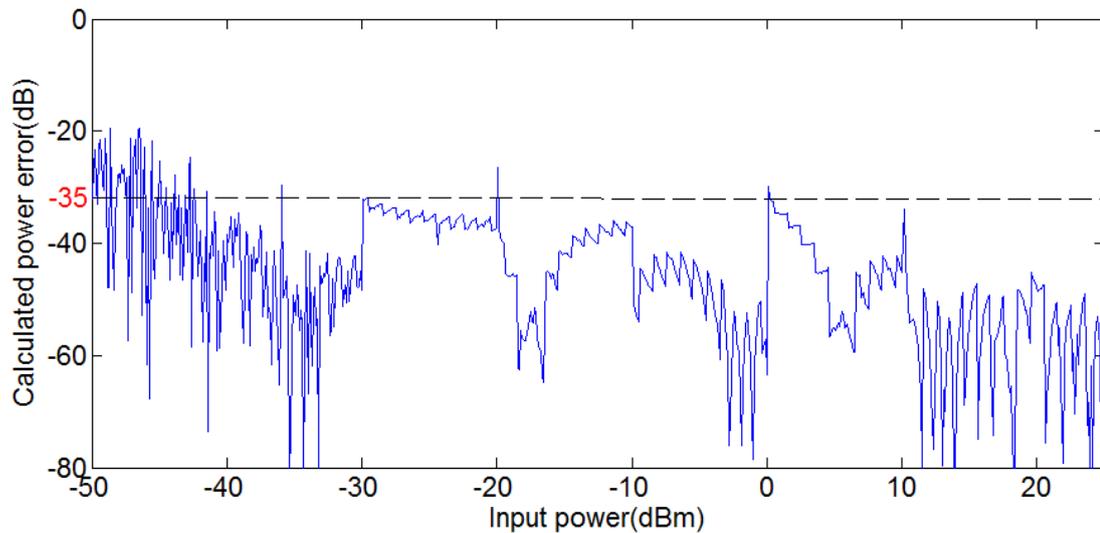
Fig. 6.15 - Error of the calculated power (in dB) as a function of the reference input power using a lower order for the linearization polynomial.

It can now be seen that the error is over -20 dB at lower power levels, but this small degradation could be acceptable if the accuracy demand is not very high and large computational effort for the linearization procedure is not desired. Also, the rms value of the error has degraded, and has now a value of -35 dB.

This chapter presented the steps taken in order to design and test several diode based power detectors. These detectors have the role to calculate the RF power present at their input by only making use of the DC voltages generated at the output. Two particular designs from this chapter (Figs. 6.3 and 6.7) were carefully analysed and measurement results for both of them were presented. In order to test their behaviour in a real measurement application, the detector from Fig. 6.7 was later used in the proposed six port reflectometer design, and the results obtained will be presented in Chapter 7. On the other hand, observing the diode detector just as a standalone component, good performance characteristics (75 dB dynamic range, higher than -10 dB return loss) were obtained using the detector presented in Fig. 6.7. A comparison between this proposed detector and other published power detectors is performed as a conclusion in Table 6.1.

Table 6.1 - Comparison between published power meters and the proposed diode based power meter analysed in this chapter (Fig. 6.7).

Diode Detector	Dynamic range	Considerations
Detector presented in [1]	18 dB	Only covering the square law region
Detector presented in [2]	12 dB	MMIC implementation
Detector presented in [3]	20 dB	MMIC implementation
HP 438A	114 dB	Industrial external power meter
This work	75 dB	Small lumped implementation

It can be seen that the diode detector proposed in Fig. 7 achieves a larger input dynamic range than the other published detectors. Commercially available power meters can go a lot higher in dynamic range, as it is the case of the HP 438A power meter, but they are built as large, external devices. Also, their cost is in the order of hundreds of dollars, while the power meter proposed in this work has a production cost of below 1 $ using commercially available SMD components.

References

[1] E. Bergeault, B. Huyart, G. Geneves, L. Jallet, "Characterisation of diode detectors used in six-port reflectometers", IEEE Transactions on Instrumentation and Measurement, vol. 50 no. 6, December 1991.

[2] J. Bahl, "Broadband power detectors", IEEE Microwave Magazine, June 2007.

[3] W. Jeon, J. Melngailis, "CMOS foundry Schotkky Diode Microwave Power Detector Fabrication, Spice Modelling and Application", SiRF 2006.

[4] T. Guldbrandsen, "Analysis of Diodes Used as Precision Power Detectors Above the Square Law Region", 1990 IEEE.

[5] C.A. Hoer, "Measuring and Minimizing Diode Detector Nonlinearity", IEEE Transactions on Instrumentation and Measurement, vol. IM-25, no. 4, December 1976.

[6] G. Colef, "New In-Situ Calibration of Diode Detectors Used in Six-Port Network Analyzers", IEEE Transactions on Instrumentation and Measurement, vol. 39, no. 1, February 1990.

[7] F. M. Ghannouchi, A. Mohammadi, "The Six-Port Technique, With Microwave and Wireless Applications", p. 84, 2009, Artech House.

7.Measurement results

The previous chapters were extensively dedicated to the theoretical analysis of the way in which all the individual parts constituting the final proposed design were developed. Chapter 3 presented the design of the integrated bondwire based directional coupler. Following that, Chapter 4 presented the most important ideas and concepts behind the design of the integrated six port reflectometer. Finally, Chapter 6 illustrated the effort put in designing and testing compact and very cost effective diode power detectors, to be used as a way to monitor the high frequency power coupled by the detection loop. During all of these chapters, theoretical concepts and software simulation results were presented in support for the affirmations made. Because of the limited time available during this thesis project, in practice it was not possible to physically produce and measure all the different designs that were simulated. This is why based on the simulation results, a few of them were selected to be produced and tested. The basis of this selection was also presented in the above mentioned chapters, and it mostly focuses on the trade-off between performance facts and area limitations for the proposed target design. This chapter will present the most important results obtained after the practical tests that have been made using the produced test boards. The goal of this chapter, as well as the goal of the whole work is to provide a proof of concept for the presented design. However, it is reasonable to believe that other implementations will behave in practice very similar to the results obtained using the software simulators used, as long as the measured data matches closely to the simulations, as it will be presented.

Because this report treated separately the design of the integrated directional coupler and the design of the integrated six port reflectometer, also the results chapter will focus on both of them individually. First, the measured results for the produced bondwire based directional coupler will be presented. Then, more attention will be put on the analysis of the produced six port reflectometer test boards, with the different tests being described and the important results being presented. Finally, this chapter will give an explanation for the obtain results and will present the detection error obtained.

7.1   Directional coupler measurements

Using a directional coupler is one of the most common ways of measuring the reflection coefficient at the output port of a power amplifier, as it was also presented in the literature review in Chapter 3. However, a large external directional coupler would not be a good solution for the presented situation, as the goal is to provide a compact, package integrated way to measure the reflected power coming back from the load. This is why a directional coupler placed inside the package of the transistor has been designed in this work. In order to save as much area as possible, it makes use of the already existing bondwires

connecting the drain of the power bar to the package drain lead. Various simulations regarding the impact of certain factors such as the length, height and shape of the bondwires have been performed and the results were presented in Chapter 3. In the end, test board prototypes were produced, consisting of a bondwire array and a coupled additional structure. The HFSS schematic of one of the produced boards is presented in Fig. 7.1.
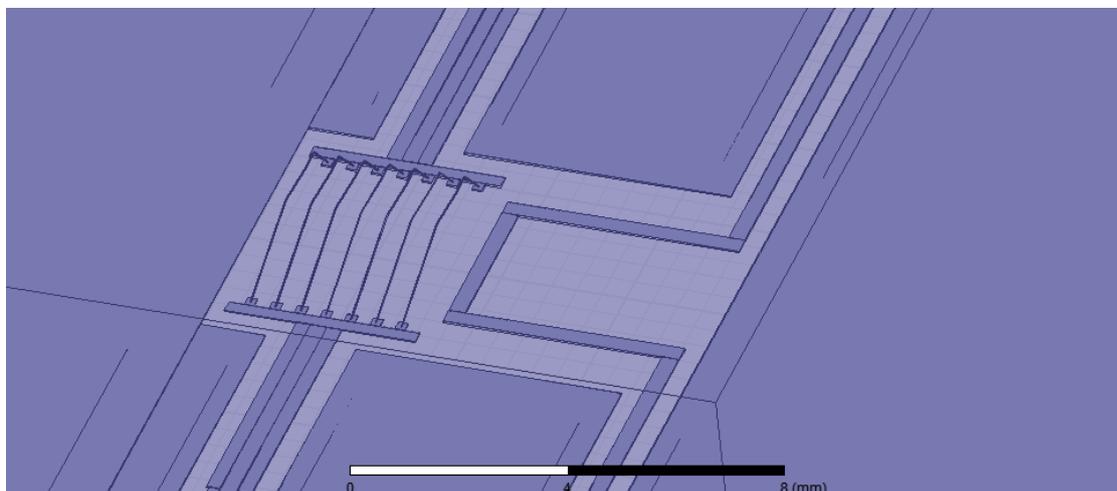
Fig. 7.1 - Example of one of the produced test boards (Ansys HFSS schematic).

The bondwire array in the centre of the board simulates the bondwire array placed inside the transistor's package. The length of the bondwires in this array has been chosen to be 2.5 mm, as this value is easy to obtain in practice and it is a common length for the bondwires placed inside the package.

As it was presented in Chapter 3, three possible versions of the bondwire based directional coupler were analysed:

- a microstrip line placed underneath the bondwire array

- a microstrip line placed next to the bondwire array

- an extra bondwire placed next to the bondwire array

HFSS schematics representing these three different implementations were shown in Chapter 3 and are presented also here in Fig. 7.2, for convenience.
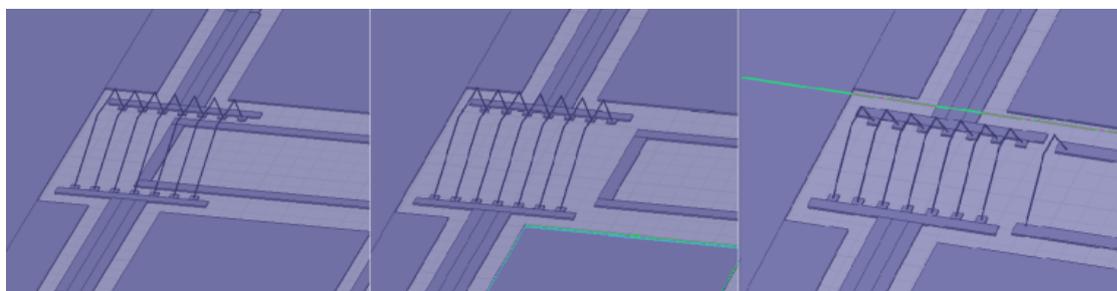
Fig. 7.2 - The threeanalysed implementations for the bondwire based directional coupler. A microstrip line placed underneath the bondwire array (left), a microstrip line placed next to the bondwire array (centre) and an extra bondwire placed next to the bondwire array (right).

The conclusion drawn in the previous discussion about these types of directional couplers was that the design with the coupled line placed next to the bondwires array achieves the best directivity (15 dB) and the lowest coupling (-30 dB) for this particular length of the bondwires in the bondwire array. This is why, in order to test the validity of the performed simulations, this layout has been also physically measured, and its set of S parameters were collected. The test board representing the measured layout is presented in Fig. 7.3. It can be seen the bondwire array in the middle, and also the coupled microstrip line placed to the side of the array. The bondwires have a maximum height of 0.7 mm, like in the HFSS design, and are made of gold. The substrate for this test board is a Rogers 3006 substrate, having the properties presented earlier in Table 3.2.
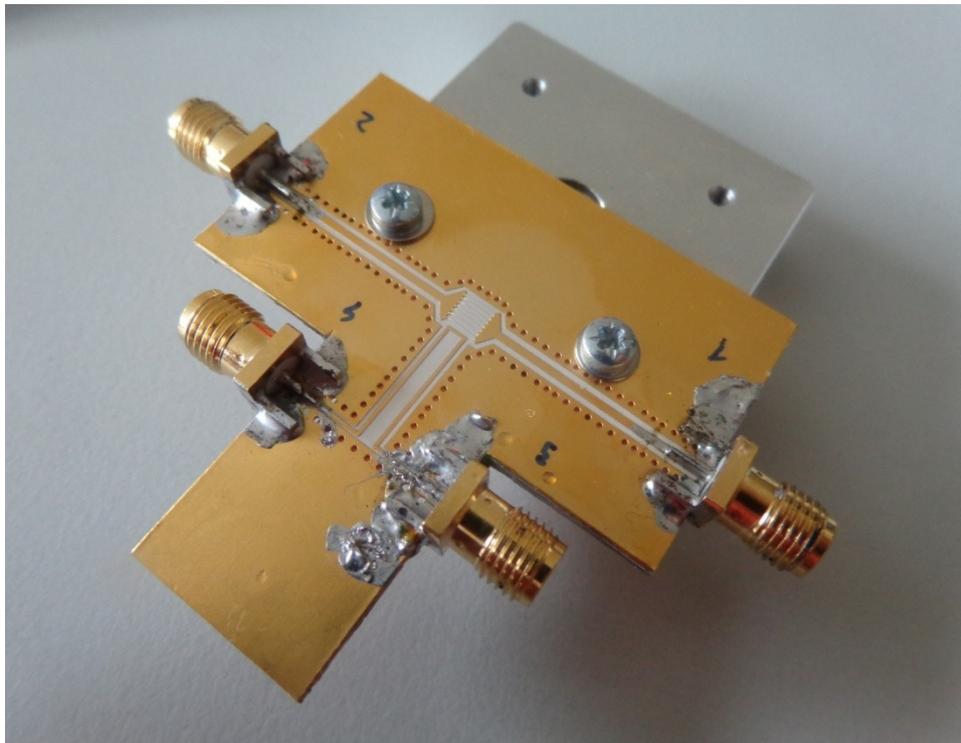
Fig. 7.3 - Produced test board for the bondwire based directional coupler.

In order to measure the S parameters of the board, a network analyser was needed. The simulations were performed with a Hewlett Packard 8753D network analyser, initially calibrated by a short-open-load Rosenberger RPC-3.50 calibration kit. The drawing of the measurement setup is presented in Fig. 7.4. 50 Ω terminations were used at the ports where the network analyser's ports were not connected. In order to get all the desired S parameters, the inputs of the network analyser were connected consecutively to a different pair of ports on the test board, such that in the end the transfer between any two ports was measured. This measurement technique assumes that the two ports that are not connected to the network analyser are always terminated by 50 Ω loads. In practice, the common 50 Ω microwave terminations are not perfect, and they present a return loss in the order to -20 dB. This will introduce an error in the determined set of S parameters. This measurement's objective was to

provide an idea about the behaviour of the proposed directional coupler, as the S parameters were not used further in other calculations. For S parameter measurements that require larger precision, published methods can be found in literature [1], which numerically remove some of the measurement errors.
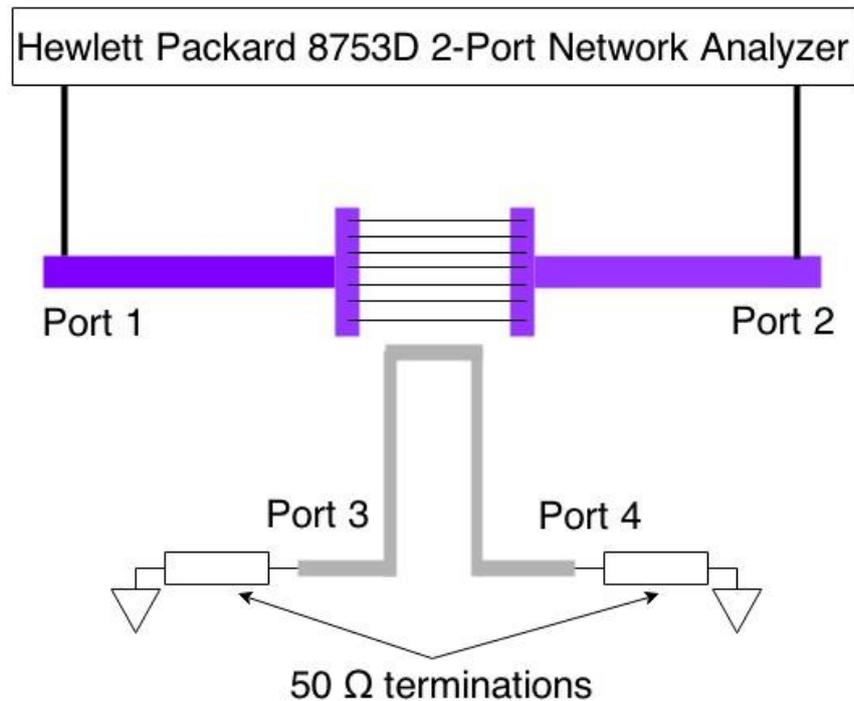
Fig. 7.4 - Test setup for the S parameter measurement in the case of the bondwire directional coupler test board.

The measured S parameters between port 2 and the other ports of the measured test board are presented in Table 7.1. The whole set of measured S parameters for this board is available in the Appendix.

Table 7.1 - Measured S parameters of the bondwire based directional coupler.

S21	S22	S23	S24
0.963/19.53	0.158/-128.32	0.007/6.11	0.036/166.65

In comparison, the results returned by HFSS for an identical layout, for the same selected S parameters are presented in Table 7.2.

Table 7.2 - HFSS simulated S parameters for the bondwire based directional coupler.

S21	S22	S23	S24
0.982/22.885	0.120/-126.87	0.005/7.97	0.030/164.57

In particular from the complete set of measured S parameters, some of them present a certain importance. Ideally S_{21} should be very close to 1 for a coupler that has low losses and

delivers the whole amount of generated power into the load. In this case, S_{21} has a value of -0.73 dB, still close to the ideal 0 dB value. S_{31} and S_{41} are also very important, as they give an indication of the couplers coupling factor and directivity. With the measured values presented in Appendix A.1, the produced layout achieved a coupling factor of -29 dB and a directivity of 14 dB. This section showed that the proposed directional coupler can be produced, and moreover, it achieves good performance characteristics. From this bondwire based directional coupler, together with the design placing the coupled line underneath the bondwire array, the design of the integrated six port reflectometer started. The most important results and conclusions regarding this one are presented in the next section of this chapter.

7.2   Six port reflectometer measurements

As it was stated in the previous section, the design for the integrated six port reflectometer was made as a continuation of the integrated directional coupler. A large range of design possibilities for the directional coupler was analysed in Chapter 3. It was concluded that different design parameters such as the length of the bondwires, their height, and the distance at which the coupled element is placed are all influencing the coupler's characteristics in terms of coupling factor and directivity. In the end, three different implementations were chosen, based on certain constraints, as it was also illustrated at that point. One of the directional coupler's designs (the microstrip line placed next to the bondwire array) has been also measured, the results being presented in the previous section.

A more extensive discussion about the design of the integrated six port reflectometer was carried in Chapter 4 of this work. The reader is advised to go there for information and conclusions regarding the topology of the design, and the way in which certain design parameters, such as the loop's length were chosen. Also Monte Carlo noise and bandwidth analysis are performed there. Similar to the approach taken for the directional coupler, several designs were also created and produced for the six port reflectometer. These designs combine the directional coupler part with the four detection ports needed for the operation of the six port reflectometer. For convenience, the ADS and HFSS layouts of one sample six port design are again presented in Figs. 7.5 and 7.6.
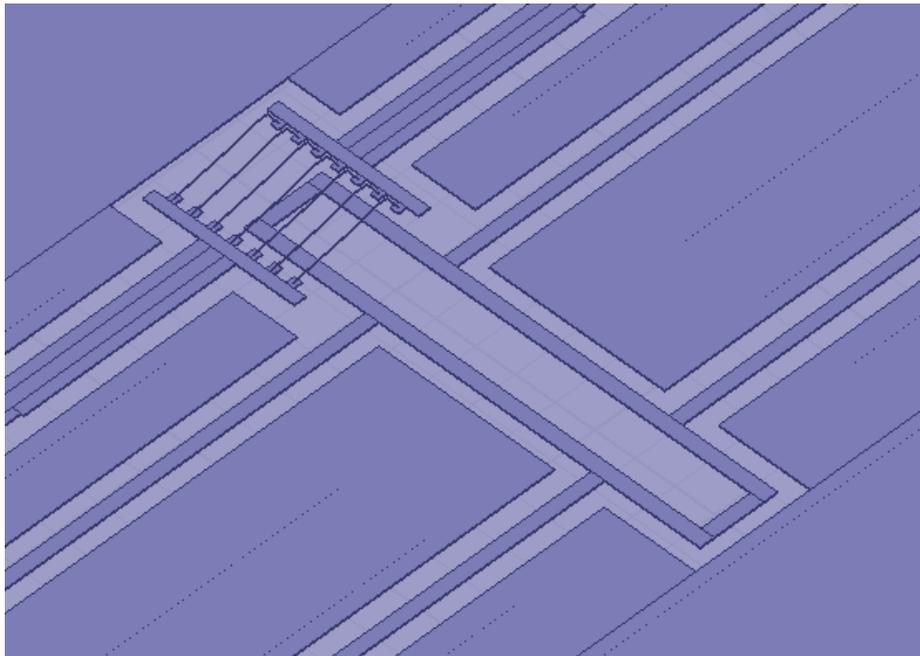
Fig. 7.5 - HFSS layout for the six port reflectometer test board.
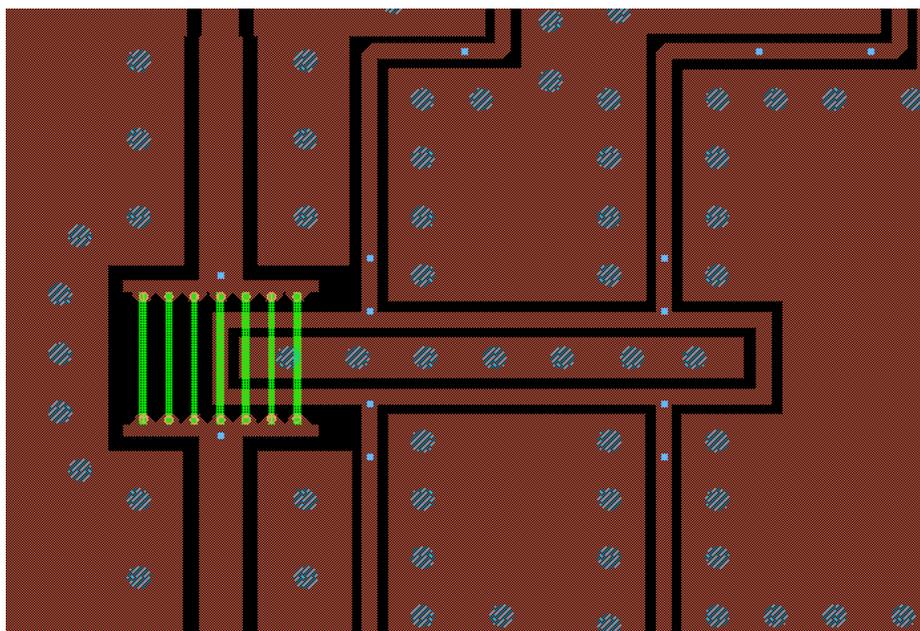
Fig. 7.6 - ADS Momentum layout for the six port reflectometer test board.

The design already presented while analysing the directional coupler can be easily seen here again. The bondwire array in the centre of the board will transfer a certain fraction of its power to the coupled microstrip line placed in this example underneath the array. The difference is that this line will not be measured at its two terminals, like in the case of the directional coupler, but a loop will be created, as presented in the figure. The loop will then be tapped at four different locations, with a distance of $\lambda/8$ between each two consecutive ones. This carefully chosen distance minimizes the effect of noise in the detectors, as it was presented in Chapter 4. The signal power that is read at each of these four points is used as the input of the diode based power detector. These devices were more extensively described in Chapter 6 of

this work. They have the role of converting the RF power that reaches their input into a DC voltage that can be easily read at the output. By means of a diode linearization procedure one can get information about the amount of RF power that was actually present at the tapping position. This power is needed in the six port calibration algorithms, as presented in Chapter 5.

Depending on the calibration algorithm, different measurement approaches have to be taken in the use of the six port reflectometer. The bottom line is however that all of them require the RF power present at the four detection ports. After these powers are available, the user can choose from a range of calibration procedures, depending on the measurement possibilities and of course the amount of precision that the measurement system can deliver. The conclusion of Chapter 5, which was dedicated to these calibration procedures, is that two different approaches can be generally taken in order to use the reflectometer as a mismatch detector. The first choice is the initial measurement of the six port's set of S parameters. Even if this procedure leads to the simplest calibration algorithm, it might not be always desirable. It is easy to measure the S parameters of a test board that is completely exposed at all the 6 ports. However, in a package integrated version, the final goal of this work, not all the ports will be available for measurement. For example, port 1 of the design presented in Fig. 7.5 is actually the drain of the power bar placed inside the package. Therefore, it is not possible to probe it in order to measure the S parameters without de-capping the power transistor. A possible solution to this problem would be to measure one device (or a couple for more reliable results) and then assume that all of them will be reproduced with a very high accuracy, such that further independent measurements will not be required.

If however the user desires a more rigorous method of calibration, without the assumption of reproducibility, there are ways published in literature and presented in Chapter 5 for doing it. This section will start by presenting the measured S parameters of the six port test board. Afterwards, more conventional types of calibration will be also performed, using either seven well known impedance standards applied at the test port, or using nine not necessarily known standards plus a short open load correction.

7.2.1   S parameters measurements

The S parameters of the six port structure can be used a quick way to determine the value of the reflection coefficient at the detection port. In order to do this however, they need to be known either by software simulation of the layout or by performing practical measurements. It was shown during the first section of this chapter that the measured results in the case of the integrated directional coupler matched closely with the ones obtained by performing simulations with softwares such as HFSS. However, it is of course always more reliable to perform a measurement rather than trusting a simulation whenever this is possible. Layouts representing the six port reflectometer specially designed for measuring the S parameters of the

structure were also produced. These layouts do not include the diode detectors used for measuring the RF power at the detection ports. A photo representing such a layout is shown in Fig. 7.7.
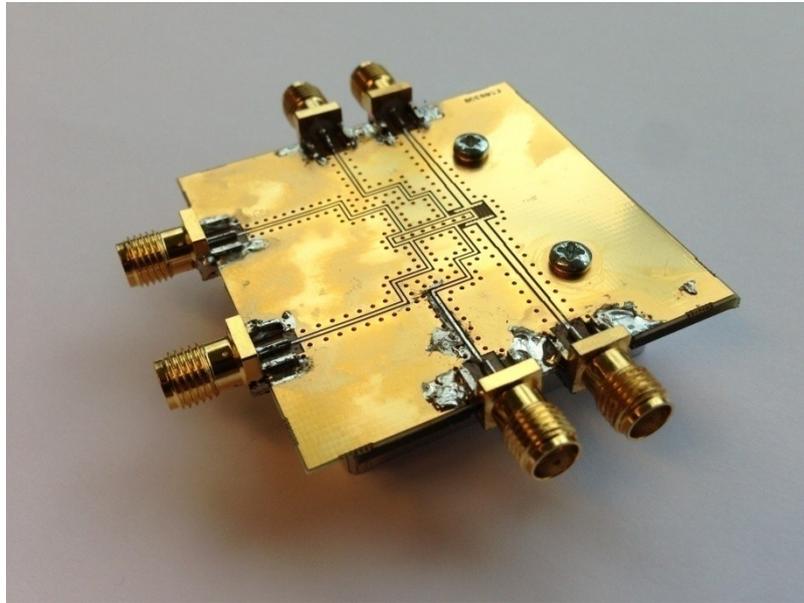
Fig. 7.7 - Physical board for the S parameters measurement in the case of the bondwire based six port reflectometer.

Once the physical prototype has been produced, the S parameters of the six port structure can be measured with the help of a network analyser. The layout chosen for the measurements stage is the one having the coupled side of the loop placed underneath the bondwire array. This layout has been chose for a series of reasons, such as:

- lower influence of the package parasitics on the coupled power, as the coupled side of the loop is placed exactly underneath the bondwire array.

- less area consumed by the whole six port reflectometer structure, as a large part of it (the whole left part of the loop) is placed underneath the array and does not require extra space.

- the implementation with the coupled microstrip line placed to the side of the bondwire array was already measured in the previous section, and this new measurement will expand the range of measured layouts.

The procedure for measuring the six port reflectometer's S parameters was similar to the one described in the case of the bondwire based directional coupler.

After performing measurements at all six ports and gathering all the required data, the measured S parameters can be collected into a 6 by 6 matrix. Table 7.3 presents a selection of measured S parameters between port 2 of the test board and the other ports. Like in the case of the simulated directional coupler, all the measured S parameters are available in the Appendix. Table 7.4 presents the HFSS simulated S parameters for the same terms as the ones in Table 7.3.

Table 7.3 - Measured S parameters for the bondwire based six port reflectometer.

S21	S22	S23	S24	S25	S26
0.965/146.27	0.050/140.63	0.021/136.97	0.017/100.00	0.053/51.84	0.076/19.14

Table 7.4 - HFSS simulated S parameters for the bondwire based six port reflectometer.

S21	S22	S23	S24	S25	S26
0.994/148.03	0.033/105.70	0.016/116.56	0.010/95.71	0.047/62.35	0.055/25.64

As it was shown in Chapter 5, knowing the S parameters of the structure is one of the ways in which the reflection coefficient can be calculated. By monitoring the powers coupled at the four detection ports and using the measured values of certain S parameters the reflection coefficient can be accurately calculated for any load applied at the detection port (port 2 on the six port reflectometer).

However, as it was explained earlier in this chapter, S parameter measurements might now be always possible to perform. This is why other calibration procedures for the six port reflectometer are further illustrated.

7.2.2   Using a calibration step with three standards

As mentioned above, measuring the S parameters of a network may not always be an easy task in real applications. In practice, there is another way of calibrating the six port reflectometer, this time requiring only three well known standards. This method is described in more detail in [2] and has been analysed also in Chapter 5 of this work. Its application is divided into two parts: a six to four port reduction, followed by a short-open-load correction. The last three (a short, an open and a matched load) are the only standards that have to be known accurately. During the six to four port reduction, nine loads have to be applied to the test port, but these do not need to be known by the user. Only the power at the detection ports has to be recorded for each of them. An external load pull system was used to generate the nine loads. Even if they can be theoretically chosen everywhere on the Smith chart, in this experiment the loads were chosen such that they cover as uniformly as possible the whole Smith Chart. The test setup is schematically presented further in Fig. 7.8.
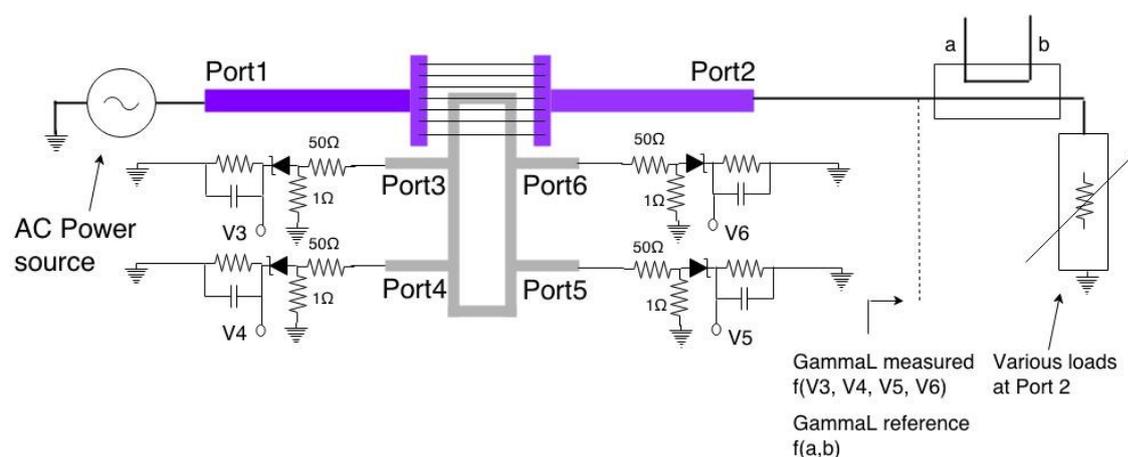
Fig. 7.8 - Test setup for the three standards calibration method.

RF power is applied at port 1 of the six port reflectometer by the use of an AC power source. All the four detection ports are terminated with diode based power meters, as described in Chapter 6. Among the diode detectors described in Chapter 6, the one presented in Fig. 6.7 was chosen for this test. The reasons for this choice are its higher output DC voltage for a particular RF input power, which led in the end to a higher input power dynamic range, and the input impedance constant with the input power level.

The power present at the input of the diode detectors is converted into a voltage that can be easily read with a regular DC voltmeter. Various loads are synthesized at the output port of the reflectometer (port 2), in order to obtain the impedance values required for the calibration step. The standards required in order to perform the short-open-load correction are also generated by the same load pull system. At the end of the calibration step, a set of calibration coefficients is determined. They can be further used in order to determine the reflection coefficient of any unknown load applied at the test port of the six port reflectometer.

To test the functionality of this calibration algorithm, a number of 95 loads uniformly placed along the whole Smith Chart were generated using the load pull system. By using the powers coupled at the four detection ports and the above determined calibration coefficients, the reflection coefficient at port 2 can be calculated for each of these loads. The calculated Γ_L for each of these loads together with the reference Γ_L values are presented on the Smith chart in Fig. 7.9.
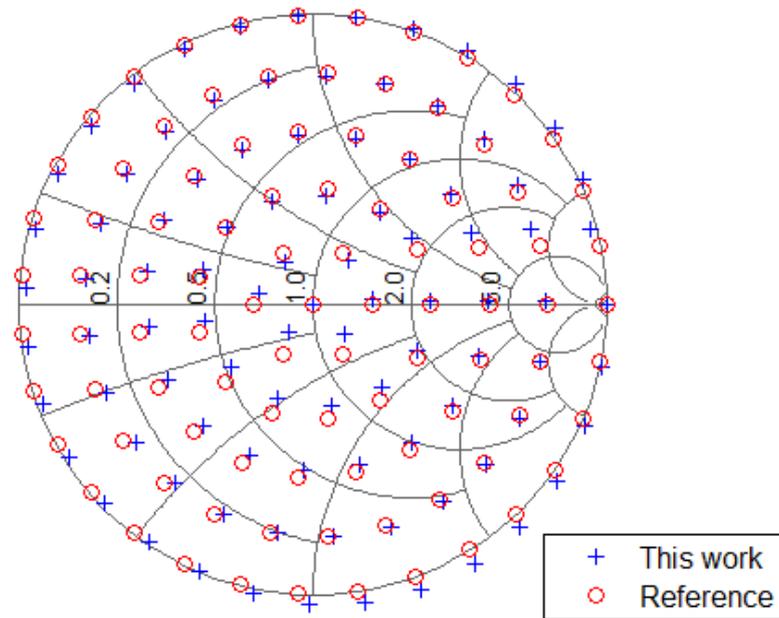
Fig. 7.9 - Results of the three standards six port calibration method representing the reference reflection coefficients (red) and the calculated reflection coefficients (blue).

It can be seen that a clear match exits between the reference and the calculated values. The error in the calculation of the reflection coefficient for each load has a maximum value of -22 dB and an rms value of -32 dB. This error for all the considered loads except for the ones used for the calibration procedure is plotted in Fig. 7.10.
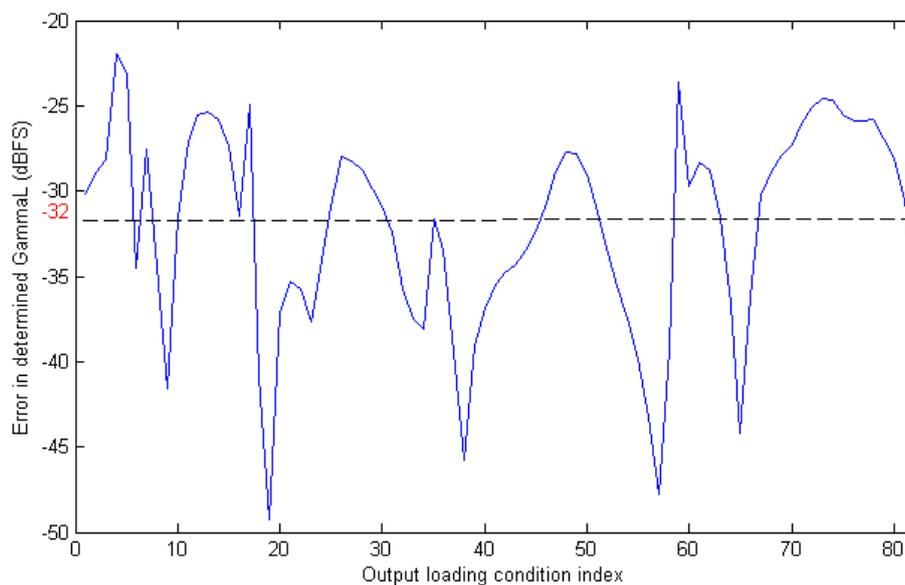
Fig. 7.10 - Error in the calculation of the tested loading conditions, except for the points used in the calibration procedure.

Concluding about this calibration procedure, it can be affirmed that the results obtained for the tested loading conditions are good, the error in the calculation of Γ_L being lower than -20 dB around the whole Smith chart. The biggest advantage is the use of only three accurately

known standards, compared to other calibrations, such as the seven standard calibration technique described in Chapter 5. The downside is the increased computational effort, together with the need of an extra correction step (short-open-load) that has to be applied at the end.

It is important to mention that both the six port calibration algorithms discussed in this chapter (by using the S parameters, and by using three calibration standards) can work with good results independent of the power injected at port 1. In particular applications, situations can arise when the power level at the input does not change, and more important, it is known by the user. In these situations, a simplified way of using the six port reflectometer can be developed, as it will be presented next.

7.2.3 Using an application-specific calibration technique

Most of the applications in which power transistors are used present variations in the amount of output power generated by the amplifier. If this is the case, then a power independent six port calibration procedure has to be used. Two possible procedures have been presented in this sense in the above sections of this chapter. However, it might be possible that certain applications do not vary the amount of input power, keeping it at a level as constant as possible. In this case, using a mathematically complex calibration algorithm like the ones presented above does not make sense, since an easier and quicker way of measuring the reflection coefficient at one particular power level can be developed. Also, the extra linearization step that converts the DC voltage at the output of the diode detector into input RF power will inevitably introduce another small error, as it was presented in Chapter 6. It would be therefore also beneficial to introduce a calibration algorithm that bypasses the linearization step, making use directly of the DC voltages, without the need to convert them back to power.

The idea behind this particular algorithm is to create a lookup table that stores the voltage received by each detector under many possible loading conditions placed at port 2. If a large number of loads are applied there and the four returned voltages are always stored, than these voltages can be interpolated such that functions that cover the whole Smith chart can be developed. Of course, in the end the accuracy of the method will be strongly correlated to the amount of reference loads for which the values of the detector voltages are memorized. Extra memory does not cost anything, since the detected values will be stored on an external device anyway. Therefore, theoretically, a very large number of loads covering almost completely the Smith chart can be memorized. Practically, because of the noise existing in the voltage reading equipment, it is useless to increase the number of reference loads over a certain value, as the distance between each of them will be anyway smaller than the error introduced by the noise in the calculated Γ_L value. In this case, the detection noise will determine in the end the accuracy of the calculated Γ_L.

To test this method, a number of 347 equally spaced loads covering the whole Smith chart were generated by the same load pull system described above. By measuring the voltage returned by each of the four detectors at these 347 loads, a lookup table can be created storing all the voltages. Depending on the loading condition applied at port 2, each of the detectors will return a certain DC voltage. Each set of four detected voltages is taken and compared to the voltages measured at the reference loads and stored in the lookup table. The closest match in the lookup table is then decided to be the reflection coefficient at that load. To perform a simple test the measurement of the 347 impedances was made again, and the resulted voltages were matched to the ones existing in the lookup table. The results are shown in Fig. 7.11.
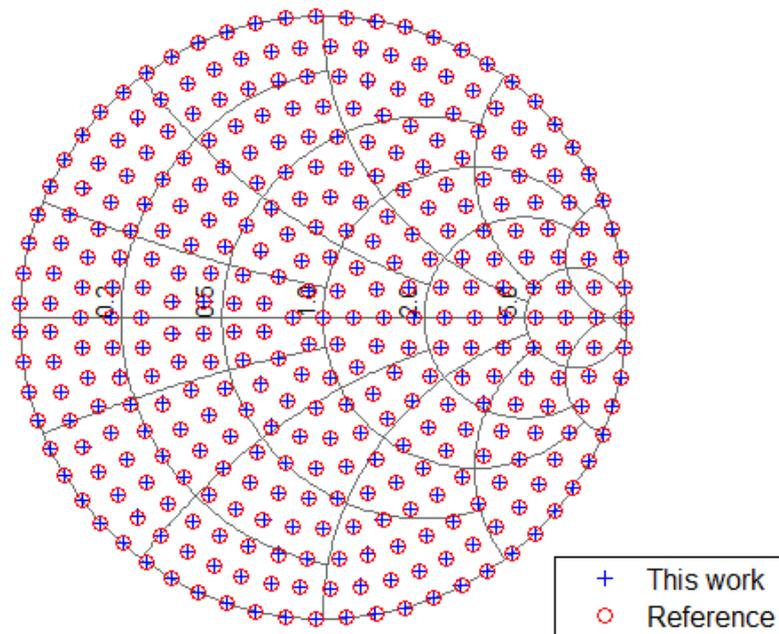
Fig. 7.11 - Results obtained using the look-up table calibration method. The reference reflection coefficients are in red, and the calculated reflection coefficients in blue.

It is clear that using this method, a certain amount of error in intentionally introduced in the final result, as a binary decision is made comparing the obtained four voltages with all the sets of voltages existing in the memorized lookup table. However, as it was stated before, choosing a large number of reference points in the build-up of the lookup table will minimize this error. Even if this method is not so mathematically elegant like the ones presented before, it might prove to be useful in applications where the power level at the output of the power transistor is kept constant, and where a certain amount of error in the calculation of Γ_L can be safely tolerated.

In conclusion, it can be affirmed that the calibration algorithm to be chosen in handling the six port reflectometer depends very much on the type of application in which the power amplifier is used, and also on the available hardware. There is a clear trade-off between the simplicity of the calibration algorithm and its hardware/computational requirements. Measuring

the S parameters of the device can provide a quick and mathematically simple way of measuring the complex reflection coefficient, but comes at the expense of probing the circuit for the S parameter matrix, which might not be always easy or even possible. Using seven well known standards is a good alternative, with a reduced computational effort, but which requires a large number of accurately known calibration loads. Finally, the calibration can be performed using only three well known standards, a short, an open and a load, but the mathematical algorithm is significantly more difficult to implement and also an extra correction stage is needed at the end of the calibration procedure. Finally, as it was used, in case the power at the output of the power transistor is kept constant, a very simplified calibration method involving a lookup table can be used, the errors in determined Γ_L being still small for a very large number of reference loads memorized.

For convenience, the advantages and disadvantages of all the presented methods are illustrated in Table 7.5, together with their computation effort.

Table 7.5 - Investigated six-port calculation algorithms, together with their advantages/disadvantages and the computational effort.

Method	Advantages	Disadvantages	Effort
S parameters	Quick calculation; Simple algorithm	Requires complex S parameters measurement	Medium
Three known standards	Only three well defined standards needed	Lengthy procedure; Extra correction step needed	High
Look-up table	Implementation based only on reading DC voltages;	Interpolation step needed; Inherent calculation error; Functionality at only one input power level for an individual lookup table.	Low

This chapter presented measured results of all the major experiments that were performed during the course of this project. The results can be considered to be good, the deviation from the ideal ones being in most cases very small. Several alternatives for the measurement techniques have been described, with all their advantages and disadvantages. While the theoretical or simulated approach towards presenting this six port implementation can always doubted by some people because of various reasons (possible inaccurate simulation results, ideal noiseless simulation conditions, etc.), the measurements represents the strongest

proof that the concept works within its targeted performance specifications. The most important final conclusions regarding all the concepts and results presented through the course of this work will be drawn in the next chapter.

References

[1] "Three and Four Port S – Parameter Measurements", Application Note, Anritsu Company, 2001.

[2] G.   F. Engen, "Calibrating the Six-Port Reflectometer by Means of Sliding Terminations", IEEE Transactions on Microwave Theory and Techniques, vol. MTT-26, no. 12, December 1978.

8. Conclusion and future work

8.1 Conclusion

The ideas, concepts and measurement results presented in this report represent the most important findings in this thesis project. The objective from which everything started was to aim for an ultra-compact way of measuring the reflection coefficient at the output of a power amplifier. Because of this compactness goal, some trade-offs had to be made in the design to be able to keep the dimensions at a minimum. The proposed solution allows package integration.

The structure of the thesis followed chronologically the steps taken in order to reach the final design, which is the packaged integrated six-port reflectometer. First, the basic theoretical basics and concepts were described to the reader, and the practical importance of this work on a real life basis was illustrated. Then, starting from Chapter 3, various ways of designing a package integrated directional coupler were investigated and the results were interpreted. After analysing several possible implementations, a directional coupler made by placing a microstrip transmission line next to the bondwire array was designed and later produced. Measured data for this directional coupler reported a coupling of -29 dB and a directivity of 14 dB.

The final obtained directivity and coupling factor present good results, considering the compactness of the coupler.

Concluding with the directional coupler, the design process took a step forward by using the directional coupling as a basis for the implementation of a packaged integrated six port reflectometer. After acknowledging the already existing literature on the subject of six port reflectometers, a novel design involving a coupled loop placed underneath the bondwire array was implemented and tested. This design provides the lowest impact of noise / measurement errors in the calculation of the reflection coefficient by using well chosen dimensions. A in the case of a conventional directional coupler, it represents a contactless measurement technique, the low coupling factor between the bondwires and the loop, translated in a minimized influence on the operation of the power transistor. The fabricated reflectometer has a compact size of 36 mm^2, which makes it possible to fit it inside an existing power transistor package, as presented in Fig. 8.1.
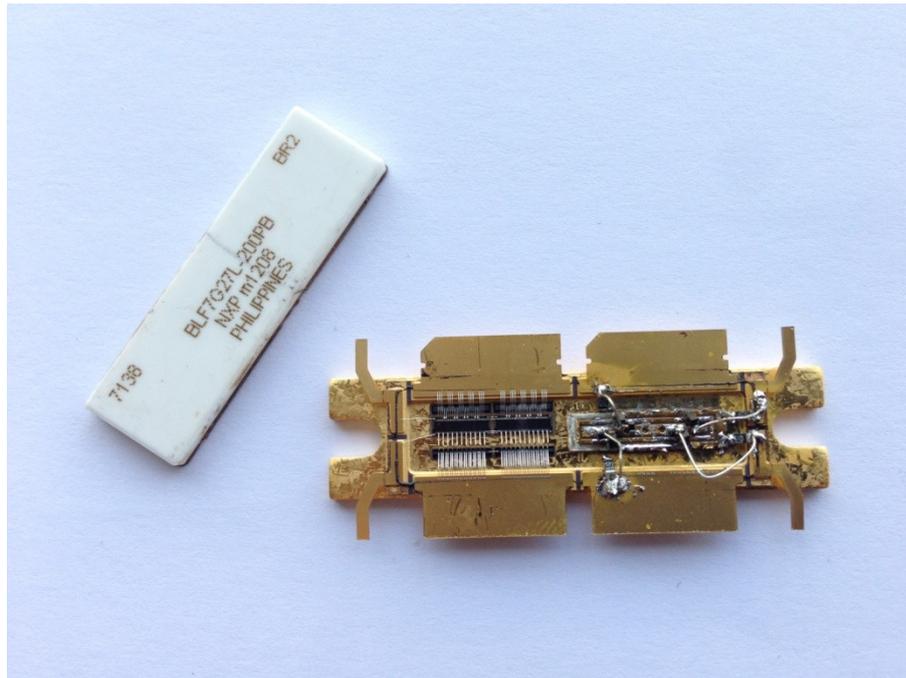
Fig. 8.1 - Photo representing the proposed six port implementation, with the coupled loop and the diode detectors fitted inside a power transistor's package.

Chapter 6 was dedicated to the design, implementation, and measurement of the diode based power detectors. As it was specified in the chapter about the six port reflectometer, power detector are required to detect the powers coupled at the four detection ports. The simplest way to create such a power detector is by making use of a square law diode detector. Three particular designs of such detectors were investigated and the results were illustrated for each of them. The final version, of which was the one used in the end to measure the produced six port, achieved a dynamic range of 75 dB, while having a worst case power conversion error of -20 db, and an rms value of -32 dB. These numbers can compete with commercially available power meters, while the produced detector has a size of only 3 mm^2.

Using these detectors on the six port test board, prototypes have been produced and tested in order to provide a proof of principle. The quality of the calculated reflection coefficients compared to the reference values shows that the proposed implementation has achieved its goal: a compact, package integratable device for measuring output mismatch.

Of course, the limited time allocated to this project did not permit a further development of the design. There are some aspects that definitely deserve more attention as they could be able to increase the performances as well as decrease the size of the produced design. These future steps are presented in the next section.

8.2   Future work

Besides the proposed designs which were presented, produced and tested during this thesis, several other concepts deserve also attention. Due to the limited time, they will be considered as future steps in the further development of this project.

Chapter 3 presented the design process that was followed for implementing the bondwire based directional coupler. As it was highlighted at that point, there are certain design parameters that influence together the final performance of the achieved coupler in terms of coupling and directivity. The most important of these parameters are the length of the bondwires, their height, and the spacing between the bondwire array and the coupled element. In order to get a set of design parameters for the test boards that were later produced, several simulations were performed, as it was presented. However, the conclusions drawn were based on individual sweeps of certain design parameters and not on the combined effect of them together. This means that even better results can be obtained by further investigating the design possibilities for this coupler. Also, a deeper mathematical understanding on the way in which the above mentioned factors (bondwire length, spacing, etc.) affect in the end the achieved performance would make the design of bondwire based directional couplers a lot easier in the future. Consideration regarding these above mentioned aspects will be taken after this present work will be over.

The most important aspect that was followed during the development of this project was the compactness of the final design. The six-port reflectometer has made as small as possible and it compatibility with package integration of a power transistor is the characteristic that distinguishes this work from the abundance of literature, as presented in Chapter 4.

The approach taken to reduce the size of the interferometer was to close the arms of the bondwire based directional coupler into a loop. In this way a layout having a total size of only 36 mm^2 was obtained, and the final version of this layout has been successfully fitted inside an already existing power transistor package, as it was shown in Fig. 8.1.

However, it is very important to observe that in theory, the size of this integrated six port reflectometer can be even further reduced. In the current implementation, the desired 45° shift between each two consecutive power detector is achieved by the use of microstrip transmission lines having the length of $\lambda/8$. At the central frequency of 2.45 GHz, where this reflectometer has been designed, these microstrip segments have a length of 6 mm each. Compared to the size of the additional components placed inside the package (the components required to implement the power detectors) this size is still significantly larger. Therefore, it is easy to observe that by using a different way to create the 45° shift, the total area occupied by the six port can be further reduced, which will further ease the package integration.

A quick solution to this idea is the use of a lumped element approach in order to generate the required phase shift. A simple T-circuit consisting of two inductors and a capacitor can generate 45° of phase shift at the desired frequency by choosing the correct values of the components. The sample T circuit is presented in Fig. 8.2.
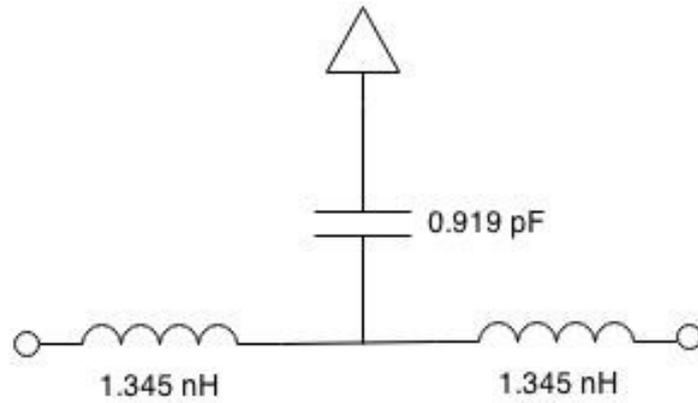
Fig. 8.2 - T circuit implementing a 45° phase shift at the central frequency of 2.45 GHz.

It can be seen that the 45° phase shifter has values for the inductors and the capacitor that allow integration, which when combined with the diodes would yield a major step forward to actual commercialization of the proposed concept. In the view of the author this represents an excellent motivation for a future continuation of this project.

Appendix

A.1 Measured S parameters (magnitude and phase) for the bondwire based directional coupler test board presented in Fig. 7.3

S_{ij} i\j	1	2	3	4
1	0.159/-14.11	0.963/19.52	0.036/170.27	0.007/15.94
2	0.963/19.53	0.158/-128.32	0.007/6.11	0.036/166.65
3	0.036/169.63	0.007/5.71	0.053/3.24	0.977/98.29
4	0.007/16.32	0.036/167.12	0.977/98.23	0.048/13.17

A.2 Measured S parameters (magnitude and phase) for the bondwire based six port reflectometer test board presented in Fig. 7.7

S_{ij} i\j	1	2	3	4	5	6
1	0.070/160.17	0.965/146.27	0.074/18.92	0.053/52.69	0.018/99.46	0.021/138.81
2	0.965/146.40	0.050/140.63	0.021/136.97	0.017/100.0	0.053/51.84	0.076/19.14
3	0.074/18.55	0.021/136.36	0.547/143.17	0.447/-56.48	0.537/-82.08	0.460/-65.49
4	0.053/53.02	0.017/100.18	0.447/-56.60	0.562/144.62	0.432/-59.99	0.548/-82.55
5	0.019/99.21	0.053/51.90	0.537/-82.03	0.432/-60.05	0.551/150.08	0.443/-55.01
6	0.021/138.41	0.076/19.36	0.046/-65.44	0.548/-82.56	0.443/-55.04	0.534/144.61

A.3 Matlab code for calculating the reflection coefficient on a set of test load impedances with a set of collected DC(non-linearized) voltages

```
% Matlab script implementing the reflection coefficient calculation
method
% presented in Section 5.2.3 of the presented thesis report. This
method
% makes use of 9 (not necessarily known) impedances presented at the
output
% port for the six to 4 port reduction, followed by an additional
short-open-load
% correction.


% Data import loop. Imports data into the Matlab script as measured
using
% the Anteverta system. The imported data are the values of the 95
% generated loading conditions at port 2, as well as the sets of four
DC
% voltages at ports 3-6 gathered for each output loading condition
for i=1:50
    sixport_data = sprintf('38dbmtake%d.mat',i);
    sixport = load(sixport_data);
    gamma_set(:, :) = sixport.results.PowerDomain.GL_f0;
    v1(i,:) = sixport.results.PowerDomain.Vin+0.00123; %offsets are
added to each channel in order to cancel the negative values
    v2(i,:) = sixport.results.PowerDomain.Iin+0.00112;
    v3(i,:) = sixport.results.PowerDomain.Vout+0.001932;
    v4(i,:) = sixport.results.PowerDomain.Iout+0.001741;
end

% The mean value of the four voltages for all 4 channels is calculated
for
% each individual loading condition as the mean of all voltage
measurements
for i=1:95
   v1_mean(i)=mean2(v1(:,i))-1.943847947384541e-004;
   v2_mean(i)=mean2(v2(:,i))-9.803707902493577e-005;
   v3_mean(i)=mean2(v3(:,i))-8.290423602728795e-005;
   v4_mean(i)=mean2(v4(:,i))-9.157327682866405e-005;
end

% Linearization coefficients as determined by the linearization
algorithm
% presented in Section 6.3. This algorithm used as an example an order
n=5,
% and 50 reference points.
lin1=[2.045827155316695e+000
    -1.682762437051209e+001
     5.493358001471824e+001
    -9.618286595657172e+001
     6.211950488256878e+001
     2.678111246823072e+000
     1.202991376179127e+000
     ];
lin2=[3.219929517400507e+000
```

```
        -2.161729674552784e+001
         8.460835415783731e+001
        -1.637393911783605e+002
         1.195946233390821e+002
         3.172268151251135e+000
         1.244865700303108e+000
         ];
lin3=[2.572488713150230e+000
        -1.843926525395157e+001
         6.295834300443132e+001
        -1.095438746573229e+002
         7.038571404775281e+001
         2.862658428312949e+000
         1.200180609937962e+000
         ];
lin4=[-0.349683757104060
        -6.089589439095618
         9.306630041990950
        -10.410496540117032
        -3.114798271455104
         1.953193379318763
         1.061416310295121
         ];
% Linearization constants used in the linearization method, as
described in
% Section 6.3
linearization_constant_1=exp(lin1(length(lin1)-1));
linearization_constant_2=exp(lin2(length(lin2)-1));
linearization_constant_3=exp(lin3(length(lin3)-1));
linearization_constant_4=exp(lin4(length(lin4)-1));


% Linearization scaling factors used in the linearization method, as
described in
% Section 6.3
scaling_factor_1=0.5/0.166400393718216;
scaling_factor_2=0.5/0.118462135538411;
scaling_factor_3=0.5/0.137702614926787;
scaling_factor_4=0.5/0.177719344021170;


% In the next loop the four detector powers are calculated from the
% respective DC voltage readings as described in the linearization
% method
for i=1:95
    for j=1:length(lin1)-2
    power_series1(j)=lin1(j)*power(scaling_factor_1*v1_mean(i),j);
    power_series2(j)=lin2(j)*power(scaling_factor_2*v2_mean(i),j);
    power_series3(j)=lin3(j)*power(scaling_factor_3*v3_mean(i),j);
    power_series4(j)=lin4(j)*power(scaling_factor_4*v4_mean(i),j);
    end

    exponent_1=sum(power_series1)+lin1(length(lin1));
    exponent_2=sum(power_series2)+lin2(length(lin1));
    exponent_3=sum(power_series3)+lin3(length(lin1));
    exponent_4=sum(power_series4)+lin4(length(lin1));



P1(i)=linearization_constant_1*power(scaling_factor_1*v1_mean(i),expon
ent_1);
```

```matlab
P2(i)=linearization_constant_2*power(scaling_factor_2*v2_mean(i),expon
ent_2);

P3(i)=linearization_constant_3*power(scaling_factor_3*v3_mean(i),expon
ent_3);

P4(i)=linearization_constant_4*power(scaling_factor_4*v4_mean(i),expon
ent_4);
end

% A table is created comprising all the informations related to a
% particular loading condition: the known reflection coefficient, the
% voltage readings at the four detector ports and the calculated
powers at
% the four detection ports
for i=1:95
lookup(1,i)= gamma_set(i);
lookup(2,i)= v1_mean(i);
lookup(3,i)= v2_mean(i);
lookup(4,i)= v3_mean(i);
lookup(5,i)= v4_mean(i);
lookup(6,i)=P1(i);
lookup(7,i)=P2(i);
lookup(8,i)=P3(i);
lookup(9,i)=P4(i);
end

% The coefficients required for first estimate in the the six port
calibration algorithm are
% calculated in the next loop, as descibed in the six port calibration
% algorithm
for i=1:95
    coefficients(1,i)=power(P2(i)/P1(i),2);
    coefficients(2,i)=power(P3(i)/P1(i),2);
    coefficients(3,i)=power(P4(i)/P1(i),2);
    coefficients(4,i)=P2(i)/P1(i)*P3(i)/P1(i);
    coefficients(5,i)=P2(i)/P1(i)*P4(i)/P1(i);
    coefficients(6,i)=P3(i)/P1(i)*P4(i)/P1(i);
    coefficients(7,i)=P2(i)/P1(i);
    coefficients(8,i)=P3(i)/P1(i);
    coefficients(9,i)=P4(i)/P1(i);
end


Coefficient_matrix= [transpose(coefficients(:,9));
    transpose(coefficients(:,20));
    transpose(coefficients(:,30));
    transpose(coefficients(:,40));
    transpose(coefficients(:,71));
    transpose(coefficients(:,75));
    transpose(coefficients(:,82));
    transpose(coefficients(:,85));
    transpose(coefficients(:,90));
    ];


Constant_matrix=[ -1;
    -1;
```

```matlab
    -1;
    -1;
    -1;
    -1;
    -1;
    -1;
    -1;
    ];

% A linear system of equations is used to calcultate the first
estimate coefficients
% required to use the six port algorithm
x=linsolve(Coefficient_matrix,Constant_matrix);


r=(2*x(5)-x(7)*x(9))/(2*x(1)*x(9)-x(5)*x(7));
q=(2*x(4)-x(7)*x(8))/(2*x(1)*x(8)-x(4)*x(7));
p=r+q+x(7)/x(1);
A_5=power(x(2)*p*r,0.25);
A_6=power(x(3)*p*q,0.25);


% An initial estimate for the non linear system is determined
x0=[q,r,p,A_5,A_6];
c=x;
options = optimset('MaxFunEvals',200000,'MaxIter',200000,'TolFun',1e-
10); % Option to display output
% The 5 six port coefficients are calcuated from a nonlinear system of
9
% equations. nonlinear_system is a separate Matlab file containing the
% nonlinear system, as described in Section 5.2.3
[k] = fsolve(@(x) nonlinear_system(x,c),x0,options) ;


% In order to test the six port principle, the algorithm is applied to
all
% the 95 measured loads
for i=1:95

p4=  P2(i)/P1(i);
p5=  P3(i)/P1(i);
p6=  P4(i)/P1(i);



% The real and imaginary parts of the reflection coefficient in the w-
plane
% are calculated
real=(p4-k(4)*k(4)*p5+k(2))/(2*sqrt(k(2)));
imag=(k(2)*(k(3)+k(1)-k(2))+(k(3)-k(1)+k(2))*p4-(k(3)-k(1)-
k(2))*k(4)*k(4)*p5-
2*k(2)*k(5)*k(5)*p6)/(2*sqrt(k(2)*(2*k(1)*k(3)+2*k(1)*k(2)+2*k(2)*k(3)
-k(3)*k(3)-k(1)*k(1)-k(2)*k(2))));


gamma_embedd(i)=real+1i*imag;
end


% A short-open-load correction is performed to translated the w-plane
% reflection coefficient into the GammaL plane
A=[ ( gamma_embedd(1))*(lookup(1,1)), -(lookup(1,1)), -1;
    ( gamma_embedd(95))*(lookup(1,95)),-(lookup(1,95)),-1;
    ( gamma_embedd(72))*(lookup(1,72)),-(lookup(1,72)),-1];
```

```
B=[(  -gamma_embedd(1));
   (  -gamma_embedd(95));
   (  -gamma_embedd(72));];

error_terms=linsolve(A,B);

c=error_terms(1);
d=error_terms(2);
e=error_terms(3);

smithchart

% The variable gamma_deembedd holds the GammaL plane reflection
coefficient
% values for all the 95 test loads
for i=1:95
gamma_deembedd(i)=(-gamma_embedd(i)+e)/(c*gamma_embedd(i)-d);
% zload calculates the respective impedance value on Port 2 based on
the
% determined reflection coefficient
zload=(50)*(1+gamma_deembedd)/(1-gamma_deembedd);
% The difference variable calculates the difference between the
determined
% reflection coefficient result and the reflection coefficient set in
the
% Anteverta system
difference(i)=gamma_deembedd(i)-lookup(1,i);
hold on
%The determined value of the reflection coefficient is plotted on the
same
%plot with the reference value set by the load pull system
plot(gamma_deembedd(i), '+b');
plot(lookup(1,i),'or');
end

for i=1:95
    dif_percent(i)=abs(difference(i))/abs(lookup(1,i))*100;
end
%The impedance points taken for the calibration and corection
algorithms
%are extracted from the final plotted result
difference_short=[difference(2:8),
difference(11:19),difference(21:29),difference(31:39),difference(41:70
),difference(73:74),difference(76:81),difference(83:84),difference(86:
89),difference(91:94)];
figure
%The error in dB between the determined reflection coefficient value
and
%the reference value is plotted
stem(db(difference_short))
xlabel('Output loading condition (95 different loads)')
ylabel('Error in determined GammaL (dBFS)')
axis([0 82 -50 0]);
for i=1:82
    difference_square(i)=(power(difference(i),2));



rms_difference=db(sqrt(mean(difference_square)))
```